

1 **Is a scaling factor required to obtain closure between measured and**
2 **modelled atmospheric O₄ absorptions? — An assessment of uncertainties of**
3 **measurements and radiative transfer simulations — case study for two days**
4 **during the MAD-CAT campaign**

5
6 Thomas Wagner¹, Steffen Beirle¹, Nuria Benavent², Tim Bösch³, Kai~~1~~ Lok Chan⁴,
7 Sebastian Donner¹, Steffen Dörner¹, Caroline Fay⁵, Udo Frieß⁶, David~~1~~ García-Nieto², Clio
8 Gielen^{5*}, David González-Bartolome⁷, Laura Gomez⁷, François Hendrick⁵, Bas Henzing⁸,
9 Jun Li Jin⁹, Ted Koenig, Johannes Lampel⁶, Jianzhong Ma¹⁰, Kornelia Mies¹, Mónica
10 Navarro⁷, Ivan Ortega, Enno Peters⁴Peters^{3**}, Gaia Pinardi⁵, Olga Puentedura⁷, Janis
11 Pukštěl¹, Julia Remmers¹, Andreas Richter³, Alfonso Saiz-Lopez², Reza Shaiganfar¹, Holger
12 Sihler¹, Michel Van Roozendael⁵, Rainer Volkamer, Yang Wang¹, Margarita Yela⁷

13 1 Max Planck Institute for Chemistry, Mainz, Germany

14 2 Department of Atmospheric Chemistry and Climate, Institute of Physical Chemistry
15 Rocasolano (CSIC), Spain.

16 3 University of Bremen, Germany

17 4 Meteorological Institute, Ludwig-Maximilians-Universität München, Germany

18 5 Royal Belgian Institute for Space Aeronomy (BIRA-IASB), Brussels, Belgium

19 6 University of Heidelberg, Germany

20 7 Instituto Nacional de Tecnica Aeroespacial (INTA), Spain

21 8 TNO, Netherlands Institute for Applied Scientific Research

22 9 CMA Meteorological Observation Center, China

23 10 Chinese Academy of Meteorological Science, China

24 * currently at the Institute of Astronomy, KU Leuven, Belgium

25 ** Now at Institute for protection of maritime infrastructures, German Aerospace Center
26 (DLR), Bremerhaven, Germany

27 **Abstract**

28 In this study the consistency between MAX-DOAS measurements and radiative transfer
29 simulations of the atmospheric O₄ absorption is investigated on two mainly ~~clear~~cloud-free
30 days during the MAD-CAT campaign in Mainz, Germany, in Summer 2013. In recent years
31 several studies indicated that measurements and radiative transfer simulations of the
32 atmospheric O₄ absorption can only be brought into agreement if a so-called scaling factor
33 (<1) is applied to the measured O₄ absorption. However, many studies, ~~in particular~~including
34 such based on direct sun light measurements, came to the opposite conclusion, that there is no
35 need for a scaling factor. Up to now, there is no broad consensus for an explanation for the
36 observed discrepancies between measurements and simulations. Previous studies inferred the
37 need for a scaling factor from the comparison of the aerosol optical depth derived from MAX-
38 DOAS O₄ measurements with that derived from coincident sun photometer measurements. In
39 this study a different approach is chosen: the measured O₄ absorption at 360 nm is directly
40 compared to the O₄ absorption obtained from radiative transfer simulations. The atmospheric
41 conditions used as input for the radiative transfer simulations were taken from independent
42 data sets, in particular from sun photometer and ceilometer measurements at the measurement
43 site. ~~The comparisons are performed for two selected clear days with similar aerosol optical~~
44 ~~depth but very different aerosol properties. This study has three main goals: First For both~~
45 ~~days not only the O₄ absorptions are compared, but also~~ all relevant error sources of the

49 spectral analysis, the radiative transfer simulations as well as the extraction of the input
50 parameters used for the radiative transfer simulations are quantified. One important result
51 obtained from the analysis of synthetic spectra is that the O₄ absorptions derived from the
52 spectral analysis agree within 1% with the corresponding radiative transfer simulations at 360
53 nm. Based on the results from sensitivity studies, recommendations for optimised settings for
54 the spectral analysis and radiative transfer simulations are given. The performed tests and
55 sensitivity studies might be useful for the analysis and interpretation of O₄ MAX-DOAS
56 measurements in future studies. Second, the measured and simulated results are compared
57 Different comparison results are found for both days: On 18 June, measurements and
58 simulations agree within their (rather large) errors (the ratio of simulated and measured O₄
59 absorptions is found to be 1.01 ± 0.16). In contrast, on 8 July measurements and simulations
60 significantly disagree: For the middle period of that day the ratio of simulated and measured
61 O₄ absorptions is found to be 0.74 ± 0.12 , which differs significantly from unity. Thus
62 for that day a scaling factor is needed to bring measurements and simulations into agreement.
63 Third, recommendations for further intercomparison exercises are derived. One possible
64 reason for the comparison results on 18 June is the rather large aerosol extinction (and its
65 large uncertainty) close to the surface, which has a large effect on the radiative transfer
66 simulations. One important recommendation for future studies is that aerosol profile data
67 should be measured at the same wavelengths as the MAX-DOAS measurements. Also the
68 altitude range without profile information close to the ground should be minimised and
69 detailed information of the aerosol optical and/or microphysical properties should be used.
70 Besides the inconsistent comparison results for both days, also no explanation for a O₄ scaling
71 factor could be derived in this study. Thus similar, but more extended future studies should be
72 performed, which preferably include more measurement days, and more instruments and
73 should be supported by more detailed independent aerosol measurements. Also additional
74 wavelengths should be included. The MAX-DOAS measurements collected during the recent
75 CINDI-2 campaign are probably well suited for that purpose.
76

77 1 Introduction

78 Observations of the atmospheric absorption of the oxygen collision complex (O₂)₂ (in the
79 following referred to as O₄, see Greenblatt et al. (1990)) are often used to derive information
80 about atmospheric light paths from remote sensing measurements of scattered sun light (made
81 e.g. from ground, satellite, balloon or airplane). Since atmospheric radiative transport is
82 strongly influenced by scattering on aerosol and cloud particles, information on the presence
83 and properties of clouds and aerosols can be derived from O₄ absorption measurements.

84 Early studies based on O₄ measurements focussed on the effect of clouds (e.g. Erle et al.,
85 1995; Wagner et al., 1998; Winterrath et al., 1999; Acarreta et al., 2004; Sneep et al., 2008;
86 Heue et al., 2014; Gielen et al., 2014; Wagner et al., 2014), which is usually stronger than that
87 of aerosols. Later also aerosol properties were derived from O₄ measurements, in particular
88 from Multi-AXis- (MAX-) DOAS measurements (e.g. Hönninger et al., 2004; Wagner et al.,
89 2004; Wittrock et al., 2004; Friess et al., 2004; Irie et al. Clémer 2010; Friess et al., 2016 and
90 references therein). For the retrieval of aerosol profiles usually forward model simulations for
91 various assumed aerosol profiles are compared to measured O₄ slant column densities (SCD,
92 the integrated O₄ concentration along the atmospheric light path). The aerosol profile
93 associated with the best fit between the forward model and measurement results is considered
94 as the most probable atmospheric aerosol profile (for more details, see e.g. Frieß et al., 2006).
95 Note that in some cases no unique solution might exist, if different atmospheric aerosol
96 profiles lead to the same O₄ absorptions. MAX-DOAS aerosol retrievals are typically
97 restricted to altitudes below about 4 km; see Friess et al. (2006).

99 About ten years ago, Wagner et al. (2009) suggested to apply a scaling factor (SF <1) to the
100 O₄ SCDs derived from MAX-DOAS measurements at 360 nm in Milano in order to achieve
101 agreement with forward model simulations. They found that on a day with low aerosol load
102 the measured O₄ SCDs were larger than the model results, even if no aerosols were included
103 in the model simulations. If, however, the measured O₄ SCDs were scaled by a SF of 0.81,
104 good agreement with the forward model simulations (and nearby AERONET measurements)
105 was achieved. Similar findings were then reported by Clémer et al. (2010), who suggested a
106 SF of 0.8 for MAX-DOAS measurements in Beijing. Interestingly, they applied this SF to
107 four different O₄ absorption bands (360, 477, 577, and 630 nm).

108 While with the application of a SF the consistency between forward model and measurements
109 was substantially improved, both studies could not provide an explanation for the physical
110 mechanism behind such a SF. In the following years several research groups applied a SF in
111 their MAX-DOAS aerosol profile retrievals. However, a similarly large fraction of studies
112 (including direct sun measurements and aircraft measurements, see Spinei et al. (2015)) did
113 not find it necessary to apply a SF to bring measurements and forward model simulations into
114 agreement. An overview on the application of a SF in various MAX-DOAS publications after
115 2010 is provided in Table 1. Up to now, there is no community consensus on whether or not a
116 SF is needed for measured O₄ SCDs. This is a rather unfortunate situation, because this
117 ambiguity directly affects the aerosol results derived from MAX-DOAS measurements and
118 thus the general confidence in the method.

119
120 So far, most of the studies deduced the need for a SF in a rather indirect way: aerosol
121 extinction profiles derived from MAX-DOAS measurements using different SF are usually
122 compared to independent data sets (mostly AOD from sun photometer observations) and the
123 SF leading to the best agreement is selected. In many cases SF between 0.75 and 0.9 were
124 derived.

125 In this study, we follow a different approach: similar to Ortega et al. (2016) we directly
126 compare the measured O₄ SCDs with the corresponding SCDs derived from a forward model.
127 For this comparison, atmospheric conditions which are well characterised by independent
128 measurements are chosen. Such a procedure allows in particular quantifying the influence of
129 the errors of the individual processing steps.

130 One peculiarity of this comparison is that the measured O₄ SCDs are first converted into their
131 corresponding air mass factors (AMF), which are defined as the ratio of the SCD and the
132 vertical column density (VCD, the vertically integrated concentration) (Solomon et al., 1987).
133

$$134 \quad AMF = \frac{SCD}{VCD} \quad (1)$$

135
136 The ‘measured’ O₄ AMF is then compared to the corresponding AMF derived from radiative
137 transfer simulations for the atmospheric conditions during the measurements:
138

$$139 \quad AMF_{measured} = AMF_{simulated} \quad (2)$$

140
141 The conversion of the measured O₄ SCDs into AMFs is carried out to ensure a simple and
142 direct comparison between measurements and forward model simulations. Here it should be
143 noted that in addition to the AMFs also so-called differential AMFs (dAMFs) will be
144 compared in this study. The dAMFs represent the difference between AMFs for
145 measurements at non-zenith elevation angles α and at 90° for the same elevation sequence:

$$147 \quad dAMF_{\alpha} = AMF_{\alpha} - AMF_{90^\circ} \quad (3)$$

148
149 For the comparison between measured and simulated O₄ (d)AMFs, two mostly ~~clear~~cloud-free
150 days (18 June and 08 July 2013) during the Multi Axis DOAS Comparison campaign for
151 Aerosols and Trace gases (MAD-CAT) campaign are chosen ([http://joseba.mpch-
152 mainz.mpg.de/mad_cat.htm](http://joseba.mpch-mainz.mpg.de/mad_cat.htm)). As discussed in more detail in section 4.2.2, based on the
153 ceilometer and sun photometer measurements, three periods on each of both days are selected,
154 during which the variation of the aerosol profiles was relatively small (see Table 2). In
155 addition to the aerosol profiles, also other atmospheric properties are averaged during these
156 periods before they are used as input for the radiative transfer simulations.
157 The comparison is carried out for the O₄ absorption band at 360 nm, which is the strongest O₄
158 absorption band in the UV. In principle also other O₄ absorption bands (e.g. in the visible
159 spectral range) could be chosen, but these bands are not covered by the wavelength range of
160 the MPIC instrument. Thus they are not part of this study.
161 Deviations between forward model and measurements can have different reasons: In the
162 following an overview on these error sources and the way they are investigated in this study
163 are given:
164 a) Calculation of O₄ profiles and O₄ VCDs (eq. 1):
165 Profiles and VCDs of O₄ are derived from pressure and temperature profiles. The errors of the
166 pressure and temperature profiles are quantified by sensitivity studies and by the comparison
167 of the extraction results derived from different groups/persons (see Table 3).
168 b) Calculation of O₄ (d)AMFs from radiative transfer simulations:
169 Besides differences between the different radiative transfer codes, the dominating error
170 sources are the uncertainties of the input parameters. They are investigated by sensitivity
171 studies and by the comparison of extracted input data by different groups/persons. Also the
172 effects of operating different radiative transfer models by different groups are investigated.
173 c) Analysis of the O₄ (d)AMFs from MAX-DOAS measurements:
174 Uncertainties of the spectral analysis results are caused by errors and imperfections of the
175 measurements/instruments, by the dependence of the analysis results on the specific fit
176 settings, and the uncertainties of the O₄ cross sections. They are investigated by systematic
177 variation of the DOAS fit settings (for measured and synthetic spectra), and by comparison of
178 analysis results obtained from different groups and/or instruments.
179 The paper is organised as follows: in section 2, information on the selected days during the
180 MAD-CAT campaign, on the MAX-DOAS measurements, and on the data sets from
181 independent measurements is provided. Section 3 presents initial comparison results for the
182 selected days using standard settings. In section 4 the uncertainties associated with each of the
183 various processing steps of the spectral analysis and the forward model simulations are
184 quantified. Section 5 presents a summary and conclusions.
185
186
187 **2 MAD-CAT campaign, MAX-DOAS instruments and other data sets used in this study**
188
189 The Multi Axis DOAS Comparison campaign for Aerosols and Trace gases (MAD-CAT)
190 (http://joseba.mpch-mainz.mpg.de/mad_cat.htm) took place in June and July 2013 on the roof
191 of the Max-Planck-Institute for Chemistry in Mainz, Germany. The main aim of the campaign
192 was to compare MAX-DOAS retrieval results of several atmospheric trace gases like NO₂,
193 HCHO, HONO, CHOCHO as well as aerosols. The measurement location was at 150m above
194 sea level at the western edge of the city of Mainz.
195

196 **2.1 MAX-DOAS instruments**
197

198 During the MAD-CAT campaign, 11 MAX-DOAS instruments were operated by different
199 groups; an overview can be found at the website [http://joseba.mpch-
200 mainz.mpg.de/equipment.htm](http://joseba.mpch-mainz.mpg.de/equipment.htm). The main viewing direction of the MAX-DOAS instruments
201 was towards north-west (51° with respect to North). Measurements at this viewing direction
202 were the main focus of this study, but a few comparisons using the ‘standard settings’ (see
203 section 3) were also carried out for three other azimuth angles (141° , 231° , 321° , see Fig. A2 I
204 in appendix A1). Each elevation sequence contains the following elevation angles: 1, 2, 3, 4,
205 5, 6, 8, 10, 15, 30 and 90° . In this study, in addition to the MPIC instrument, also spectra from
206 3 other MAX-DOAS instruments were analysed. The instrumental details are given in Table
207 4. The spectra of the MPIC instrument are available at the website [http://joseba.mpch-mainz.mpg.de/e_doc_zip.htm](http://joseba.mpch-
208 mainz.mpg.de/e_doc_zip.htm).

209
210 **2.2 Additional data sets**
211

212 In order to constrain the radiative transfer simulations, independent measurements and data
213 sets were used. In particular, information on atmospheric pressure, temperature and relative
214 humidity, as well as aerosol properties is used. In addition to local in situ measurements from
215 air quality monitoring stations and remote sensing measurements by a ceilometer and a sun
216 photometer, also ECMWF reanalysis data were used. An overview on these data sets is given
217 in Table 5. The data sets used in this study are available at the websites [http://joseba.mpch-mainz.mpg.de/a_doc_zip.htm](http://joseba.mpch-
218 mainz.mpg.de/a_doc_zip.htm) and http://joseba.mpch-mainz.mpg.de/c_doc_zip.htm.

219
220 **2.3 RTM simulations**
221

222 Several radiative transfer models are used to calculate O₄ (d)AMFs for the selected days. As
223 input, vertical profiles of temperature, pressure, relative humidity and aerosol extinction
224 extracted from the independent data sets (see section 2.2 and 4) were used. The vertical
225 resolution is high in the lowest layers and decreases with increasing altitude (see Table A1 in
226 appendix A1). The upper boundary of the vertical grid is set to 1000 km. The lower boundary
227 of the model grid represents the surface elevation of the instrument (150 m above sea level).
228 For the ‘standard run’, a surface albedo of 5% is assumed and the aerosol optical properties
229 are described by a Henyey-Greenstein phase function with an asymmetry parameter of 0.68
230 and a single scattering albedo of 0.95. Both values represent typical urban aerosols (see e.g.
231 Dubovik et al., 2002). Ozone absorption was not considered, because it is very small at 360
232 nm. The MAD-CAT campaign took place around summer solstice. Thus the same dependence
233 of the solar zenith angle (SZA) and relative azimuth angle (RAZI) on time is used for both
234 days (see Table A2 in the appendix A1). The input data used for the radiative transfer
235 simulations are available at the website http://joseba.mpch-mainz.mpg.de/d_doc_zip.htm. In
236 the following sub-sections the different radiative transfer models used in this study are
237 described.

238
239 **2.3.1 MCARTIM**
240

241 The full spherical Monte Carlo radiative transfer model MCARTIM (Deutschmann et al.,
242 2011) explicitly simulates individual photon trajectories including the photon interactions
243 with molecules, aerosol particles and the surface. In this study two versions of MCARTIM are
244 used: version 1 and version 3. Version 1 is a 1-D scalar model. Version 3 can also be run in 3-
245 D and vector modes. In version 1 Rotational Raman scattering (RRS) is partly taken into

247 account: the RRS cross section and phase function are explicitly considered for the
248 determination of the photon paths, but the wavelength redistribution during the RRS events is
249 not considered. In version 3 RRS can be fully taken into account. If operated in the same
250 mode (1-D scalar) both models show excellent agreement.

253 2.3.2 LIDORT

254
255 In this study the LIDORT version 3.3 was used. The Linearized Discrete Ordinate Radiative
256 Transfer (LIDORT) forward model (Spurr et al., 2001; Spurr et al., 2008) is based on the
257 discrete ordinate method to solve the radiative transfer equation (e.g.: Chandrasekhar, 1960;
258 Chandrasekhar, 1989; Stamnes et al., 1988). This model considers a pseudo-spherical multi-
259 layered atmosphere including several anisotropic scatters. The formulation implemented
260 corrects for the atmosphere curvature in the solar and single scattered beam, however the
261 multiple scattering term is treated in the plane-parallel approximation. The properties of each
262 of the atmospheric layers are considered homogenous in the corresponding layer. Using finite
263 differences for the altitude derivatives, this linearized code converts the problem into a linear
264 algebraic system. Through first order perturbation theory, it is able to provide radiance field
265 and radiance derivatives with respect to atmospheric and surface variables (Jacobians) in a
266 single call. LIDORT was used in several studies to derive vertical profiles of aerosols and
267 trace gases from MAX-DOAS (e.g. Clémer et al., 2010; Hendrick et al., 2014; Franco et al.,
268 2015).

271 2.3.3 SCIATRAN

272
273 The RTM SCIATRAN (Rozanov et al. 2014) was used in its full-spherical mode including
274 multiple scattering but without polarization. In the operation mode used here, SCIATRAN
275 solves the transfer equations using the discrete ordinate method. In this study, SCIATRAN
276 was used by two groups: The IUP Bremen group used v3.8.3 for the for the O₄ dAMFs
277 simulations (without Raman scattering). The MPIC group used v3.6.11 for the calculation of
278 synthetic spectra (see Section 2.4) and for the O₄ dAMFs simulations (including Raman
279 scattering).

282 2.4 Synthetic spectra

283
284 In addition to AMFs and dAMFs, also synthetic spectra were simulated. They are analysed in
285 the same way as the measured spectra, which allows the investigation of two important
286 aspects:

287 a) The derived O₄ dAMFs from the synthetic spectra can be compared to the O₄ dAMFs
288 obtained directly from the radiative simulations at one wavelength (here: 360 nm) using the
289 same settings. In this way the consistency of the spectral analysis results and the radiative
290 transfer simulations is tested.

291 b) Sensitivity tests can be performed varying several fit parameters, e.g. the spectral range or
292 the DOAS polynomial, and their effect on the derived O₄ dAMFs can be assessed.

293 Synthetic spectra are simulated using SCIATRAN taking into account rotational Raman
294 scattering. The basic simulation settings are the same as for the RTM simulations of the O₄
295 (d)AMFs described above. In order to minimise the computational effort, for the profiles of
296 temperature, pressure, relative humidity and aerosol extinction the input data for only two
297 periods (18 June: 11:00 – 14:00, 08 July: 7:00 – 11:00, see Table 2) are used for the whole

298 day. Thus ‘perfect’ agreement with the measurements can only be expected for the two
299 selected periods. Aerosol optical properties (phase function and single scattering albedo) are
300 taken from AERONET measurements of the two selected days. Although the wavelength
301 dependencies of both quantities (and also for the aerosol extinction) are considered, it should
302 be noted that the associated uncertainties are probably rather large, since the optical properties
303 in the UV had to be extrapolated from measurements in the visible spectral range. Moreover,
304 the phase functions were not available as fully consolidated AERONET level 2.0 data, but
305 only as level 1.5 data.

306 Spectra were simulated at a spectral resolution of 0.01 nm and convolved with a Gaussian slit
307 function of 0.6 nm full width at half maximum (FWHM), which is similar to those of the
308 measurements. For the generation of the spectra a high resolutio solar spectrum (Chance and
309 Kurucz, 2010) and the trace gas absorptions of O₃, NO₂, HCHO, and O₄ are considered (see
310 Table A3 in appendix A1). The assumed tropospheric profiles of NO₂ and HCHO are similar
311 to those retrieved from the MAX-DOAS observations during the selected periods. Time series
312 of the tropospheric VCDs of NO₂ and HCHO for the two selected days are shown in Fig. A1
313 in appendix 1.

314 Two sets of synthetic spectra were simulated, one taking into account the temperature
315 dependence of the O₄ cross section and the other not. For the case without considering the
316 temperature dependence the O₄ cross section for 293 K is used. In addition to spectra without
317 noise, also spectra with noise (sigma of the noise is assumed as $7.5 \cdot 10^{-4}$ times the intensity)
318 were simulated. The synthetic spectra are available at the website http://joseba.mpc-mainz.mpg.de/f_doc_zip.htm.

3 Strategies used in this studies and comparison results for ‘standard settings’

3.1 Selection of days

325 For the comparison of measured and simulated O₄ dAMFs, two mostly clearcloud-free days
326 during the MAD-CAT campaign (18 June and 8 July 2013) were selected. On both days the
327 AOD measured by the AERONET sun photometer at 360 nm is between 0.25 and 0.4 (see
328 Fig. 1). In spite of the similar AOD, very different aerosol properties at the surface are found
329 on the two days: on 18 June much higher concentrations of large aerosol particles (PM_{2.5} and
330 PM₁₀) are found. These differences are also represented by the large differences of the
331 Ångström parameter for long wavelengths (440 – 870 nm) on both days. Also the aerosol
332 height profiles are different: On 8 July rather homogenous profiles with a layer height of
333 about 2 km occur. On 18 June the aerosol profiles reach to higher altitudes, but the highest
334 extinction is found close to the surface. Also the temporal variability of the aerosol properties,
335 especially the near-surface concentrations, is much larger on 18 June.

3.2 Different levels of comparisons

339 The comparison between the forward model and MAX-DOAS measurements is performed in
340 different depth for different subsets of the measurements:

341 a) A quantitative comparison of O₄ AMFs and O₄ dAMFs is performed for 3° elevation angle
342 at the standard viewing direction (51° with respect to North) for the middle periods of both
343 selected days. During these periods the uncertainties of the measurement and the radiative
344 transfer simulations are smallest because around noon the measured intensities are high and
345 the variation of the SZA is small. During the selected periods, also the variation of the
346 ceilometer profiles is relatively small. These comparisons thus constitute the core of the
347 comparison exercise and all sensitivity studies are performed for these two periods. The
348 elevation angle of 3° is selected because for such a low elevation angle the atmospheric light

349 paths and thus the O₄ absorption are rather large. Moreover, as can be seen in Fig. 2, the O₄
350 (d)AMFs for 3° are very similar to those for 1° and 6°, especially on 8 July 2013. Sensitivity
351 studies showed that a wrong elevation calibration ($\pm 0.5^\circ$) led to to only small changes (<1%)
352 of the O₄ (d)AMFs. Changes of the field of view between 0.2 and 1.1° led to even smaller
353 differences. This These indicates that possible uncertainties of the calibration of the
354 elevation angles of the instruments can be neglected. Here it is interesting to note that on 18
355 June even slightly lower O₄ (d)AMFs are found for the low elevation angles. This is in
356 agreement with the finding of high aerosol extinction in a shallow layer above the surface (see
357 Fig. 1). The azimuth angle of 51° is chosen, because it was the standard viewing direction
358 during the MAD-CAT campaign and measurements for this direction are available from
359 different instruments.

360 b) The quantitative comparison for 3° elevation and azimuth of 51° is also extended to the
361 periods prior and after the middle periods of the selected days. However, to minimise the
362 computational efforts, some sensitivity studies are not carried out for the first and last periods.
363 c) The comparison is extended to more elevation angles (1°, 3°, 6°, 10°, 15°, 30°, 90°) and
364 azimuth angles (51°, 141°, 231°, 321°). For this comparison only the standard settings for the
365 DOAS analysis and the radiative transfer simulations are applied (see Tables 6 and 7). The
366 comparison results for the MPIC MAX-DOAS measurements are shown in appendix A2. The
367 purpose of this comparison is to check whether for other viewing angles similar results are
368 found as for 3° elevation at 51° azimuth direction.

369 3.3 Quantitative comparison for 3° elevation in standard azimuth direction

370 Fig. 3 presents a comparison of the measured and simulated O₄ (d)AMFs for 3° elevation and
371 51° azimuth on both days. For the spectral analysis and the radiative transfer simulations the
372 respective ‘standard settings’ (see Tables 6 and 7) were used. On 8 July the simulated O₄
373 (d)AMFs systematically underestimate the measured O₄ (d)AMFs by up to 40%. Similar
374 results are also obtained for other elevation and azimuth angles (see appendix A1A2), the
375 differences becoming smaller towards higher elevation angles. In contrast, no systematic
376 underestimation is observed for most of 18 June. For some periods of that day the simulated
377 O₄ (d)AMFs are even larger than the measured O₄ (d)AMFs. However, here it should be
378 noted that the aerosol extinction profile of the ‘standard settings’ (using linear extrapolation
379 below 180 m where no ceilometer data are available) probably underestimates the aerosol
380 extinction close to the surface. If instead a modified aerosol profile with strongly increased
381 aerosol extinction below 180 m and the maximum AOD during that period is used (see Fig.
382 A31 in appendix A5) the corresponding (d)AMFs fall below the measured O₄ (d)AMFs
383 (green curves in Fig. A4 in appendix A2). More details on the extraction of the aerosol
384 extinction profiles are given in section 4.2.2 and appendix A5).

385 The average ratio of simulated to measured (d)AMFs (for the standard settings) during the
386 middle periods on both days are given in Table 8. For 18 June they are close to unity, for 8
387 July they are much lower (0.83 for the AMF, and 0.69 for the dAMF).

392 4 Estimation of the uncertainties of the different processing steps

393 There are 3 major processing steps, for which the uncertainties are quantified in this section:
394 a) The determination of the O₄ height profiles and corresponding O₄ vertical column densities.
395 b) The simulation of O₄ (d)AMFs by the forward model
396 c) The analysis of O₄ (d)AMFs from the MAX-DOAS measurements.

397 4.1 Determination of the vertical O₄ profile and the O₄ VCD

400
401 The O₄ VCD is required for conversion of measured (d)SCDs into (d)AMFs (eq. 1). O₄
402 profiles are also needed for the calculation of O₄ (d)AMFs. The accuracy of the calculated O₄
403 height profile and the O₄ VCD depends in particular on two aspects:

404 a) is profile information on temperature, pressure and (relative) humidity available?
405 b) what is the accuracy of these data sets?

406 Additional uncertainties are related to the details of the calculation of the O₄ concentration
407 and O₄ VCDs from these profiles. Both error sources are investigated in the following sub
408 sections.

409

410 4.1.1 Extraction of vertical profiles of temperature and pressure

411

412 The procedure of extracting temperature and pressure profiles depends on the availability of
413 measured profile data or surface measurements. If profile data are available (e.g. from sondes
414 or models) they could be directly used. If only surface measurements are available, vertical
415 profiles of temperature and pressure could be calculated making assumptions on the lapse rate
416 (here we assume a value of -0.65 K / 100 m). If no measurements or model data are available,
417 profiles from the US standard atmosphere might be used (United States Committee on
418 Extension to the Standard Atmosphere, 1976). In appendix A3 the different procedures are
419 described in detail for the two days of the MAD-CAT campaign. For these days the optimum
420 choice was to combine the model data and the surface measurements. In that way, the diurnal
421 variation in the boundary layer could be considered.

422 ~~For the two selected days during the MADCAT campaign two data sets of temperature and~~
423 ~~pressure are available: surface measurements close to the measurement site and vertical~~
424 ~~profiles from ECMWF ERA-Interim re-analysis data (see Table 5). Both data sets are used to~~
425 ~~derive the O₄-concentration profiles for the three selected periods on both days. The general~~
426 ~~procedure is that first the temperature profiles are determined. In a second step, the pressure~~
427 ~~profiles are derived from the temperature profiles and the measured surface pressure. For the~~
428 ~~temperature profile extraction, three height layers are treated differently:~~

429 ~~below 1 km~~

430 ~~Between the surface (~150 m above sea level) and 1 km, the temperature is linearly~~
431 ~~interpolated between the average of the in situ measurements of the respective period and the~~
432 ~~ECMWF data at 1 km (see next paragraph). This procedure is used to account for the diurnal~~
433 ~~variation of the temperature close to the surface. Here it is important to note that for this~~
434 ~~surface near layer the highest accuracy is required, because a) the maximum O₄-concentration~~
435 ~~is located near the surface, and b) the MAX-DOAS measurements are most sensitive close to~~
436 ~~the surface.~~

437 ~~1 km to 20 km~~

438 ~~In this altitude range, the diurnal variation of the temperature becomes very small. Thus the~~
439 ~~average of the four ECMWF profiles of each day is used (for simplicity, a 6th-order~~
440 ~~polynomial is fitted to the ECMWF data).~~

441 ~~Above 20 km~~

442 ~~In this altitude range the accuracy of the temperature profile is not critical and thus the~~
443 ~~ECMWF temperature profile for 00:00 UTC of the respective day is used for simplicity.~~

444 ~~The temperature profiles for 8 July 2013 extracted in this way are shown in Fig. 4 (left). Close~~
445 ~~to the surface the temperature variation during the day is about 10 K.~~

446 ~~In the next step, the pressure profiles are determined from the surface pressure (obtained from~~
447 ~~the in situ measurements) and the extracted temperature profiles according to the ideal gas~~
448 ~~law. In principle the effect of atmospheric humidity could also be taken into account, but the~~
449 ~~effect is very small for surface near layers and is thus ignored here. The derived pressure~~

450 profiles for 8 July 2013 are shown in Fig. 4 (right). Excellent agreement with the
451 corresponding ECMWF pressure profiles is found.

452 Here it should be noted that in principle also the ECMWF pressure profiles could be used.
453 However, we chose to determine the pressure profiles from the surface pressure and the
454 extracted temperature profiles, because this procedure can also be applied if no ECMWF data
455 (or other information on temperature and pressure profiles) is available.

456 If no profile data (e.g. from ECMWF) are available, temperature and pressure profiles can
457 also be extrapolated from surface measurements e.g. by assuming a constant lapse rate of
458 $-0.65 \text{ K} / 100 \text{ m}$ for the altitude range between the surface and 12 km, and a constant
459 temperature above 12 km (as stated above, uncertainties at this altitude range have only a
460 negligible effect on the O_4 VCD). If no measurements or model data are available at all, a
461 fixed temperature and pressure profile can be used, e.g. the US standard atmosphere (United
462 States Committee on Extension to the Standard Atmosphere, 1976).

463 A comparison of the different temperature profiles extracted by the different methods for two
464 selected periods on both days is shown in Fig. 5. For 8 July (right), rather good agreement is
465 found, but for 18 June (left) the agreement is worse (differences up to 20 K). Of course, the
466 differences between the true and the US standard atmosphere profiles can become even larger,
467 depending on location and season. So the use of a fixed temperature and pressure profile
468 should always be the last choice. In contrast, the simple extrapolation from surface values can
469 be very useful if no profile data are available, because the uncertainties of this method are
470 usually smallest at low altitudes, where the bulk of O_4 is located.

471 4.1.2 Calculation of O_4 concentration profiles and O_4 VCDs

472 From the temperature and pressure profiles the oxygen (O_2) concentration is calculated. Here
473 also the effect of the atmospheric humidity profiles should be taken into account (see
474 below appendix A3), because it can have a considerable effect on the surface-near layers (at
475 least for temperatures of about $> 20^\circ\text{C}$). Finally, the square of the oxygen concentration is
476 calculated and used as proxy for the O_4 concentration (see Greenblatt et al., 1990). The
477 uncertainties of the derived O_4 concentration (and the corresponding O_4 VCD) caused by the
478 uncertainty of the input profiles is estimated by varying the input parameters (for details see
479 appendix A3). The following uncertainties are derived:

480 The variation of the temperature (whole profile) by about 2 K leads to variations of the O_4
481 concentration (or O_4 VCD) by about 0.8%.

482 The variation of the surface pressure by about 3 hPa leads to variations of the O_4
483 concentration (or O_4 VCD) by about 0.7%.

484 The effect of uncertainties of the relative humidity depends strongly on temperature: For
485 surface temperatures of 0°C , 10°C , 20°C , 30°C , and 35°C a variation of the relative humidity
486 of 30% leads to variations of the O_4 concentration (or O_4 VCDs) of about 0.15%, 0.3%, 0.6%,
487 1.2%, and 1.6%, respectively. If the effect of atmospheric humidity is completely ignored (dry
488 air is assumed), the resulting O_4 concentrations (or O_4 VCDs) are systematically
489 overestimated by about 0.3%, 0.7%, 1.3%, 2.5%, and 4% for surface temperatures of 0°C ,
490 10°C , 20°C , 30°C , and 35°C , respectively (assuming a relative humidity of 70%). In this
491 study we used the relative humidity measured by the in situ sensors. We took these values not
492 only for the surface layers, but also for the whole troposphere. Here it should be noted that the
493 related uncertainties of the absolute humidity decrease quickly with altitude because the
494 absolute humidity itself decrease quickly with altitude. Since both selected days were warm or
495 even hot summer days, we estimate the uncertainty of the O_4 concentration and O_4 VCDs due
496 to uncertainties of the relative humidity to 1% and 0.4% on 18 June and 8 July, respectively.

497 For both selected days during the MAD-CAT campaign Assuming that the uncertainties of
498 the three input parameters are independent, the total uncertainty related to the is se factors is

501 estimated to be about 1.5% assuming that the uncertainties of the individual input
502 parameterinput parameters are independent.

503 Further uncertainties arise from the procedure of the vertical integration of the O₄
504 concentration profiles. We tested the effect of using different vertical grids and altitude
505 ranges. It is found that the vertical grid should not be coarser than 100 m (for which a
506 deviation of the O₄ VCD of 0.3% compared to a much finer grid is found). If e.g. a vertical
507 grid with 500 m layers is used, the deviation increases to about 1.3%. The integration should
508 be performed over an altitude range up to 30 km. If lower maximum altitudes are used, the O₄
509 VCD will be substantially underestimated: deviations of 0.1 %, 0.5 %, and 11% are found if
510 the integration is performed only up to 25 km, 20 km, and 10 km, respectively. Here it should
511 be noted that the exact consideration of the altitude of the measurement site is also very
512 important: A deviation of 50 m already leads to a change of the O₄ VCD by 1%. For the
513 MAD-CAT measurements the altitude of the instruments is 150m ±20m.

514 Finally, the effects of individual extraction and integration procedures are investigated by
515 comparing the results from different groups (see Fig. 6, and Fig. A5 in appendix A3). Except
516 for some extreme cases, the extracted temperatures typically differ by less than 3 K below 10
517 km. However, the deviations are typically larger for the profiles extrapolated from the surface
518 values and in particular for the US standard atmosphere (up to > 10 K below 10 km). Also the
519 variations of the extracted pressure profiles are in general rather small (< 1% below 10 km,
520 except one obvious outlier). Also here the deviations of the profiles extrapolated from the
521 surface values and especially the US standard atmosphere are much larger (up to > 5 % below
522 10 km). The resulting deviations of the O₄ concentration from the different extractions are
523 typically <3% below 10 km (and up to > 20 % belowabove 10 km for the US standard
524 atmosphere).

525 In Fig. 7 the O₄ VCDs calculated for the O₄ profiles extracted from the different groups and
526 for the profiles extrapolated from the surface values and the US standard atmosphere are
527 shown. The VCDs for the profiles extracted by the different groups agree within 2.5%. The
528 deviations for the profiles extrapolated from the surface values are only slightly larger
529 (typically within 3%), but show a large variability throughout the day, which is caused by the
530 systematic increase of the surface temperature during the day (with temperature inversions in
531 the morning on the two selected days). The deviations of the US standard atmosphere are up
532 to 5% (but can of course be larger for other seasons and locations, see also Ortega et al.
533 (2016).

534 Ultimately, the accuracy with which O₄ concentrations can be calculated is limited by the
535 assumption that O₄ (O₂-O₂) is pure collision induced absorption. If the oxygen concentration
536 profile is well known, the uncertainty due to bound O₄ is smaller 0.14% in Earth's atmosphere
537 (Thalman and Volkamer, 2013).

538 Together with the uncertainties related to the input data sets, the total uncertainty of the O₄
539 VCDs determined for both selected days is estimated as 3%.

540 4.2 Uncertainties of the O₄ (d)AMFs derived from radiative transfer simulations

543 The most important errors of the simulated O₄ (d)AMFs are related to the uncertainties of the
544 input parameters used for the simulations, in particular the aerosol properties. Further
545 uncertainties are caused by imperfections of the radiative transfer models. These error sources
546 are discussed and quantified in the following sub sections.

548 4.2.1 Uncertainties of the O₄ (d)AMFs caused by uncertainties of the input parameters

550 In this section the effect of the uncertainties of various input parameters on the O₄ (d)AMFs is
551 investigated. The general procedure is that the input parameters are varied individually and

552 the corresponding changes of the O₄ (d)AMFs compared to the standard settings are
553 quantified.

554 First, the effect of the O₄ profile shape is investigated. In contrast to the effect of the
555 (absolute) profile shape on the O₄ VCD (section 4.1), here the effect of the relative profile
556 shape on the O₄ AMF is investigated. The O₄ (d)AMFs simulated for the O₄ profiles extracted
557 by the different groups (and for those derived from the US standard atmosphere and the
558 profiles extrapolated from the surface values, see section 4.1) are compared to those for the
559 MPIC O₄ profiles (using the standard settings). The corresponding ratios are shown in Fig. A6
560 and Table A4 in appendix A4. For the O₄ profiles extracted by the different groups, and for
561 O₄ profiles extrapolated from the surface values, small variations are found (typically < 2%).
562 For the O_{4-US} standard atmosphere larger deviations (up to 7%) are derived.

563 Next the effect of the aerosol extinction profile is investigated. In this study, aerosol
564 extinction profiles are derived from the combined ceilometer and sun photometer
565 measurements (see Table 5). In short, the ceilometer measurements of the attenuated
566 backscatter are scaled by the simultaneously measured aerosol optical depth (AOD) from the
567 sun photometer to obtain the aerosol extinction profile. Also the self-attenuation of the aerosol
568 is taken into account. The different steps are illustrated in Fig. 8 and described in detail in
569 appendix A5. In the extraction procedure, several assumptions have to be made: First, the
570 ceilometer profiles have to be extrapolated for altitudes below 180 m, for which the
571 ceilometer is not sensitive. Furthermore, they have to be averaged over several hours and are
572 in addition vertically smoothed (above 2 km) to minimise the rather large scatter. Finally,
573 above 5 to 6 km (depending on the ceilometer profiles) the extinction is set to zero because of
574 the further increasing scatter and the usually small extinctions. Another assumption is that the
575 LIDAR ratio is independent of altitude, which is typically not strictly fulfilled (the LIDAR
576 ratio describes the ratio between the extinction and backscatter probabilities of the molecules
577 and aerosol particles).

578 ~~Some of t~~These uncertainties are quantified by sensitivity studies, in particular the effect of
579 the extrapolation below 180 m and the altitude above which the aerosol extinction is set to
580 zero. Other uncertainties, like the effect of the assumption of a constant LIDAR ratio are more
581 difficult to quantify without further information (see below). ~~While a constant LIDAR ratio is~~
582 ~~probably a good assumption for 8 July, for 18 June the surface measurements indicate that the~~
583 ~~aerosol properties strongly change with time. Thus the LIDAR ratio might also vary stronger~~
584 ~~with altitude on that day.~~ The effect of temporal averaging and smoothing is probably
585 negligible for 8 July, because similar height profiles are found for all three periods of that day,
586 but on 18 June the effect might be more important.

587 Fig. 9 shows a comparison of the aerosol extinction profiles extracted by the different groups
588 for the three periods on both days. Especially on 8 July systematic differences are found.
589 They are caused by the different altitudes, above which the aerosol extinction is set to zero. In
590 combination with the scaling of the profiles with the AOD obtained from the sun photometer,
591 this also influences the extinction values close to the surface. Deviations up to 18% are found
592 for the first period of 8 July. These deviations also have an effect on the corresponding O₄
593 (d)AMFs, where higher values are obtained for the profiles (INTA and IUPB 300m) which
594 were extracted for a larger altitude range (Fig. A7 and Table A5 in the appendix A4). Here it
595 is interesting to note that these differences are not related to the direct effect of the aerosol
596 extinction at high altitude, but to the corresponding (via the scaling with the AOD) decrease
597 of the aerosol extinction close to the surface. Larger deviations (up to 4%) are found for 8
598 July, while the deviations on 18 June are within 3%.

599 In Fig. A8 and Table A6 in appendix A4, the effect of the different extrapolations of the
600 aerosol extinction profile below 180 m on the O₄ (d)AMFs is quantified. Similar deviations
601 (up to 5 %) are found for both days.

602 Finally, we investigated the effect of changing aerosol optical properties with altitude
603 (changing LIDAR ratio). Such effects are in particular important if the wavelength of the
604 ceilometer measurements (1064 nm) differs largely from that of the MAX-DOAS observations
605 (360 nm). Based on the partitioning in fine and coarse mode aerosols derived from the sun
606 photometer observations, as well as the corresponding phase functions and optical depths, the
607 sensitivity of the ceilometer to fine mode aerosols were estimated (for details see appendix
608 A5). While for 18 June the contribution of the fine mode to the ceilometer signal is about 32%
609 on 8 July it is much larger (about 82 %). Thus it can be concluded that the aerosol extinction
610 profile derived from the ceilometer is largely representative for the fine mode aerosols on that
611 day. Nevertheless, the remaining uncertainties of the aerosol extinction profile at 360 nm
612 together with the assumption that the coarse aerosols indicate that the aerosol extinction
613 profile extracted assuming a constant LIDAR ratio and that the ceilometer measurements at
614 1064 nm were representative also for 360 nm had to be modified (see appendix A5). The
615 corresponding repartitioning led to a decrease of the aerosol extinction close to the surface
616 which is balanced by an increase at higher altitudes (see Fig. A34). The O_4 dAMFs calculated
617 for the modified profile are by about 15 % larger than those for the standard settings (for
618 details see appendix A5).

619 The effect of elevated aerosol layers (see Ortega et al., 2016) was further investigated by
620 systematic sensitivity studies (appendix A6). On both selected days enhanced aerosol
621 extinction was found at elevated layers (Fig. 9). Compared to those reported by Ortega et al.
622 (2016) the profiles extracted in this study reach even up to higher altitudes. For the
623 investigation of the effect of changes of the aerosol extinction at different altitudes, the
624 aerosol extinction profile on 8 July was subdivided into 3 layers (0-1.7 km; 1.7 – 4.9 km; 4.9
625 – 7 km), and the extinction in the individual layers was increased by +40 %. It was found that
626 even a strong increase of the aerosol extinction at high altitudes by 40% leads only to an
627 increase of the O_4 dAMFs by 7 %.

628 Also the effect of horizontal gradients should be briefly discussed. For the selected periods of
629 both days, the wind direction and wind speed were rather constant. On 18 June the wind
630 direction was between 80° and 150° with respect to North, and the wind speed was about 2
631 m/s. On 8 July the wind direction was between 70° and 90° (the wind came from almost the
632 same direction at which the instruments were looking), and the wind speed was about 3 m/s.
633 During the 4 hours of the selected period on 8 July, the air masses moved over a distance of
634 about 40 km. During the 3 hours of the selected period on 18 June, the air masses moved over
635 a distance of about 20 km. These distances are larger than the distances for which the MAX-
636 DOAS observations are sensitive (about 5 – 15 km). Since also the AOD and the aerosol
637 extinction profiles were rather constant during both selected periods, we conclude that for the
638 measurements considered here horizontal gradients can be neglected. Here it should also be
639 noted that the discrepancies between measurements and simulations were simultaneously
640 observed at all 4 azimuth directions.

641 In Fig. A9 and Table A7 in appendix A4, the effect of different single scattering albedos
642 (between 0.9 and 1) on the O_4 (d)AMFs is quantified. The effect on the O_4 (d)AMFs is up 4 %
643 on 18 June and up to 2 % on 8 July 2013.

644 The impact of the aerosol phase function is investigated in two ways: First, simulation results
645 are compared for Henyey Greenstein phase functions with different asymmetry parameters.
646 The corresponding results are shown in Fig. A10 and Table A8 in appendix A4. The
647 differences of the O_4 (d)AMFs for the different aerosol phase functions are rather strong: up
648 to 3% for the O_4 AMFs and up to 8% for the O_4 dAMFs (larger uncertainties for the dAMFs
649 are found because of the strong influence of the phase function on the 90° observations). Here
650 it should be noted that the actual deviations from the true phase function might be even larger.
651 In order to better estimate these uncertainties, also simulations for phase functions derived

653 from the sun photometer measurements based on Mie theory (in the following referred to as
654 Mie phase functions) were performed. A comparison of these Mie phase functions with the
655 Henyey Greenstein phase functions is shown in Fig. 10. Large differences, especially in
656 forward direction are obvious. The O₄ (d)AMFs for the Mie phase functions are compared to
657 the standard simulations (using the HG phase function for an asymmetry parameter of 0.68) in
658 Fig. A11 and Table A9 in Appendix A4. Again rather large deviations are found, which are
659 larger on 18 June (up to 9 %) than on 8 July (up to 5%).
660 In Fig. A12 and Table A10 in Appendix A4, the effect of different surface albedos on the O₄
661 (d)AMFs is quantified. For the considered variations (0.03 to 0.1) the changes of the O₄
662 (d)AMFs are within 2 %.

663

664 **4.2.2 Uncertainties of the O₄ (d)AMFs caused by imperfections of the radiative transfer 665 models**

666

667 The radiative transfer models used in this study are well established and showed very good
668 agreement in several intercomparison studies (e.g. Hendrick et al., 2006; Wagner et al., 2007;
669 Lorente et al., 2017). Nevertheless, they are based on different methods and use different
670 approximations (e.g. with respect to the Earth's sphericity). Thus we compared the simulated
671 O₄ (d)AMFs for both days in order to estimate the uncertainties associated to these
672 differences. In Fig. A13 and Table A11 (appendix A4), the comparison results are shown.
673 They agree within a few percent with slightly larger differences for 18 June (up to 6 %) than
674 for 8 July (up to 3 %).

675 So far, all radiative transfer simulations were carried out without considering polarisation.
676 Thus in Fig. A14 and Table A12 in appendix A4, the results with and without considering
677 polarisation are compared. The corresponding differences are very small (<1%).

678

679 **4.2.3 Summary of uncertainties of the O₄ AMF from radiative transfer simulations**

680

681 Table 9 presents and overview on the different sources of uncertainties of the simulated O₄
682 (d)AMFs derived from the comparison of the results from different groups and the sensitivity
683 studies. The uncertainties are expressed as relative deviations from the results for the standard
684 settings (see Table 6) derived by MPIC using MCARTIM.

685 In general, larger uncertainties are found for the O₄ dAMFs compared to the O₄ AMFs. This is
686 expected because the uncertainties of the O₄ dAMFs contain the uncertainties of two
687 simulations (at 90° elevation and at low elevation). Another general finding is that the
688 uncertainties on 18 June are larger than on 8 July. This finding is mainly related to the larger
689 uncertainties due to the aerosol phase function, which has an especially strong forward peak
690 on 18 June. Also the error contributions from the O₄ profile extraction, the choice of the
691 radiative transfer model and the extrapolation of the aerosol extinction below 180 m are larger
692 on 18 June than on 8 July. These higher uncertainties are probably mainly related to the high
693 aerosol extinction close to the surface on 18 June (see section 5.1, and appendices A2 and
694 A5).

695 For the total uncertainties two values are given in Table 9: The 'average deviation' is the sum
696 of all systematic deviations of the individual uncertainties (the corresponding mean of the
697 maximum and minimum values). The second quantity (the 'range of uncertainties') is
698 calculated from half the individual uncertainty ranges by assuming that they are independent.

699 Finally, it should be noted that for some error sources (e.g. the effects of the surface albedo or
700 the single scattering albedo) the given numbers probably overestimate the true uncertainties,
701 while for others, e.g. the uncertainties related to the aerosol extinction profiles or the phase
702 functions they possibly underestimate the true uncertainties (although reasonable assumptions

were made). The two latter error sources are especially large for 18 June. The differences between both days are discussed in more detail in section 5.

4.3 Uncertainties of the spectral analysis

The uncertainties of the spectral analysis are caused by different effects:

-the specific settings of the spectral analysis like the fit window or the degree of the polynomial. Of particular interest is the effect of choosing different O₄ cross sections as well as its temperature dependence.

-the properties (and imperfections) of the MAX-DOAS instruments

-the effect of different analysis software and implementations

-the effect of the wavelength dependence of the AMF across the fit window.

These error sources are discussed and quantified in the following sub sections.

4.3.1 Comparison of O₄ (d)AMFs derived from the synthetic spectra with O₄ (d)AMFs directly obtained from the radiative transfer simulations

Synthetic spectra for both selected days were simulated using the radiative transfer model SCIATRAN (for details see section 2.4 and Table A3 in appendix A1). While spectra for the whole day are simulated (for the viewing geometry see Table A2 in appendix A1) it should be noted that the aerosol properties during the middle periods are used also for the whole day (to minimise the computational efforts). The spectra are analysed using the standard settings and the derived O₄ (d)SCDs are converted to O₄ (d)AMFs using eq. 1. In addition to the spectra, also O₄ (d)AMFs at 360 nm are simulated directly by the RT models using exactly the same settings. These O₄ (d)AMFs are used to test whether the spectral retrieval results are indeed representative for the simulated O₄ (d)AMFs at 360 nm.

Spectra are simulated with and without considering the temperature dependence of the O₄ cross section. Also one version of synthetic spectra with added random noise is processed.

First, the synthetic spectra are analysed using the standard settings (see Table 7). Examples of the O₄ fits for synthetic (and measured) spectra are shown in Fig. 11. Here it is interesting to note that the ratios of the results for the measured spectrum and the simulated spectra are between 0.68 and 0.74, similar to ratio for the dAMFs on 8 July shown in Table 8.

In Fig. 12 the ratios of the O₄ (d)AMFs derived from the synthetic spectra versus those directly obtained from the radiative transfer simulations at 360 nm are shown. In the upper part (a) the results for synthetic spectra considering the temperature dependence of the O₄ cross section are presented (without noise). Systematically enhanced ratios are found in the morning and evening, while for most of the day the ratios are close to unity. The higher values in the morning and evening are probably partly caused by the increased light paths through higher atmospheric layers (with lower temperatures) when the solar zenith angle is high. Interestingly, if the temperature dependence of the O₄ cross section is not taken into account (Fig. 12 b), still slightly enhanced ratios during the morning and evening are found, which can not be explained anymore by the temperature dependence of the O₄ cross section. Thus we speculate whether part of the enhanced values at high SZA are probably caused by the wavelength dependence of the O₄ AMFs. Nevertheless, for most of the day the ratio is very close to unity indicating that for SZA < 75° the O₄ (dAMFs) obtained from the spectral analysis are almost identical to the O₄ (dAMFs) directly obtained from the radiative transfer simulations (at 360 nm).

In Fig. 12 c results for spectra with added random noise (without consideration of the temperature dependence of the O₄ cross section) are shown. On average similar results as for the spectra without noise (Fig. 12 b) are found but the results now show a large scatter. From

754 these results and also the spectral analyses (Fig. 11) we conclude that the noise added to the
755 synthetic spectra overestimates that of the real measurements.

756 In Table A13 in appendix A4 the average ratios for the middle periods on both selected days
757 are shown. They deviate from unity by up to 2% indicating that the wavelength dependence of
758 the O₄ (d)AMF is negligible for the considered cases for SZA < 75°.

760 4.3.2 Sensitivity studies for different fit parameters

761 In this section the effect of the choice of several fit parameters on the derived O₄ (d)AMFs is
762 investigated using both measured and synthetic spectra. Only one fit parameter is varied for
763 each individual test, and the results are compared to those for the standard fit parameters (see
764 Table 7).

765 First the fit window is varied. Besides the standard fit window (352 to 387 nm), which
766 contains two O₄ bands, also two fit windows towards shorter wavelengths are tested: 335 –
767 374 nm (including two O₄ bands) and 345 – 374 nm (including one O₄ band at 360 nm). The
768 ratios of the derived O₄ (d)AMFs versus those for the standard analysis are shown in Fig. A15
769 and Table A14 in appendix A2. On 18 June rather large deviations of the O₄ (d)AMFs are
770 found for both measured (-12%) and synthetic spectra (-5%) for the spectral range 335 to 374
771 nm. On 8 July the corresponding differences are smaller (-6% and -2% for measured and
772 synthetic spectra, respectively). For the spectral range 345 – 374 nm, smaller differences of
773 only up to 1% are found for both days. The reason for the larger deviations on 18 June for the
774 spectral range 335 – 374 nm is not clear. One possible reason could be the differences of the
775 Ångström parameters (see Fig. 1) and phase functions (see Fig 10).

776 In Fig. A16 and Table A15 the results for different degrees of the polynomial used in the
777 spectral analysis are shown. For the measured spectra systematically higher O₄ (d)AMFs (up
778 to 6%) than for the standard analysis are found when using lower polynomial degrees. For the
779 synthetic spectra the effect is smaller (<3%).

780 In Fig. A17 and Table A16 the results for different intensity offsets are shown. Again, for the
781 measured spectra systematically higher O₄ (d)AMFs (up to 16%) than for the standard
782 analysis are found when reducing the order of the intensity offset, while for the synthetic
783 spectra the effect is smaller (<3%). Higher order intensity offsets might compensate for
784 wavelength dependent offsets (e.g. spectral straylight), which can be important for real
785 measurements, while the synthetic spectra do not contain such contributions.

786 In Fig. A18 and Table A17 the results for spectral analyses with only one Ring spectrum are
787 shown. In contrast to the standard analysis, which includes two Ring spectra (one for clear
788 and one for cloudy sky, see Wagner et al., 2009), only the Ring spectrum for clear sky is used.
789 For both selected days, only small deviations (within 2%) compared to the standard analysis
790 are found.

793 4.3.3 Sensitivity studies using different trace gas absorption cross sections

794 In this section the impact of different trace gas absorption cross sections on the derived O₄
795 (d)AMFs is investigated.

796 In Fig. A19 and Table A18 the results for using two NO₂ cross sections (294 and 220 K)
797 compared to the standard analysis (using only a NO₂ cross section for 294 K) are shown. The
798 results are almost the same as for the standard analysis.

799 In Fig. A20 and Table A19 the results for using an additional wavelength-dependent NO₂
800 cross section compared to the standard analysis (using only one NO₂ cross section) are shown.
801 The second NO₂ cross section is calculated by multiplying the original cross section with
802 wavelength (Pukite et al., 2010). Again, only small deviations of the results from the standard
803 analysis (1% for the measured spectra, and 2% for the synthetic spectra are found.

805 In Fig. A21 and Table A20 results for using and additional wavelength-dependent O_4 cross
806 sections compared to the standard analysis (using only one O_4 cross section) are shown. The
807 second O_4 cross section is calculated like for NO_2 , but also an orthogonalisation with respect
808 to the original O_4 cross section (at 360 nm) is performed. The derived O_4 (d)AMFs are almost
809 identical to those from the standard analysis (within 1%).

810 For the spectral retrieval of HONO in a similar spectral range, a significant impact of water
811 vapour absorption around 363 nm was found in Wang et al. (2017c) and Lampel et al. (2017).
812 In Fig. A22 and Table A21 the O_4 results for including a H_2O cross section (Polyansky et al.,
813 2018) compared to the standard analysis (using no H_2O cross section) are shown. The results
814 are almost identical to those from the standard analysis (within 1%).

815 In Fig. A23 and Table A22 the results for including a $HCHO$ cross section (Polyansky et al.,
816 2018) compared to the standard analysis (using no $HCHO$ cross section) are shown.
817 Especially for 18 June a large systematic effect is found: the O_4 dAMFs are by 4 % or 6 %
818 smaller than for the standard analysis for measured and synthetic spectra, respectively. On 8
819 July the underestimation is smaller (2% and 3% for measured and synthetic spectra,
820 respectively).

821 822 **4.3.4 Effect of using different O_4 cross sections**

823 In Fig. A24 and Table A23 the results for different O_4 cross sections are compared to the
824 standard analysis (using the Thalman O_4 cross section). The results for both days are almost
825 identical. For the real measurements, the derived O_4 dAMFs using the Hermans and
826 Greenblatt cross sections are by 3% smaller or 8 % larger than those for the standard analysis,
827 respectively. However, if the Greenblatt O_4 cross section is allowed to shift during the
828 spectral analysis, the overestimation can be largely reduced to only +3 %. This confirms
829 findings from earlier studies (e.g. Pinardi et al., 2013) that the wavelength calibration of the
830 original data sets is not very accurate.

831 For the synthetic spectra slightly different results than for the real measurements are found for
832 the Hermans O_4 cross section. The reason for these differences is not clear. However, here it
833 should be noted that the temperature dependent O_4 absorption in the synthetic spectra does
834 probably not exactly represent the true atmospheric O_4 absorption.

835 836 **4.3.5 Effect of the temperature dependence of the O_4 cross section**

837 The new set of O_4 cross sections provided by Thalman and Volkamer (2013) allows to
838 investigate the temperature dependence of the atmospheric O_4 absorptions in detail. They
839 provide O_4 cross sections measured at five temperatures (203, 233, 253, 273, 293 K) covering
840 the range of temperatures relevant for atmospheric applications. Using these cross sections,
841 the effect of the temperature dependence of the O_4 absorptions is investigated in two ways:

842 a) In a first test, synthetic spectra are simulated for different surface temperatures assuming a
843 fixed lapse rate. These spectra are then analysed using the O_4 cross section for 293K (which is
844 usually used for the spectral analysis of O_4). From this study the magnitude of the effect of the
845 temperature dependence of the O_4 cross section on MAX-DOAS measurements can be
846 quantified.

847 b) In a second test, measured and synthetic spectra for both selected days are analysed with
848 O_4 cross sections for different temperatures. From this study it can be seen to which degree
849 the temperature dependence of the O_4 cross section can be already corrected during the
850 spectral analysis (if two O_4 cross sections are used simultaneously).

851 For the first study, MAX-DOAS spectra are simulated in a simplified way:

852 -Atmospheric temperature profiles are constructed for surface temperatures between 220 K
853 and 310 K in steps of 10 K assuming a fixed laps rate of -0.656 K / 100 m.

856 -For each altitude layer (vertical extension: 20 m below 500m, 100 m between 500 m and 2
857 km, 200 m between 2 km and 12 km, 1 km above) the O₄ concentrations (calculated from the
858 US standard atmosphere) are multiplied with the corresponding differential box-AMFs
859 calculated for typical atmospheric conditions and viewing geometries (see Fig. A25 in
860 appendix A4).

861 -High resolution absorption spectra are calculated by applying the Beer-Lambert-law for each
862 height layer using the O₄ cross section of the respective temperature (interpolated between the
863 two adjacent temperatures of the Thalman and Volkamer data set).

864 -The derived high resolution spectra are convolved with the instrument slit function (FWHM
865 of 0.6 nm).

866 -The logarithm of the ratio of the spectra for the low elevation and zenith is calculated and
867 analysed using the O₄ cross section for 293 K.

868 -The derived O₄ dAMFs are divided by the corresponding dAMFs directly obtained from the
869 radiative transfer simulations.

870 These calculated ratios as function of the surface temperature are shown in Fig. 13. A strong
871 and systematic dependence on the surface temperature is found (15 % for a change of the
872 surface temperature between 240 and 310 K). However, except for measurements at polar
873 regions, the deviations are usually small. Since for both selected days the temperatures were
874 rather high (indicated by the two coloured horizontal bars in the figure), the effect of the
875 temperature dependence of the O₄ absorption for the middle periods of both days is very small
876 (-1 to -2% for 18 June, and 0 to +1% on 8 July). It should be noted that the results shown in
877 Fig. 13 are obtained for generalised settings of the radiative transfer simulations. Thus it is
878 recommended that future studies should investigate the effect of the temperature dependence
879 in more detail and using the exact viewing geometry for individual observations. However,
880 since the temperatures on both selected days were rather high, for this study the
881 simplifications of the radiative transfer simulations have no strong influence on the derived
882 results.

883 In the second test the measured and synthetic spectra are analysed using O₄ cross sections for
884 different temperatures. The corresponding results are shown in Fig. A26 and Table A24.

885 If only the O₄ cross section at low temperature (203 K) is used, the derived O₄ AMFs and
886 dAMFs are by about 16% and 30% smaller than for the standard analysis (using the O₄ cross
887 section for 293 K). These results are consistently obtained for the measured and synthetic
888 spectra. If, however, two O₄ cross sections (for 203 and 293 K) are simultaneously included in
889 the analysis, different results are obtained for the measured and synthetic spectra: for the
890 measured spectra the derived O₄ (d)AMFs agree within 4% with those from the standard
891 analysis. In contrast, for the synthetic spectra, the derived O₄ (d)AMFs are systematically
892 smaller (by about 6 to 18 %). This finding was not expected, because exactly the same cross
893 sections were used for both the simulation and the analysis of the synthetic spectra. Detailed
894 investigations (see appendix A4) led to the conclusion that there is a slight inconsistency in
895 the temperature dependence of the O₄ cross sections from Thalman et al. (2013): The ratio of
896 the peak values of the cross section at 360 and 380 nm changes in a non-continuous way
897 between 253 and 223 K (see Fig. A27 in appendix A4). The reason for this inconsistency is
898 currently not known. If these two O₄ bands are included in the spectral analysis (as for the
899 standard settings), the convergence of the spectral analysis strongly depends on the ability to
900 fit both O₄ bands well. Thus the fit results for both O₄ cross sections are mainly determined by
901 the relative strengths of both O₄ bands (see Fig. A27 in appendix A4). If instead a smaller
902 wavelength ranges is used containing only one absorption band (345 – 374 nm), the derived
903 O₄ (d)AMFs are in rather good agreement with the results of the analysis (using only the O₄
904 cross section for 293 K), see Table A25 in appendix A4. In that case, the convergence of the
905 fit mainly depends on the temperature dependence of the line width. It should be noted that
906 the non-continuous temperature dependence of the O₄ absorption cross section only affects

907 the analysis of the synthetic spectra, because for the simulation of the spectra all O₄ cross
908 sections for temperatures between 223 and 293 K were used. For the measured spectra, no
909 problems are found, because in the spectral analysis only the O₄ cross sections for 223 and
910 293 K were used.

911 In Fig. A28 in appendix A4 the ratios of both fit coefficients (for 203 and 293 K) as well as
912 the derived effective temperatures for the analyses of measured and synthetic spectra are
913 shown. For the measured spectra the ratios are close to zero and the derived temperatures are
914 close to 300K for most of the time (except in early morning and evening), because the
915 effective atmospheric temperature for both days is close to the temperature of the high
916 temperature O₄ cross section (293 K) (see Fig. 13). Similar results (at least around noon) are
917 also obtained for the synthetic spectra if the narrow spectral range (345 – 374 nm) is used. For
918 the standard fit range (including two O₄ bands), however, the ratios are much higher again
919 indicating the effect of the inconsistency of the temperature dependence of the O₄ cross
920 sections (see Fig. A27 in appendix A4).

921 4.3.6 Results from different instruments and analyses by different groups

922 In this section the effects of using measurements from different instruments and having these
923 spectra analysed by different groups are investigated. For that purpose three different
924 procedures are followed: First, MPIC spectra are analysed by other groups; second, the
925 spectra from ~~other instruments are analysed by MPIC~~ ~~non-MPIC instruments are analysed by~~
926 ~~the respective group~~; third, the spectra from ~~non-MPIC instruments~~ ~~other instruments~~ are
927 analysed ~~by the respective group by MPIC~~.

928 In Fig. 14a and Table A25 (in appendix A4) the comparison results of the analysis of MPIC
929 spectra by other groups versus the analysis of MPIC spectra by MPIC are shown. Especially
930 for 18 June rather large differences (between –6% / +5%) to the MPIC standard analysis are
931 found. Interestingly the largest differences are found in the morning when the aerosol
932 extinction close to the surface was strongest. On 8 July smaller differences (between –6% and
933 –1%) are found.

934 In Fig. 14b and Table A25 (in appendix A4) the comparison results of the analysis of spectra
935 from other instruments by MPIC versus the analysis of MPIC spectra by MPIC are shown.
936 For this comparison all analyses are performed in the spectral range 335 – 374 nm, because
937 the standard spectral range (352 – 387 nm) is not covered by all instruments. Again, the
938 largest differences are found for 18 June (up to $\pm 11\%$). For 8 July the differences reach up to
939 $\pm 6\%$, but for this day only a few measurements in the morning are available.

940 In Fig. 14c and Table A25 (in appendix A4) the comparison results of the analysis of spectra
941 from other instruments by the respective group versus the MPIC analysis by MPIC (standard
942 analysis) is shown. From this exercise the combined effects of different instrumental
943 properties and retrievals can be estimated. Interestingly, the observed differences are only
944 slightly larger than those for the analysis of the spectra from the different instruments by
945 MPIC (Fig. 14b). This indicates that the largest errors are related to the differences of the
946 different instruments and not to the settings and implementations of the different retrievals.
947 For the middle period of 18 June the uncertainties are within 12%. This range is also assumed
948 for 8 July. ~~Here it is interesting to note that the derived errors of the spectral analysis are~~
949 ~~probably not representative for most recent measurement campaigns. For example, during the~~
950 ~~CINDI-2 campaign (<http://www.tropomi.eu/data-products/cindi-2>) the deviations of the O₄~~
951 ~~spectral analysis results were much smaller than for the selected days during the MAD-CAT~~
952 ~~campaign.~~

953 4.3.7 Summary of uncertainties of the O₄ AMF from the spectral analysis

958 Table 10 presents an overview on the different sources of uncertainties of the measured O₄
959 (d)AMFs obtained in the previous sub-sections. The uncertainties are expressed as relative
960 deviations from the results for the standard settings (see Table 7) derived by MPIC from
961 spectra of the MPIC instrument

962 Like for the simulation results, in general, larger uncertainties are found for the O₄ dAMFs
963 compared to the O₄ AMFs. This is expected because the uncertainties of the O₄ dAMFs
964 contain the uncertainties of two analyses (at 90° elevation and at low elevation). Also, the
965 uncertainties on 18 June are again larger than on 8 July. This finding was not expected, but is
966 possibly related to the higher trace gas abundances (see Fig. 1 and Table A3 in appendix A1)
967 and the higher aerosol extinction close to the surface on 18 June.

968 Another interesting finding is that the uncertainties of the spectral analysis of O₄ are
969 dominated by the effect of instrumental properties up to ±12% in the morning of 18 June.
970 Further important uncertainties are associated with the choice of the wavelength range, the
971 degree of the polynomial and the intensity offset. In contrast, the exact choices of the trace
972 gas cross sections (including their wavelength- and temperature dependencies) play only a
973 minor role (up to a few percent). Excellent agreement (within ±1%) is in particular found for
974 the O₄ analysis of the synthetic spectra using the standard settings and the directly simulated
975 O₄ (d)AMFs at 360 nm. This indicates that the O₄ (d)AMFs retrieved in the wavelength range
976 352 – 387 nm are indeed representative for radiative transfer simulations at 360 nm.

977 As for the uncertainties of the simulated O₄ (d)AMFs, the uncertainties of the spectral
978 analysis are also split into a systematic and a random term: the systematic deviations of the O₄
979 dAMFs from those of the standard settings are about +1% and -1.5% for 18 June and 8 July,
980 respectively. The range of uncertainty is calculated from the uncertainty ranges of the
981 different error sources by assuming that they are all independent. The uncertainty ranges for
982 18 June and 8 July are calculated as ±12.5% and ±10.8%, respectively.

984 **4.4 Recommendations derived from the sensitivity studies**

985
986 In this section a short summary of the most important findings from the sensitivity studies is
987 given.

988 **Temperature and pressure profiles**

989 Temperature and pressure profiles from sondes or model data should be used if available.
990 Alternatively, of temperature and pressure profiles extrapolated from surface measurements
991 could be used. Typical uncertainties of the O₄ VCD derived from such profiles are still < 2%.
992 For high temperature (>20°C) the atmospheric humidity should be considered. If no
993 measurements are available, prescribed profiles, e.g. from the US standard atmosphere can be
994 used. However, depending on location and season the errors of the resulting O₄ VCD can be
995 rather large (see also Ortega et al., 2016).

996 **Integration of the O₄ VCD**

997
998 The integration should be performed on a vertical grid with at least 100 m resolution up to an
999 altitude of 30 km. The surface altitude should be taken into account with an accuracy of at
1000 least 20 m.

1001 **Measurements and spectral analysis**

1002
1003 Instruments should have a small FOV (≤1°), an accurate elevation calibration (better than
1004 0.5°), and a small and preferably well characterised stray light level. For the data analysis the
1005 standard settings as provided in Table 7 should be used. From the analysis of synthetic spectra
1006 it was found that the results for these settings are consistent with simulated O₄ (d)AMFs
1007 within 1 %.

1009
1010 **Information on aerosols**

1011 Aerosol profiles should be obtained from LIDARs or ceilometers using similar wavelengths
1012 as the MAX-DOAS measurements. Preferred LIDAR types are HSRL or Raman LIDARs,
1013 which directly provide profiles of aerosol extinction and thus need no assumptions on the
1014 LIDAR ratio. They should also have high signal to noise ratios and shallow blind region at the
1015 surface in order to cover a large altitude range. Information on aerosol optical properties and
1016 size distributions from sun photometers or in situ measurements should be used.

1017
1018 **RTM simulations**

1019 Radiative transfer models should use Mie phase functions e.g. derived from sun photometer
1020 observations. The consideration of polarisation and rotational Raman scattering is not
1021 necessary.

1022 If such optimised settings are used, the errors of the radiative transfer simulations and spectral
1023 analysis can be largely reduced: the uncertainties of the O₄ dAMFs related to radiative
1024 transfer simulations can be reduced from about $\pm 8\%$ as in this study to about $\pm 4\%$; those
1025 related to the spectral analysis can be reduced from about $\pm 10\%$ to about $\pm 6\%$.

1026
1027
1028 **4.4.1 Preferred scenarios for future studies**

1029 In addition to the recommendations given above, future campaigns should aim to cover
1030 different meteorological conditions (e.g. low temperatures), viewing geometries (e.g. low
1031 SZA), surface albedos (e.g. snow and ice) and wavelengths (e.g. 477, 577, and 630 nm). Also
1032 different aerosol scenarios including those with low aerosol optical depths should be covered.
1033 Max-DOAS measurements should be performed by at least 2, preferably more instruments.
1034 In order to minimise the effects of instrumental properties, the instruments should be well
1035 calibrated and should have low straylight levels. Based on the above criteria, measurements
1036 during the CINDI-2 campaign are probably well suited for a similar study.

1037
1038
1039 **5 Comparison of measurements and simulations**

1040
1041 The comparison results for both days are different: On 18 June (except in the evening)
1042 measurements and simulations agree within errors (the ratio of simulated and measured O₄
1043 dAMFs for the middle period of that day is 1.01 ± 0.16). In contrast, on 8 July measurements
1044 and simulations significantly disagree: Taking into account the errors of the VCD calculation
1045 (3%), the radiative transfer simulations ($+16 \pm 6.4\%$) and the spectral analysis ($-1.5 \pm 10.8\%$) for
1046 the middle period of that day results in a ratio of simulated and measured O₄ dAMFs of 0.81
1047 ± 0.10 , which differs significantly from unity.

1048
1049
1050
1051 **5.1 Important differences between both days**

1052
1053 On both selected days similar aerosol AOD were measured. Also the diurnal variation of the
1054 SZA was similar because of the proximity to summer solstice. However, also many
1055 differences are found for the two days, which are discussed below.

1056
1057
1058 a) temperature, pressure, wind:

1059 On 18 June surface pressure was lower by about 13 hPa and surface temperature was higher
1060 by about 7K than on 8 July, respectively. These differences were explicitly taken into account
1061 in the calculation of the O₄ profiles / VCDs, the radiative transfer simulations and the
1062 interpretation of the spectral analyses. Thus they can very probably not explain the different
1063 comparison results on the two days.

1064 On both days, wind was mainly blowing from East-North-East, but on 18 June it was blowing
1065 from West before about 08:00 and after 20:00 UTC. Wind speeds were lower on 18 June
1066 (between 1 and 2 m/s) than on 8 July (between 1 and 3 m/s).

1067
1068 b) aerosol properties:

1069 The in situ aerosol measurements show very different abundances and properties of aerosols
1070 close to the ground for the selected days. On 18 June much larger concentrations of larger
1071 aerosol particles are found, which cannot be measured by the ceilometer, because the lowest
1072 detecting altitude is 180m. Thus it can be concluded that the enhanced aerosol concentration
1073 on 18 June is confined to a shallow layer at the surface. In general the aerosol concentrations
1074 close to the surface are more variable on 18 June than on 8 July. The high aerosol
1075 concentrations close to the surface probably also affect the LIDAR ratio, which is thus
1076 probably more variable on 18 June. Similarly, also the phase function derived from the sun
1077 photometer (for the integrated aerosol profile) is probably less representative for the low
1078 elevation angles on 18 June because different aerosol size distributions probably existed at
1079 different altitudes. Finally, the Ångström parameter derived from AERONET observations is
1080 different for both days, especially for large wavelengths, which is in qualitative agreement
1081 with the higher in situ aerosol concentrations of large particles on 18 June. Also a larger
1082 forward peak of the derived aerosol phase function is found for 18 June. Both effects probably
1083 cause larger uncertainties on 18 June.

1084
1085 c) spectral analysis

1086 Larger uncertainties of the spectral analysis are found for 18 June compared to 8 July. This
1087 finding was surprising, but was also partly reproduced by the analysis of the synthetic spectra.
1088 One possible explanation is the smaller wavelength dependence of aerosol scattering at low
1089 altitudes on 18 June, which mainly affects measurements at low elevation angles. When
1090 analysed versus a zenith reference, for which the broad band wavelength dependency is much
1091 stronger (because of the larger contribution from Rayleigh scattering), larger deviations can
1092 be expected (e.g. because of differences of instrumental straylight, or the different detector
1093 saturation levels). On 18 June also higher (about doubled) NO₂ and HCHO concentrations are
1094 present compared to 8 July possibly leading to increased spectral interferences with the O₄
1095 absorption, but this effect is expected to be small.

1096
1097
1098 **5.2 Which conditions would be needed to bring measurements and simulations on 8 July**
1099 **into agreement**

1100
1101 This section describes possible (but unrealistic) changes of the atmospheric scenario, the
1102 instrument properties or the input parameters, which could bring measurements and
1103 simulations on 08 July into agreement. If e.g. the whole aerosol extinction profile was scaled
1104 by 0.65, the corresponding O₄ dAMFs would almost perfectly match the measured ones.

1105 Similarly good agreement could also be achieved if the about 27% of the total AOD would be
1106 shifted from low layers (below 1.68 km) to high layers (above 4.9 km, see appendix A6).
1107 However, in this scenario, about 73% of the total aerosol extinction would be above 1.68 km.
1108 Such a scenario would also not be in agreement with the AERONET inversion products and

1109 would also lead to an underestimation of the diurnal variation of the O₄ AMFs measured in
1110 zenith direction.

1111 Also horizontal gradients of the aerosol extinction could in principle explain the discrepancy.
1112 While we are not able to quantify them, they surely would have to be of the order of several
1113 ten percent per 10 km. Such persistent horizontal gradients are not supported by the almost
1114 constant AOD during the day. Also the finding that mismatch between measurements and
1115 simulations is found for all azimuth angles indicates that horizontal gradients can not explain
1116 the observed discrepancies.

1117 Another possibility would be aerosol phase functions with very high asymmetry parameters
1118 (>> 0.75). Also systematic errors of the O₄ cross section could explain the observed
1119 discrepancies. Finally, an overcorrection of spectrograph straylight (or any other intensity
1120 offset) could be explain the discrepancies. However, a rather high overcorrection (by about
1121 20%) would be needed, which is probably unrealistic.

1125 **5-6 Discussion and eConclusions**

1127 We compared MAX-DOAS observations of the atmospheric O₄ absorption with
1128 corresponding radiative transfer simulations for two mainly cloud-free days during the MAD-
1129 CAT campaign. A large part of this study is dedicated to the extraction of input information
1130 for the radiative transfer simulations and the quantification of the associated errors of the
1131 radiative transfer simulations and spectral retrievals. One important result was from the
1132 sensitivity studies is that the O₄ results derived from the analysis of synthetic spectra using the
1133 standard settings are consistent with the simulated O₄ air mass factors within 1%. Also
1134 recommendations for the settings of the radiative transfer simulations, in particular on the
1135 extraction of aerosol and O₄ profiles are given. One important result is that the quality of the
1136 aerosol data sets is crucial to constrain the radiative transfer simulations. For example, it is
1137 recommended that LIDAR instruments are operated at wavelengths close to those of the
1138 MAX-DOAS measurementst and have a small sensitivity gap close to the surface. Further
1139 aerosol properties (e.g. size distributions, phase functions) should be available from sun
1140 photometer and/or in situ measurements. If such aerosol data are available the corresponding
1141 uncertainties of the radiative transfer simulations could be largely reduced to about $\pm 5\%$.
1142 Similar uncertainties can also be expected for optimum instrument operations and data
1143 analyses.

1144 The comparison results for both days are different: On 18 June (except in the evening)
1145 measurements and simulations agree within errors (the a ratio of simulated and measured O₄
1146 dAMFs for the middle period of that day is 1.01 ± 0.16). In contrast, on 8 July measurements
1147 and simulations significantly disagree: Taking into account the errors of the VCD calculation
1148 (3%), the radiative transfer simulations ($+16 \pm 6.44\%$) and the spectral analysis ($-1.5 \pm 10.8\%$)
1149 for the middle period of that day results in a ratio of simulated and measured O₄ dAMFs of
1150 0.71 ± 0.42 , which differs significantly from unity. No plausible explanation for the
1151 observed discrepancies on 8 July was found.

1152 ~~On 18 June larger uncertainties both for the measurements and radiative transfer simulations~~
1153 ~~exist, mainly related to the high aerosol concentration close to the surface. A summary of the~~
1154 ~~most important differences between both days is given in section 5.1.~~

1155 A large part of this study was dedicated to the extraction of input information for the radiative
1156 transfer simulations and to the quantification of the errors of the radiative transfer simulations
1157 and spectral retrievals. In particular, the analysis of synthetic spectra indicated that the O₄
1158 results derived from the spectral analysis using the standard settings are consistent with the
1159 simulated O₄ air mass factors within 1%.

1160 Based on this study, also recommendations for similar future studies are derived (see section
1161 5.2). In general, the largest errors sources arise from spectral analyses (partly related to
1162 imperfections of the MAX DOAS instruments) and the uncertainties of the aerosol phase
1163 functions and extinction profiles. Even if the aerosol extinction profiles could be better
1164 constraint, e.g. using results from Raman LIDARs or high spectral resolution LIDARs
1165 (HSRL), the uncertainties of the aerosol phase function will remain a critical error source.
1166 Future measurements should in particular try to minimize these error sources. Here it should
1167 be noted that the general larger errors obtained for 18 June are probably not representative for
1168 typical measurement conditions. For example, during the CINDI 2 campaign
1169 (<http://www.tropomi.eu/data-products/cindi-2>) the deviations of the O₄ spectral analysis
1170 results were much smaller than those for 18 June.

1171 The main conclusion from this study is that on one of the two selected days during the
1172 MADCAT campaign (08 July) a scaling factor (of about 0.71±0.12) is needed to bring
1173 measurements and forward model into agreement. As long as the reason for this deviation is
1174 not understood, it is, however, unclear, how representative these findings are for other
1175 measurements (e.g. from other platforms, at other locations/seasons, for other aerosol loads,
1176 and other wavelengths). Thus further studies spanning a large variety of measurement
1177 conditions and also including other wavelengths are recommended.

1178

1179

1180 **5.1 Important differences between both days**

1181

1182 On both selected days similar aerosol AOD were measured. Also the diurnal variation of the
1183 SZA was similar because of the proximity to summer solstice. However, also many
1184 differences are found for the two days, which are discussed below.

1185

1186 a) temperature, pressure, wind:

1187 On 18 June surface pressure was lower by about 13 hPa and surface temperature was higher
1188 by about 7K than on 8 June, respectively. These differences were explicitly taken into account
1189 in the calculation of the O₄ profiles / VCDs, the radiative transfer simulations and the
1190 interpretation of the spectral analyses. Thus they can very probably not explain the different
1191 comparison results on the two days.

1192 On both days, wind was mainly blowing from East North East, but on 18 June it was blowing
1193 from West before about 08:00 and after 20:00 UTC. Wind speeds were lower on 18 June
1194 (between 1 and 2 m/s) than on 8 July (between 1 and 3 m/s).

1195

1196 b) aerosol properties:

1197 The in situ aerosol measurements show very different abundances and properties of aerosols
1198 close to the ground for the selected days. On 18 June much larger concentrations of larger
1199 aerosol particles are found, which cannot be measured by the ceilometer, because the lowest
1200 detecting altitude is 180m. Thus it can be concluded that the enhanced aerosol concentration
1201 on 18 June is confined to a shallow layer at the surface. In general the aerosol concentrations
1202 close to the surface are more variable on 18 June than on 8 July. The high aerosol
1203 concentrations close to the surface probably also affect the LIDAR ratio, which is thus more
1204 variable on 18 June. Since a constant LIDAR ratio is used for the extraction of the aerosol
1205 extinction profiles, also the uncertainties of the aerosol profile are probably larger on 18 June.
1206 Similarly, also the phase function derived from the sun photometer (for the integrated aerosol
1207 profile) is probably less representative for the low elevation angles on 18 June because
1208 different aerosol size distributions probably existed at different altitudes. Finally, the
1209 Ångström parameter derived from AERONET observations is different for both days,
1210 especially for large wavelengths, which is in qualitative agreement with the higher in situ

1211 aerosol concentrations of large particles on 18 June. Also a larger forward peak of the derived
1212 aerosol phase function is found for 18 June. Both effects probably cause larger uncertainties
1213 on 18 June.

1214

1215 c) spectral analysis

1216 Larger uncertainties of the spectral analysis are found for 18 June compared to 8 July. This
1217 finding was surprising, but was also partly reproduced by the analysis of the synthetic spectra.
1218 One possible explanation is the smaller wavelength dependence of aerosol scattering at low
1219 altitudes on 18 June, which mainly affects measurements at low elevation angles. When
1220 analysed versus a zenith reference, for which the broad band wavelength dependency is much
1221 stronger (because of the larger contribution from Rayleigh scattering), larger deviations can
1222 be expected (e.g. because of differences of instrumental straylight, or the different detector
1223 saturation levels). On 18 June also higher (about doubled) NO₂ and HCHO concentrations are
1224 present compared to 8 July possibly leading to increased spectral interferences with the O₄
1225 absorption, but this effect is expected to be small.

1226

1227

1228 **5.2 Recommendations**

1229

1230 Based on the findings of this comparison study, recommendations for similar future studies
1231 are derived. Part of them are also of interest for the interpretation of O₄ measurements in
1232 general.

1233

1234 a) VCD calculation

1235 Temperature and pressure profiles representative for individual days should be used. If such
1236 profiles are not available, also profiles extrapolated from surface measurements can be used.
1237 They are not 'perfect' but usually the associated errors are at the percent level. The vertical
1238 grid for the integration of the O₄ profile should not be coarser than 100m. The integration
1239 should be carried out up to an altitude of at least 30 km. The exact height of the instrument
1240 position needs to be taken into account.

1241

1242 b) Radiative transfer simulations

1243 If available appropriate phase functions (e.g. from Mie calculations) should be used. Here it is
1244 important to note that even if appropriate asymmetry parameters are available, the often used
1245 HG parameterisation becomes very imprecise for forward scattering geometries.

1246

1247 c) Spectral analysis

1248 The spectral range should cover the two O₄ bands at 360 and 380 nm. An intensity offset
1249 should be included in the analysis. If the surface temperature differs strongly (more than 25K)
1250 from 300K the effect of the temperature dependence of the O₄ absorption should be
1251 considered.

1252

1253 d) Preferred scenarios for future studies

1254 In particular the uncertainties related to aerosols should be minimised. For example,
1255 measurements at rather low AOD (<0.1) and with low temporal variability should be selected.
1256 Aerosol profiles should be derived from LIDARs/ceilometers which are sensitive down to very
1257 shallow altitudes (low overlap ranges). If possible, Raman LIDARs or high spectral-
1258 resolution LIDARs (HSRL) should be used, because from such observations the aerosol
1259 extinction profile can be derived without the assumption of a LIDAR ratio. Also sun
1260 photometer measurements should be available. Besides AOD and the Ångström parameter

1261 ~~also information on the phase function and single scattering albedo from these measurements
1262 should be used.~~

1263 ~~It would be interesting to cover other meteorological conditions (e.g. low temperatures),
1264 viewing geometries (e.g. low SZA), surface albedos (e.g. snow and ice) and wavelengths (e.g.
1265 477, 577, and 630 nm).~~

1266 ~~In order to minimise the effects of instrumental properties, the instruments should be well
1267 calibrated and should have low straylight levels. At least two instruments should be operated
1268 at the same site. Based on the above criteria, measurements during the CINDI 2 campaign are
1269 probably well suited for a similar study.~~

1270 1271 **Acknowledgments**

1272 We are thankful for several external data sets which were used in this study: Temperature and
1273 pressure profiles from the ERAInterim reanalysis data set were provided by the European
1274 Centre for Medium-Range Weather Forecasts. In situ measurements of trace gas and aerosol
1275 concentrations as well as meteorological data were performed by the environmental
1276 monitoring services of the States of Rhineland-Palatinate and Hesse (<http://www.luft-rlp.de>
1277 and <https://www.hlnug.de/themen/luft/luftmessnetz.html>). We thank M. O. Andreae and
1278 Günther Schebeske for operating the Ceilometer and the AERONET instrument at the Max
1279 Planck Institute for Chemistry.

1280 1281 **Tables**

1282
1283
1284
1285
1286
1287
1288
1289
1290
1291
1292
1293
1294
1295
1296
1297
1298
1299
1300
1301
1302
1303
1304
1305
1306 Table 1 Overview on studies which did not apply a scaling factor (upper part) or did apply a
1307 scaling factor (lower part) to the measured O₄ dSCDs. Besides the initial studies proposing a
1308 scaling factor (Wagner et al., 2009; Clémer et al., 2010) only studies after 2010 are listed.

Reference	Measurement type	Location and period	O ₄ band (nm)	Scaling factor
Studies which did not apply a scaling factor*				

Thalmann and Volkamer, 2010	CE-DOAS	Laboratory	477	1
Peters et al., 2012a	MAX-DOAS	Western Pacific Ocean (Oct 2009)	360, 477	1
Spinei et al. 2015	Direct sun DOAS	JPL, USA (Jul 2007) Pullman, USA (Sep – Nov 2007, Jul – Nov 2011) Fairbanks, USA (Mar-Apr 2011) Huntsville, USA (Aug 2008) Richland, USA (Apr-Jun 2008) Greenbelt, USA (May 2007, 2012-2014) Cabauw, The Netherlands (Jun-Jul 2009)	360, 477	1
Spinei et al., 2015 / Volkamer et al., 2015	Airborne DOAS	Subtropical Pacific Ocean (Jan 2012)	360, 477	1
Ortega et al., 2016	MAX-DOAS	Cape Cod, USA (Jul 2012)	360, 477	1
Schreier et al., 2016	MAX-DOAS	Zugspitze, Germany (Apr-Jul 2003) Pico Espejo, Venezuela (2004 - 2009)	360	1
Seyler et al., 2017	MAX-DOAS	German Bight (2013-2016)	360, 477	1
Wang et al., 2017a,b	MAX-DOAS	Wuxi, China (2011 - 2014)	360	1
Gielen et al., 2017	MAX-DOAS	Bujumbura, Burundi (2013-2015)	360, 477	1
Franco et al., 2015	MAX-DOAS	Jungfraujoch (2010 –2012)	360	1

Studies which did apply a scaling factor

Wagner et al., 2009	MAX-DOAS	Milano, Italy Sep 2013 (FORMAT II)	360	0.81
Clemer et al., 2010	MAX-DOAS	Beijing, China Jul 2008 – Apr 2009	360, 477, 577, 630	0.80
Irie et al., 2011	MAX-DOAS	Cabauw, The Netherlands Jul-Jun 2009 (CINDI-I)	360, 477	0.75±0.1
Merlaud et al., 2011	Airborne DOAS	Arctic Apr 2008 POLARCAT)	360	0.89
Vlemmix et al., 2011	MAX-DOAS	Cabauw, The Netherlands Jul-Oct 2009 (CINDI-I)	477	0.8
Zieger et al., 2011	Overview on MAX-DOAS	Cabauw, The Netherlands Jul-Oct 2009 (CINDI-I)	360 (MPIC) 477 (BIRA) 477 (IUPHD) 477 (JAMSTEC)	0.83 0.75 0.8 0.8*
Wang et al., 2014	MAX-DOAS	Xianghe, China (2010 - 2013)	360	0.8
Kanaya et al., 2014	MAX-DOAS	Cape Hedo, Japan (2007 – 2012) Fukue, Japan (2008 – 2012) Yokosuda, Japan (2007 – 2012) Gwangju, Korea (2008 – 2012) Hefei, China (2008 – 2012) Zvenigorod; Russia (2009 – 2012)	477 477 477 477 477 477	0.8 0.8 0.8 0.8 0.8 0.8
Hendrick et al., 2014	MAX-DOAS	Beijing, China (2008 - 2009) Xianghe, China (2010 – 2012)	360	0.8
Vlemmix et al., 2015	MAX-DOAS	Beijing, China (2008 - 2009) Xianghe, China (2010 – 2012)	360, 477	0.8
Irie et al.,	MAX-DOAS	Tsukuba, Japan (Oct 2010)	477	elevation

2015				dependent scaling factor**
Wang et al., 2016	MAX-DOAS	Madrid, Spain (Mar – Sep 2015)	360	0.83
Friess et al., 2016	MAX-DOAS	Cabauw, The Netherlands Jul-Jul 2009 (CINDI-I)	477 (AOIFM) 477 (BIRA) 477 (IUPHD) 477 (JAMSTEC) 360 (MPIC)	0.8 0.8 1 0.8*** 0.77

1309 *The authors of part of these studies were probably not aware that a scaling factor was applied by other groups.

1310 **SF = 1 / (1 + EA/60)

1311 ***SF is varied during profile inversion

1312 1313 1314 Table 2 Periods on both selected days, which are used for the comparisons.

day	1 st period	2 nd period	3 rd period
18 June 2013	8:00 – 11:00 UTC	11:00 – 14:00 UTC	14:00 – 19:00 UTC
8 July 2013	4:00 – 7:00 UTC	7:00 – 11:00 UTC	11:00 – 19:00 UTC

1315 1316 1317 1318 Table 3 Participation of the different groups in the different analysis steps

Abreviation	Institution	Determination of the O ₄ profile and VCD	Extraction of aerosol profiles	Radiative transfer simulations	Spectral analysis
BIRA	BIRA/IASB, Brussels, Belgium				•
CMA	Meteorological Observation Center, Beijing, China			•	•
CSIC	Department of Atmospheric Chemistry and Climate, Institute of Physical Chemistry Rocasolano (CSIC), Spain.	•			•
INTA	Instituto Nacional de Técnica Aeroespacial, Spain	•	•	•	•
IUP-B	University of Bremen, Germany		•	•	•
IUP-HD	University of Heidelberg, Germany				•
LMU	Ludwig-Maximilians-Universität München, Germany	•	•		
MPIC	MPG for chemistry, Mainz, Germany	•	•	•	•

1319 1320 1321 1322 Table 4 Overview on properties of MAX-DOAS instruments participating in this study

Institute / Instrument	Spectral range	Spectral resolution	Spectral range per	Detector type / temperature	Integration time of	Reference
------------------------	----------------	---------------------	--------------------	-----------------------------	---------------------	-----------

type	(nm)	(FWHM, nm)	detector pixel (nm)		individual spectra (s)	
BIRA / 2-D scanning MAX-DOAS	300 - 386	0.49	0.04	2-D back-illuminated CCD, 2048 x 512 pixels / -40 °C	60	Clémer et al., 2010
IUP-Bremen / 2-D scanning MAX-DOAS	308 - 376	0.43	0.05	2-D back-illuminated CCD, 1340 x 400 pixels / -35 °C	20	Peters et al., 2012b
IUP-Heidelberg / 1-D scanning MAX-DOAS	294 - 459	0.59	0.09	AvaSpec-ULS 2048 pixels back-thinned Hamamatsu CCD S11071-1106 / 20°C	60	Lampel et al., 2015
MPIC / 4-azimuth MAX-DOAS	320 – 457	0.67	0.14	2-D back-illuminated CCD, 1024 x 255 Pixels / -30°C	10 s	Krautwurst, 2010

1323

1324

1325

1326

1327

1328

1329

1330

1331

1332

1333

1334

1335

1336

1337

1338

1339

1340

1341

1342

1343

1344

1345

1346

1347

1348

1349

1350

Table 5 Independent data sets used to constrain the atmospheric properties during both selected days.

Measurement / data set	Measured quantities	Derived quantities	Temporal / spatial resolution	Source / reference
-------------------------------	----------------------------	---------------------------	--------------------------------------	---------------------------

Ceilometer	Attenuated backscatter profiles* at 1064 nm	Aerosol extinction profiles at 360 nm	30s** / 15 m	Wiegner and Geiß, 2012
AERONET sun photometer	Solar irradiances, Sky radiances	Aerosol optical depth, single scattering albedo, phase function	Typical integration time: 2 to 15 min	Holben et al., 2001, https://aeronet.gsfc.nasa.gov/
Surface measurements air quality stations in Mainz Mombach	temperature, pressure, rel. humidity		1h	http://www.luft-rlp.de
Surface measurements air quality stations in Mainz and Wiesbaden	pm _{2.5} pm ₁₀		1h (Mainz stations) 30 min (Wiesbaden stations)***	http://www.luft-rlp.de https://www.hlnug.de/themen/luft/luftmessnetz.html
ECMWF ERA-Interim reanalysis	temperature, Pressure, rel. humidity		Average over the area 49.41°-50.53° N, 7.88°-9.00° E, every 6 h	(Dee et al., 2011)

1351 *no useful signal below 180m due to limited overlap

1352 **Here 15 min averages are used.

1353 ***Stations in Mainz: Parcusstrasse, Zitadelle, Mombach; Stations in Wiesbaden: Schierstein, Ringkirche, Süd

1359 Table 6 Standard settings for the radiative transfer simulations

Parameter	Standard setting
Temperature and pressure profile	MPIC extraction
O ₃ profile	MPIC extraction
Surface albedo	5 %
Aerosol single scattering albedo	0.95
Aerosol phase function	HG model with asymmetry parameter of 0.68
Aerosol extinction profile	MPIC extraction with linear interpolation < 180 m
Polarisation	Not considered
Raman scattering	Partly considered for synthetic spectra

1360
1361
1362
1363 Table 7 Standard settings for the DOAS analysis of O₃.

Parameter	Value, Remark / Reference
Spectral range	352 – 387 nm
Degree of DOAS polynomial	5

Degree of intensity offset polynomial	2
Fraunhofer reference spectrum	08 July, 10:05:35, SZA: 32.37°, elevation angle: 90° (this spectrum is used for both days)
Wavelength calibration	Fit to high resolution solar spectrum using Gaussian slit function
Shift / squeeze	The measured spectrum is shifted and squeezed against all other spectra
Ring spectrum 1	Normal Ring spectrum calculated from DOASIS
Ring spectrum 2	Ring spectrum 1 multiplied by λ^{-4}
O ₃ cross section	223 K, Bogumil et al. (2003)
NO ₂ cross section	294 K, Vanaege et al. (1997)
BrO cross section	223 K, Fleischmann et al. (2004)
O ₄ cross section	293 K, Thalman and Volkamer (2013)

1364

1365

1366

1367

Table 8 Average ratios (simulation results divided by measurements) of the O₄ (d)AMFs for both middle periods of the selected days.

Period	18.06.2013, 11:00 – 14:00	08.07.2013, 7:00 – 11:00
AMF ratio	0.97	0.83
DAMF ratio	0.94	0.69

1368

1369

1370

1371

1372

1373

1374

1375

Table 9 Summary of uncertainties of the simulated O₄ (d)AMFs for the middle periods of both selected days. The two numbers left and right of the '/' indicate the minimum and maximum deviations. The columns with label 'Optimum' indicate the uncertainties which could be reached if optimum information on the measurement conditions was available (e.g. height profiles of temperature, pressure and aerosol extinction as well as well aerosol microphysical or optical properties).

	O ₄ AMF			O ₄ dAMF		
	18 June	8 July	Optimum settings	18 June	8 July	Optimum settings
Effects of RTM						
Radiative transfer model	-1% / +2%	0% / +1%	<u>±1%</u>	-1% / +5%	0% / +3%	<u>±1%</u>
Polarisation	0% / 0%	0% / 0%	<u>0%</u>	0% / 0%	0% / +1%	<u>0%</u>
Effects of input parameters						
O ₄ profile extraction	0% / + 2%	0% / + 1%	<u>±1%</u>	0% / + 4%	0% / + 2%	<u>±1%</u>
Single scattering albedo	-1% / + 3%	-1% / + 1%	<u>0%</u>	-1% / + 3%	-1% / + 1%	<u>0%</u>
Phase function	-3% / +3%	-2% / 0%	<u>±1%</u>	-5% / +9%	-5% / +2%	<u>±1.5%</u>
Aerosol profile extraction	-1% / + 1%*	-2% / + 2%	<u>±1%</u>	-2% / + 1%*	-4% / + 4%	<u>±1.5%</u>
Extrapolation below 180 m	0% / + 2%	-1% / + 1%	<u>0%</u>	-1% / + 4%	-2% / + 2%	<u>0%</u>
LIDAR ratio &	<u>?</u>	<u>+5% /</u>	<u>±2%**</u>	<u>?</u>	<u>+13% /</u>	<u>±3%**</u>

<u>wrong wavelength</u>		<u>+6%</u>			<u>+17%</u>	
Surface albedo	0% / + 2%	0% / + 1%	<u>0%</u>	0% / + 2%	-1% / + 0%	<u>0%</u>
Total uncertainty						
Average deviation (from results for standard settings)	+4.5%	+ <u>0.56</u> %		+8.5%	<u>±16</u> %	
Range of uncertainty	<u>±4.4%*</u>	<u>±2.8%</u>	<u>±2.8%**</u>	<u>±8.7%*</u>	<u>±6.14%</u>	<u>±3.8%**</u>

1376 *this uncertainty does not contain the contribution from variation of aerosol properties with
 1377 altitude, see text

1378 **if LIDAR profiles at the same wavelength and without gaps in the troposphere were
 1379 available.

1380

1381 Table 10 Summary of uncertainties of the measured O₄ (d)AMFs for the middle periods of
 1382 both selected days. The two numbers left and right of the '/' indicate the minimum and
 1383 maximum deviations. The columns with label 'Optimum' indicate the uncertainties which
 1384 could be reached if optimum instrumental performance was ensured and optimum cross
 1385 section were available.

	O ₄ AMF			O ₄ dAMF		
	18 June	8 July	Optimum	18 June	8 July	Optimum
Consistency spectral analysis versus RTM						
Analysis of synthetic spectra	-1% / +1%	-1% / 0%	<u>±1%</u>	0% / 0%	0% / +1%	<u>±1%</u>
Fit settings						
Spectral range	-7% / -3%	-3% / 0%	<u>±1%</u>	-12% / -1%	-6% / -1%	<u>±1%</u>
Degree of polynomial	+0% / +4%	0% / +3%	<u>±1%</u>	0% / +6%	0% / +6%	<u>±1%</u>
Intensity offset*	+1% / +5%	+1% / +3%	<u>±1%</u>	+3% / +11%	+2% / +4%	<u>±1.5%</u>
Ring	+1% / +2%	-1% / +1%	<u>±1%</u>	+1% / +1%	-1% / +1%	<u>±1.5%</u>
Temperature dependence of NO ₂ absorption	0% / 0%	0% / 0%	<u>0%</u>	0% / 0%	0% / 0%	<u>0% / 0%</u>
Wavelength dependence of NO ₂ absorption	-1% / 0%	0% / 0%	<u>0%</u>	-2% / -1%	-1% / 0%	<u>0%</u>
Wavelength dependence of O ₄ absorption	-1% / 0%	-1% / -1%	<u>0%</u>	0% / +1%	-1% / -1%	<u>0%</u>
Including H ₂ O cross section	0% / 0%	0% / 0%	<u>0%</u>	+1% / +1%	+1% / +1%	<u>0%</u>
Including HCHO cross section	-3% / 0%	-1% / 0%	<u>0%</u>	-6% / -4%	-3% / -2%	<u>0%</u>

Different O ₄ cross sections*	-2% / +1%	-2% / +1%	<u>±2%</u>		-3% / +3%	-3% / +3%	<u>±2%</u>
Temperature dependence of the O₄ absorption							
Analysis using two O ₄ cross sections for different temperatures [▼]	0% / 0%	+2% / +2%	<u>±1%</u>		+4% / +4%	+1% / +1%	<u>±1.5%</u>
Analysis of synthetic spectra for different surface temperatures	-1% / 0%	-1% / +2%			+4% / +4%	+1% / +1%	
Analysis from different instruments and groups							
Different groups and analyses [◆]	-6% / + 5%	-6% / + 5%	<u>±3%[▲]</u>		-12% / +7%	-12% / +7%	<u>±4.5%</u>
Total uncertainty							
Average deviation (from results for standard settings)	-4.5%	-0.5%			+1%	-1.5%	
Range of uncertainty	±7.0%	±6.5%	<u>±4.2%</u>		±12.5%	±10.8%	<u>±5.7%</u>

1386 *here the case ‘no offset’ is not considered

1387 *here the case of the non-shifted Greenblatt O₄ cross section is not considered

1388 [▼]here only the results for the measured spectra in the spectral range 352 – 387 nm are
1389 considered. (temperatures on 18 June: 27–31 °C; 8 July: 20–30 °C)

1390 [◆]The results for 18 June are also taken for 8 July due to the lack of measurements on 8 July

1391 [▲]see Kreher et al., 2019

1394 References

1395
1396 Acarreta, J. R., De Haan, J. F., and Stammes, P.: Cloud pressure retrieval using the O₂-O₂
1397 absorption band at 477 nm, J. Geophys. Res., 109, D05204, doi:10.1029/2003JD003915,
1398 2004.

1399
1400 Bogumil, K., J. Orphal, T. Homann, S. Voigt, P. Spietz, O.C. Fleischmann, A. Vogel, M.
1401 Hartmann, H. Bovensmann, J. Frerik and J.P. Burrows, Measurements of Molecular
1402 Absorption Spectra with the SCIAMACHY Pre-Flight Model: Instrument Characterization

1403 and Reference Data for Atmospheric Remote-Sensing in the 230-2380 nm Region, *J.*
1404 *Photochem. Photobiol. A.*, 157, 167-184, 2003.

1405

1406 Chance, K.V., and R.L. Kurucz, An improved high-resolution solar reference spectrum for
1407 earth's atmosphere measurements in the ultraviolet, visible, and near infrared, J. Quant.
1408 Spectrosc. Radiat. Transfer, 111, 1289-1295, 2010.

1409

1410 Chandrasekhar S. Radiative Transfer. New York: Dover Publications Inc.; 1960.

1411

1412 Chandrasekhar S. Selected papers, vol. 2. New York: University of Chicago Press, 1989.

1413

1414 Clément, K., Van Roozendael, M., Fayt, C., Hendrick, F., Hermans, C., Pinardi, G., Spurr, R.,
1415 Wang, P., and De Mazière, M.: Multiple wavelength retrieval of tropospheric aerosol optical
1416 properties from MAXDOAS measurements in Beijing, *Atmos. Meas. Tech.*, 3, 863-878,
1417 doi:10.5194/amt-3-863-2010, 2010.

1418

1419 Dee, D. P., Uppala, S. M., Simmons, A. J., Berrisford, P., Poli, P., Kobayashi, S., Andrae, U.,
1420 Balmaseda, M. A., Balsamo, G., Bauer, P., Bechtold, P., Beljaars, A. C. M., van de Berg, L.,
1421 Bidlot, J., Bormann, N., Delsol, C., Dragani, R., Fuentes, M., Geer, A. J., Haimberger, L.,
1422 Healy, S. B., Hersbach, H., H'olm, E. V., Isaksen, L., K'allberg, P., K'ohler, M., Matricardi,
1423 M., McNally, A. P., Monge-Sanz, B. M., Morcrette, J.-J., Park, B.-K., Peubey, C., de Rosnay,
1424 P., Tavolato, C., Th'epaut, J.-N., and Vitart, F.: The ERA-Interim reanalysis: configuration
1425 and performance of the data assimilation system, *Q. J. Roy. Meteorol. Soc.*, 137, 553-597,
1426 doi:10.1002/qj.828, 2011.

1427

1428 Deutschmann, T., Beirle, S., Frieß, U., Grzegorski, M., Kern, C., Kritten, L., Platt, U., Pukite,
1429 J., Wagner, T., Werner, B., and Pfeilsticker, K.: The Monte Carlo Atmospheric Radiative
1430 Transfer Model McArtim: Introduction and Validation of Jacobians and 3D Features, *J.*
1431 *Quant. Spectrosc. Ra.*, 112, 1119-1137, doi:10.1016/j.jqsrt.2010.12.009, 2011.

1432

1433 Dubovik, O., Holben, B. N., Eck, T. F., Smirnov, A., Kaufman, Y. J., King, M. D., Tanré, D.,
1434 and Slutsker, I.: Variability of absorption and optical properties of key aerosol types observed
1435 in worldwide locations, *J. Atmos. Sci.*, 59, 590-608, 2002.

1436

1437 Erle, F., K. Pfeilsticker, and U. Platt, On the influence of tropospheric clouds on zenith-
1438 scattered-light measurements of stratospheric species, *Geophys. Res. Lett.*, 22, 2725- 2728,
1439 1995.

1440

1441 Fleischmann, O. C., Hartmann, M., Burrows, J. P., and Orphal, J.: New ultraviolet absorption
1442 cross-sections of BrO at atmospheric temperatures measured by time-windowing Fourier
1443 transform spectroscopy, *J. Photoch. Photobiol. A*, 168, 117-132, 2004.

1444

1445 Franco, B., Hendrick, F., Van Roozendael, M., Müller, J.-F., Stavrakou, T., Marais, E. A.,
1446 Bovy, B., Bader, W., Fayt, C., Hermans, C., Lejeune, B., Pinardi, G., Servais, C., and Mahieu,
1447 E.: Retrievals of formaldehyde from ground-based FTIR and MAX-DOAS observations at the
1448 Jungfraujoch station and comparisons with GEOS Chem and IMAGES model simulations,
1449 *Atmos. Meas. Tech.*, 8, 1733-1756, <https://doi.org/10.5194/amt-8-1733-2015>, 2015.

1450

1451 Frieß, F., P. S. Monks, J. J. Remedios, A. Rozanov, R. Sinreich, T. Wagner, and U. Platt,
1452 MAX-DOAS O₄ measurements: A new technique to derive information on atmospheric

1453 aerosols. (II) Modelling studies, J. Geophys. Res., 111, D14203,
1454 doi:10.1029/2005JD006618.2006.

1455

1456 Frieß, U., Klein Baltink, H., Beirle, S., Clémer, K., Hendrick, F., Henzing, B., Irie, H., de
1457 Leeuw, G., Li, A., Moerman, M. M., van Roozendael, M., Shaiganfar, R., Wagner, T., Wang,
1458 Y., Xie, P., Yilmaz, S., and Zieger, P.: Intercomparison of aerosol extinction profiles retrieved
1459 from MAX-DOAS measurements, Atmos. Meas. Tech., 9, 3205-3222,
1460 <https://doi.org/10.5194/amt-9-3205-2016>, 2016.

1461

1462 Gielen, C., Hendrick, F., Pinardi, G., De Smedt, I., Fayt, C., Hermans, C., Stavrakou, T.,
1463 Bauwens, M., Müller, J.-F., Ndenzako, E., Nzohabonayo, P., Akimana, R., Niyonzima, S.,
1464 Van Roozendael, M., and De Mazière, M.: Characterisation of Central-African aerosol and
1465 trace-gas emissions based on MAX-DOAS measurements and model simulations over
1466 Bujumbura, Burundi, Atmos. Chem. Phys. Discuss., <https://doi.org/10.5194/acp-2016-1104>,
1467 in review, 2017.

1468

1469 Greenblatt G.D., Orlando, J.J., Burkholder, J.B., and Ravishankara, A.R.: Absorption
1470 measurements of oxygen between 330 and 1140 nm, J. Geophys. Res., 95, 18577-18582,
1471 1990.

1472

1473 Hendrick, F., Van Roozendael, M., Kylling, A., Petritoli, A., Rozanov, A., Sanghavi, S.,
1474 Schofield, R., von Friedeburg, C., Wagner, T., Wittrock, F., Fonteyn, D., and De Mazière, M.:
1475 Intercomparison exercise between different radiative transfer models used for the
1476 interpretation of ground-based zenith-sky and multi-axis DOAS observations, Atmos. Chem.
1477 Phys., 6, 93-108, doi:10.5194/acp-6-93-2006, 2006.

1478

1479 Hendrick, F., Müller, J.-F., Clémer, K., Wang, P., De Mazière, M., Fayt, C., Gielen, C.,
1480 Hermans, C., Ma, J. Z., Pinardi, G., Stavrakou, T., Vlemmix, T., and Van Roozendael, M.:
1481 Four years of ground-based MAX-DOAS observations of HONO and NO₂ in the Beijing area,
1482 Atmos. Chem. Phys., 14, 765-781, <https://doi.org/10.5194/acp-14-765-2014>, 2014.

1483

1484 Heue, K.-P., Riede, H., Walter, D., Brenninkmeijer, C. A. M., Wagner, T., Frieß, U., Platt, U.,
1485 Zahn, A., Stratmann, G., and Ziereis, H.: CARIBIC DOAS observations of nitrous acid and
1486 formaldehyde in a large convective cloud, Atmos. Chem. Phys., 14, 6621-6642,
1487 <https://doi.org/10.5194/acp-14-6621-2014>, 2014.

1488

1489 Hönninger, G., von Friedeburg, C., and Platt, U.: Multi Axis Differential Optical Absorption
1490 Spectroscopy (MAX-DOAS), Atmos. Chem. Phys., 4, 231–254, 2004.

1491

1492 Holben, B. N., Tanre, D., Smirnov, A., Eck, T. F., Slutsker, I., Abuhassan, N., Newcomb, W.
1493 W., Schafer, J., Chatenet, B., Lavenue, F., Kaufman, Y. J., Vande Castle, J., Setzer, A.,
1494 Markham, B., Clark, D., Frouin, R., Halthore, R., Karnieli, A., O'Neill, N. T., Pietras, C.,
1495 Pinker, R. T., Voss, K., and Zibordi, G.: An emerging ground-based aerosol climatology:
1496 Aerosol Optical Depth from AERONET, J. Geophys. Res., 106, 12067–12097, 2001.

1497

1498 Irie, H., Kanaya, Y., Akimoto, H., Iwabuchi, H., Shimizu, A., and Aoki, K.: First retrieval of
1499 tropospheric aerosol profiles using MAX-DOAS and comparison with lidar and sky
1500 radiometer measurements, Atmos. Chem. Phys., 8, 341–350, doi:10.5194/acp-8-341-2008,
1501 2008.

1502

1503 Irie, H., Takashima, H., Kanaya, Y., Boersma, K. F., Gast, L., Wittrock, F., Brunner, D.,
1504 Zhou, Y., and Van Roozendael, M.: Eight-component retrievals from ground-based MAX-
1505 DOAS observations, *Atmos. Meas. Tech.*, 4, 1027-1044, <https://doi.org/10.5194/amt-4-1027-2011>, 2011.

1507

1508 Irie, H., Nakayama, T., Shimizu, A., Yamazaki, A., Nagai, T., Uchiyama, A., Zaizen, Y.,
1509 Kagamitani, S., and Matsumi, Y.: Evaluation of MAX-DOAS aerosol retrievals by coincident
1510 observations using CRDS, lidar, and sky radiometer in Tsukuba, Japan, *Atmos. Meas. Tech.*,
1511 8, 2775-2788, <https://doi.org/10.5194/amt-8-2775-2015>, 2015.

1512

1513 Kanaya, Y., Irie, H., Takashima, H., Iwabuchi, H., Akimoto, H., Sudo, K., Gu, M., Chong, J.,
1514 Kim, Y. J., Lee, H., Li, A., Si, F., Xu, J., Xie, P.-H., Liu, W.-Q., Dzhola, A., Postylyakov, O.,
1515 Ivanov, V., Grechko, E., Terpugova, S., and Panchenko, M.: Long-term MAX-DOAS
1516 network observations of NO₂ in Russia and Asia (MADRAS) during the period 2007–2012:
1517 instrumentation, elucidation of climatology, and comparisons with OMI satellite observations
1518 and global model simulations, *Atmos. Chem. Phys.*, 14, 7909-7927,
1519 <https://doi.org/10.5194/acp-14-7909-2014>, 2014.

1520

1521 Kreher, K., M. Van Roozendael, F. Hendrick, A. Apituley, E. Dimitropoulou, U. Friess, A.
1522 Richter, T. Wagner, L. Ang, M. Anguas, A. Bais, N. Benavent, K. Bognar, A. Borovski, I.
1523 Bruchkovsky, A. Cede, K.L. Chan, S. Donner, T. Drosoglou, C. Fayt, H. Finkenzeller, N.
1524 Hao, C. Hermans, S. Hoque, H. Irie, J. Jin, P. Johnston, J. Khayyam Butt, F. Khokhar, T.
1525 Koenig, J. Ma, A. K. Mishra, M. Navarro-Comas, A. Pazmino, E. Peters, M. Pinharanda, A.
1526 Piters, O. Postylyakov, C. Prados, O. Rodriguez, R. Querel, A. Saiz-Lopez, S. Schreier, A.
1527 Seyler, E. Spinei, K. Strong, M. Tiefengraber, J.-L. Tirpitz4, V. Kumar, R. Volkamer, M.
1528 Wenig, P. Xie, J. Xu, M. Yela, X. Zhao, W. Zhuoru, Intercomparison of NO₂, O₄, O₃ and
1529 HCHO slant column measurements by MAX-DOAS and zenith-sky UV-Visible
1530 spectrometers, to be submitted to Atmos. Meas. Tech. 2019.

1531

1532 Krautwurst, S.: Charakterisierung eines neu aufgebauten MAXDOAS-Systems und
1533 Interpretation von ersten Messergebnissen zu dem Spurenstoff NO₂, Diplomarbeit,
1534 Fachhochschule Coburg, Coburg, Germany, 2010.

1535

1536 Lampel, J., Frieß, U., and Platt, U.: The impact of vibrational Raman scattering of air on
1537 DOAS measurements of atmospheric trace gases, *Atmos. Meas. Tech.*, 8, 3767–3787,
1538 <https://doi.org/10.5194/amt-8-3767-2015>, 2015.

1539

1540 Lampel, J., Pöhler, D., Polyansky, O. L., Kyuberis, A. A., Zobov, N. F., Tennyson, J., Lodi,
1541 L., Frieß, U., Wang, Y., Beirle, S., Platt, U., and Wagner, T.: Detection of water vapour
1542 absorption around 363 nm in measured atmospheric absorption spectra and its effect on
1543 DOAS evaluations, *Atmos. Chem. Phys.*, 17, 1271-1295, <https://doi.org/10.5194/acp-17-1271-2017>, 2017.

1545

1546 Lorente, A., Folkert Boersma, K., Yu, H., Dörner, S., Hilboll, A., Richter, A., Liu, M.,
1547 Lamsal, L. N., Barkley, M., De Smedt, I., Van Roozendael, M., Wang, Y., Wagner, T., Beirle,
1548 S., Lin, J.-T., Krotkov, N., Stammes, P., Wang, P., Eskes, H. J., and Krol, M.: Structural
1549 uncertainty in air mass factor calculation for NO₂ and HCHO satellite retrievals, *Atmos.*
1550 *Meas. Tech.*, 10, 759-782, <https://doi.org/10.5194/amt-10-759-2017>, 2017.

1551

1552 Meller, R. and G. K. Moortgat, Temperature dependence of the absorption cross sections of
 1553 formaldehyde between 223 and 323 K in the wavelength range 225–375 nm, *J. Geophys. Res.*,
 1554 105, 7089–7101, 2000.

1555

1556 Merlaud, A., Van Roozendael, M., Theys, N., Fayt, C., Hermans, C., Quennhen, B.,
 1557 Schwarzenboeck, A., Ancellet, G., Pommier, M., Pelon, J., Burkhardt, J., Stohl, A., and De
 1558 Mazière, M.: Airborne DOAS measurements in Arctic: vertical distributions of aerosol
 1559 extinction coefficient and NO₂ concentration, *Atmos. Chem. Phys.*, 11, 9219–9236,
 1560 doi:10.5194/acp-11-9219-2011, 2011.

1561

1562 Ortega, I., Berg, L. K., Ferrare, R. A., Hair, J. W., Hostetler, C. A., and Volkamer, R.:
 1563 Elevated aerosol layers modify the O₂-O₂ absorption measured by ground-based MAX-
 1564 DOAS, *J. Quant. Spectrosc. Ra.*, 176, 34–49, doi:10.1016/j.jqsrt.2016.02.021, 2016.

1565

1566 Paur, R. J. and Bass, A. M.: The Ultraviolet Cross-Sections of Ozone: II. Results and
 1567 temperature dependence, in: *Atmospheric ozone; Proc. Quadrennial Ozone Symposium*,
 1568 edited by: Zeferos, C. S. and Ghazi, A., Halkidiki Greece, 1984, Dordrecht: Reidel, D., 611–
 1569 615, 1984.

1570

1571 Peters, E., Wittrock, F., Großmann, K., Frieß, U., Richter, A., and Burrows, J. P.:
 1572 Formaldehyde and nitrogen dioxide over the remote western Pacific Ocean: SCIAMACHY
 1573 and GOME-2 validation using ship-based MAX-DOAS observations, *Atmos. Chem. Phys.*,
 1574 12, 11179–11197, <https://doi.org/10.5194/acp-12-11179-2012>, 2012a.

1575

1576 Peters, E., Wittrock, F., Großmann, K., Frieß, U., Richter, A., and Burrows, J. P.:
 1577 Formaldehyde and nitrogen dioxide over the remote western Pacific Ocean: SCIAMACHY
 1578 and GOME-2 validation using ship-based MAX-DOAS observations, *Atmos.*
 1579 *Chem. Phys.*, 12, 11179–11197, <https://doi.org/10.5194/acp-12-11179-2012>, 2012b.

1580

1581 Pinardi, G., Van Roozendael, M., Abuhassan, N., Adams, C., Cede, A., Clémer, K., Fayt, C.,
 1582 Frieß, U., Gil, M., Herman, J., Hermans, C., Hendrick, F., Irie, H., Merlaud, A., Navarro
 1583 Comas, M., Peters, E., Piters, A. J. M., Puentedura, O., Richter, A., Schönhardt, A.,
 1584 Shaiganfar, R., Spinei, E., Strong, K., Takashima, H., Vrekoussis, M., Wagner, T., Wittrock,
 1585 F., and Yilmaz, S.: MAX-DOAS formaldehyde slant column measurements during CINDI:
 1586 intercomparison and analysis improvement, *Atmos. Meas. Tech.*, 6, 167–185,
 1587 <https://doi.org/10.5194/amt-6-167-2013>, 2013.

1588

1589 Polyansky, O.L., A.A. Kyuberis, N.F. Zobov, J. Tennyson, S.N. Yurchenko and L. Lodi
 1590 ExoMol molecular line lists XXX: a complete high-accuracy line list for water, *Mon. Not. R.*
 1591 *astr. Soc.*, submitted, 2018.

1592

1593 Prados-Roman, C., Butz, A., Deutschmann, T., Dorf, M., Kritten, L., Minikin, A., Platt, U.,
 1594 Schlager, H., Sihler, H., Theys, N., Van Roozendael, M., Wagner, T., and Pfeilsticker, K.:
 1595 Airborne DOAS limb measurements of tropospheric trace gas profiles: case studies on the
 1596 profile retrieval of O₄ and BrO, *Atmos. Meas. Tech.*, 4, 1241–1260, doi:10.5194/amt-4-1241-
 1597 2011, 2011.

1598

1599 Pukštė, J., Kühl, S., Deutschmann, T., Platt, U., and Wagner, T.: Extending differential optical
 1600 absorption spectroscopy for limb measurements in the UV, *Atmos. Meas. Tech.*, 3, 631–653,
 1601 doi:10.5194/amt-3-631-2010, 2010.

1602

1603 Schreier, S. F., Richter, A., Wittrock, F., and Burrows, J. P.: Estimates of free-tropospheric
1604 NO₂ and HCHO mixing ratios derived from high-altitude mountain MAX-DOAS
1605 observations at midlatitudes and in the tropics, *Atmos. Chem. Phys.*, 16, 2803-2817,
1606 <https://doi.org/10.5194/acp-16-2803-2016>, 2016.

1607

1608 Serdyuchenko, A., Gorshelev, V., Weber, M., Chehade, W., and Burrows, J. P.: High spectral
1609 resolution ozone absorption cross-sections – Part 2: Temperature dependence, *Atmos. Meas.*
1610 *Tech.*, 7, 625-636, <https://doi.org/10.5194/amt-7-625-2014>, 2014.

1611

1612 Seyler, A., Wittrock, F., Kattner, L., Mathieu-Üffing, B., Peters, E., Richter, A., Schmolke, S.,
1613 and Burrows, J. P.: Monitoring shipping emissions in the German Bight using MAX-DOAS
1614 measurements, *Atmos. Chem. Phys.*, 17, 10997-11023, <https://doi.org/10.5194/acp-17-10997-2017>, 2017.

1616

1617 Sneep, M., de Haan, J. F., Stammes, P., Wang, P., Vanbause, C., Joiner, J., Vasilkov, A. P.,
1618 and Levelt, P. F.: Three-way comparison between OMI and PARASOL cloud pressure
1619 products, *J. Geophys. Res.*, 113, D15S23, doi:10.1029/2007JD008694, 2008.

1620

1621 Solomon, S., A. L. Schmeltekopf, and R. W. Sanders, On the interpretation of zenith sky
1622 absorption measurements, *J. Geophys. Res.*, 92, 8311-8319, 1987.

1623

1624 Spinei, E., Cede, A., Herman, J., Mount, G. H., Eloranta, E., Morley, B., Baidar, S., Dix, B.,
1625 Ortega, I., Koenig, T., and Volkamer, R.: Ground-based direct-sun DOAS and airborne
1626 MAX-DOAS measurements of the collision-induced oxygen complex, O₂O₂, absorption with
1627 significant pressure and temperature differences, *Atmos. Meas. Tech.*, 8, 793-809,
1628 <https://doi.org/10.5194/amt-8-793-2015>, 2015.

1629

1630 Spurr RJD, Kurosu TP, Chance KV. A linearized discrete ordinate radiative transfer model
1631 for atmospheric remote sensing retrieval. *JQSRT* 2001;68:689–735.

1632

1633 Spurr, R., LIDORT and VLIDORT: Linearized Pseudo-Spherical Scalar and Vector Discrete
1634 Ordinate Radiative Transfer Models for Use in Remote Sensing Retrieval Problems, Light
1635 Scattering Reviews, Vol. 3, edited by: Kokhanovsky, A., Springer, Berlin Heidelberg,
1636 Germany, 2008.

1637

1638 Stammes K, Tsay S-C, Wiscombe W, Jayaweera K. Numerically stable algorithm for discrete
1639 ordinate method radiative transfer in multiple scattering and emitting layered media. *Appl Opt*
1640 1988; 27:2502-9.

1641

1642 Thalman, R. and Volkamer, R.: Inherent calibration of a blue LED-CE-DOAS instrument to
1643 measure iodine oxide, glyoxal, methyl glyoxal, nitrogen dioxide, water vapour and aerosol
1644 extinction in open cavity mode, *Atmos. Meas. Tech.*, 3, 1797-1814, 2010.

1645

1646 Thalman, R. and Volkamer, R.: Temperature dependent absorption cross-sections of O₂–O₂
1647 collision pairs between 340 and 630 nm and at atmospherically relevant pressure, *Phys.*
1648 *Chem. Chem. Phys.*, 15, 15371, doi:10.1039/c3cp50968k, 2013.

1649

1650 United States Committee on Extension to the Standard Atmosphere: U.S. Standard
1651 Atmosphere, 1976, National Oceanic and Atmospheric Administration, National Aeronautics
1652 and Space Administration, United States Air Force, Washington D.C., 1976.

1653

1654 Vandaele, A. C., C. Hermans, P. C. Simon, M. Carleer, R. Colin, S. Fally, M.-F. Mérienne, A.
1655 Jenouvier, and B. Coquart, Measurements of the NO₂ Absorption Cross-section from 42000
1656 cm⁻¹ to 10000 cm⁻¹ (238-1000 nm) at 220 K and 294 K, *J. Quant. Spectrosc. Radiat.*
1657 *Transfer*, 59, 171-184, 1997.

1658

1659 Vlemmix, T., Piters, A. J. M., Berkhouit, A. J. C., Gast, L. F. L., Wang, P., and Levelt, P. F.:
1660 Ability of the MAX-DOAS method to derive profile information for NO₂: can the boundary
1661 layer and free troposphere be separated?, *Atmos. Meas. Tech.*, 4, 2659-2684,
1662 <https://doi.org/10.5194/amt-4-2659-2011>, 2011.

1663

1664 Vlemmix, T., Hendrick, F., Pinardi, G., De Smedt, I., Fayt, C., Hermans, C., Piters, A., Wang,
1665 P., Levelt, P., and Van Roozendael, M.: MAX-DOAS observations of aerosols, formaldehyde
1666 and nitrogen dioxide in the Beijing area: comparison of two profile retrieval approaches,
1667 *Atmos. Meas. Tech.*, 8, 941-963, <https://doi.org/10.5194/amt-8-941-2015>, 2015.

1668

1669 Volkamer, R., Baidar, S., Campos, T. L., Coburn, S., DiGangi, J. P., Dix, B., Eloranta, E. W.,
1670 Koenig, T. K., Morley, B., Ortega, I., Pierce, B. R., Reeves, M., Sinreich, R., Wang, S.,
1671 Zondlo, M. A., and Romashkin, P. A.: Aircraft measurements of BrO, IO, glyoxal, NO₂, H₂O,
1672 O₂-O₂ and aerosol extinction profiles in the tropics: comparison with aircraft-/ship-based in
1673 situ and lidar measurements, *Atmos. Meas. Tech.*, 8, 2121-2148, 2015.

1674

1675 Wagner, T., F. Erle, L. Marquard, C. Otten, K. Pfeilsticker, T. Senne, J. Stutz, and U. Platt,
1676 Cloudy sky optical paths as derived from differential optical absorption spectroscopy
1677 observations, *J. Geophys. Res.*, 103, 25307-25321, 1998.

1678

1679 Wagner, T., B. Dix, C.v. Friedeburg, U. Friess, S. Sanghavi, R. Sinreich, and U. Platt MAX-
1680 DOAS O₄ measurements – a new technique to derive information on atmospheric aerosols.
1681 (I) Principles and information content, *J. Geophys. Res.*, 109, doi: 10.1029/2004JD004904,
1682 2004.

1683

1684 Wagner, T., J. P. Burrows, T. Deutschmann, B. Dix, C. von Friedeburg, U. Friess, F.
1685 Hendrick, K.-P. Heue, H. Irie, H. Iwabuchi, Y. Kanaya, J. Keller, C. A. McLinden, H. Oetjen,
1686 E. Palazzi, A. Petritoli, U. Platt, O. Postylyakov, J. Pukite, A. Richter, M. van Roozendael, A.
1687 Rozanov, V. Rozanov, R. Sinreich, S. Sanghavi, F. Wittrock, Comparison of Box-Air-Mass-
1688 Factors and Radiances for Multiple-Axis Differential Optical Absorption Spectroscopy
1689 (MAX-DOAS) Geometries calculated from different UV/visible Radiative Transfer Models,
1690 *Atmos. Chem. Phys.*, 7, 1809-1833, 2007.

1691

1692 Wagner, T., Deutschmann, T., and Platt, U.: Determination of aerosol properties from MAX-
1693 DOAS observations of the Ring effect, *Atmos. Meas. Tech.*, 2, 495-512, 2009.

1694

1695 Wagner, T., Beirle, S., Deutschmann, T., and Penning de Vries, M.: A sensitivity analysis of
1696 Ring effect to aerosol properties and comparison to satellite observations, *Atmos. Meas.*
1697 *Tech.*, 3, 1723-1751, doi:10.5194/amt-3-1723-2010, 2010.

1698

1699 Wang, T., Hendrick, F., Wang, P., Tang, G., Clémer, K., Yu, H., Fayt, C., Hermans, C.,
1700 Gielen, C., Müller, J.-F., Pinardi, G., Theys, N., Brenot, H., and Van Roozendael, M.:
1701 Evaluation of tropospheric SO₂ retrieved from MAX-DOAS measurements in Xianghe,
1702 China, *Atmos. Chem. Phys.*, 14, 11149-11164, <https://doi.org/10.5194/acp-14-11149-2014>,
1703 2014.

1704

1705 Wang, S., Cuevas, C. A., Frieß, U., and Saiz-Lopez, A.: MAX-DOAS retrieval of aerosol
1706 extinction properties in Madrid, Spain, *Atmos. Meas. Tech.*, 9, 5089-5101,
1707 <https://doi.org/10.5194/amt-9-5089-2016>, 2016.

1708

1709 Wang, Y., Beirle, S., Lampel, J., Koukouli, M., De Smedt, I., Theys, N., Li, A., Wu, D., Xie,
1710 P., Liu, C., Van Roozendael, M., Stavrakou, T., Müller, J.-F., and Wagner, T.: Validation of
1711 OMI, GOME-2A and GOME-2B tropospheric NO₂, SO₂ and HCHO products using MAX-
1712 DOAS observations from 2011 to 2014 in Wuxi, China: investigation of the effects of priori
1713 profiles and aerosols on the satellite products, *Atmos. Chem. Phys.*, 17, 5007-5033,
1714 <https://doi.org/10.5194/acp-17-5007-2017>, 2017a.

1715

1716 Wang, Y., Lampel, J., Xie, P., Beirle, S., Li, A., Wu, D., and Wagner, T.: Ground-based
1717 MAX-DOAS observations of tropospheric aerosols, NO₂, SO₂ and HCHO in Wuxi, China,
1718 from 2011 to 2014, *Atmos. Chem. Phys.*, 17, 2189–2215, doi:10.5194/acp-17-2189-2017,
1719 2017b.

1720

1721 Wang, Y., Beirle, S., Hendrick, F., Hilboll, A., Jin, J., Kyuberis, A. A., Lampel, J., Li, A.,
1722 Luo, Y., Lodi, L., Ma, J., Navarro, M., Ortega, I., Peters, E., Polyansky, O. L., Remmers, J.,
1723 Richter, A., Puentedura, O., Van Roozendael, M., Seyler, A., Tennyson, J., Volkamer, R.,
1724 Xie, P., Zobov, N. F., and Wagner, T.: MAX-DOAS measurements of HONO slant column
1725 densities during the MAD-CAT campaign: inter-comparison, sensitivity studies on spectral
1726 analysis settings, and error budget, *Atmos. Meas. Tech.*, 10, 3719-3742,
1727 <https://doi.org/10.5194/amt-10-3719-2017>, 2017c.

1728

1729 Wiegner, M. and Geiß, A.: Aerosol profiling with the Jenoptik ceilometer CHM15kx, *Atmos.*
1730 *Meas. Tech.*, 5, 1953-1964, <https://doi.org/10.5194/amt-5-1953-2012>, 2012.

1731

1732 Winterrath, T., T. P. Kurosu, A. Richter and J. P. Burrows, Enhanced O₃ and NO₂ in
1733 thunderstorm clouds: convection or production?, *Geophys. Res. Lett.*, No. 26, pp. 1291-1294,
1734 1999.

1735

1736 Wittrock, F., H. Oetjen, A. Richter, S. Fietkau, T. Medeke, A. Rozanov, J. P. Burrows
1737 MAX-DOAS measurements of atmospheric trace gases in Ny-Ålesund - Radiative transfer
1738 studies and their application, *Atmos. Chem. Phys.*, 4, 955-966, 2004

1739

1740 Zieger, P., Weingartner, E., Henzing, J., Moerman, M., de Leeuw, G., Mikkilä, J., Ehn, M.,
1741 Petäjä, T., Clément, K., van Roozendael, M., Yilmaz, S., Frieß, U., Irie, H., Wagner, T.,
1742 Shaiganfar, R., Beirle, S., Apituley, A., Wilson, K., and Baltensperger, U.: Comparison of
1743 ambient aerosol extinction coefficients obtained from in-situ, MAX-DOAS and LIDAR
1744 measurements at Cabauw, *Atmos. Chem. Phys.*, 11, 2603-2624, <https://doi.org/10.5194/acp-11-2603-2011>, 2011.

1746

1747

1748

1749

1750

1751

1752

1753

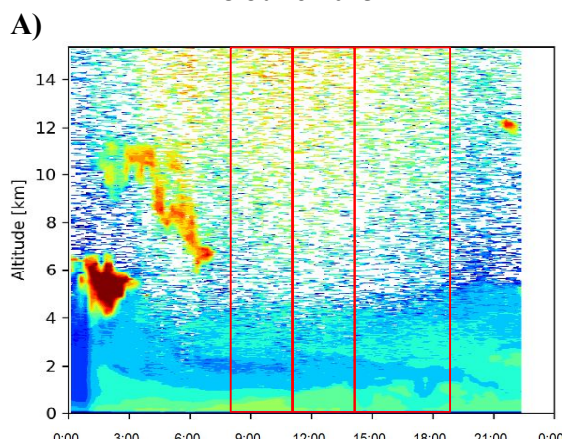
1754

1755

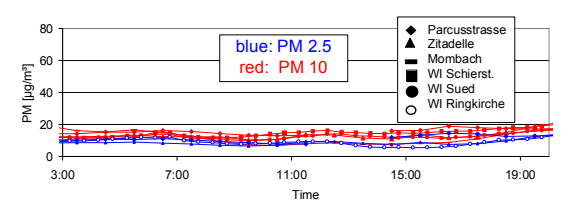
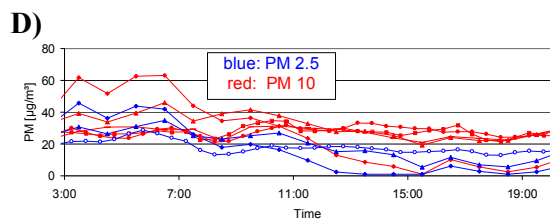
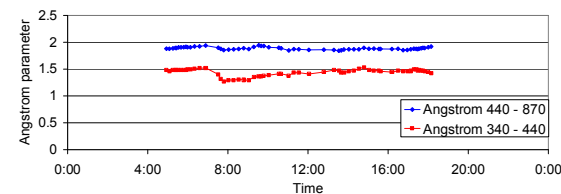
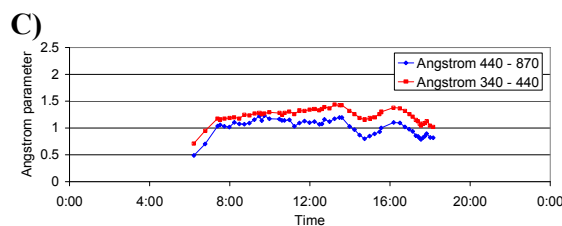
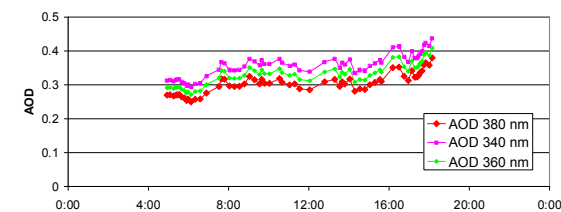
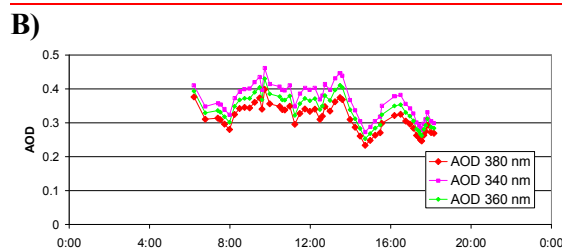
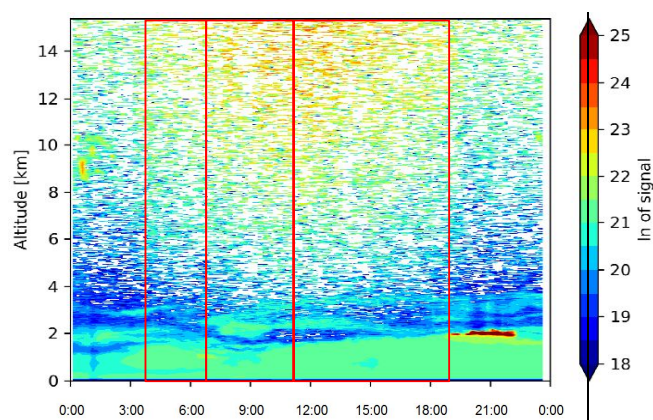
1756
1757
1758
1759
1760
1761
1762
1763
1764
1765
1766
1767
1768
1769
1770
1771
1772

Figures

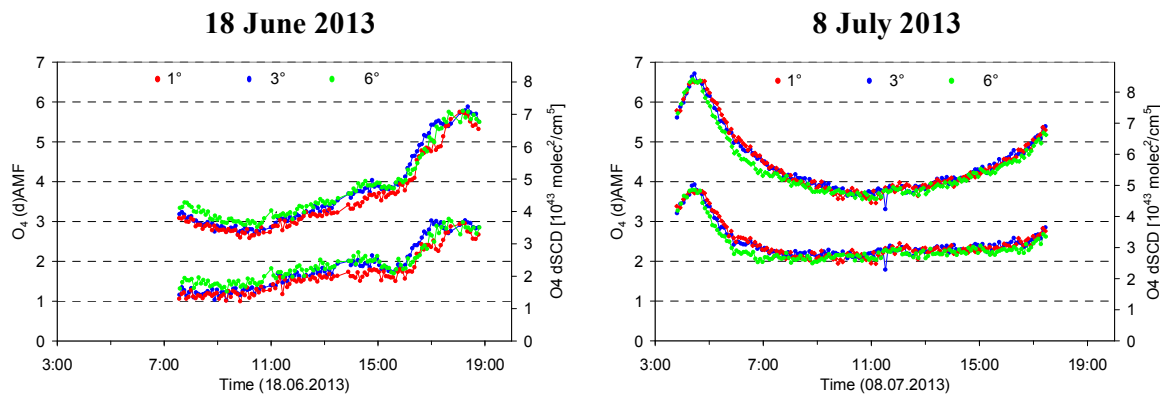
18 June 2013



8 July 2013

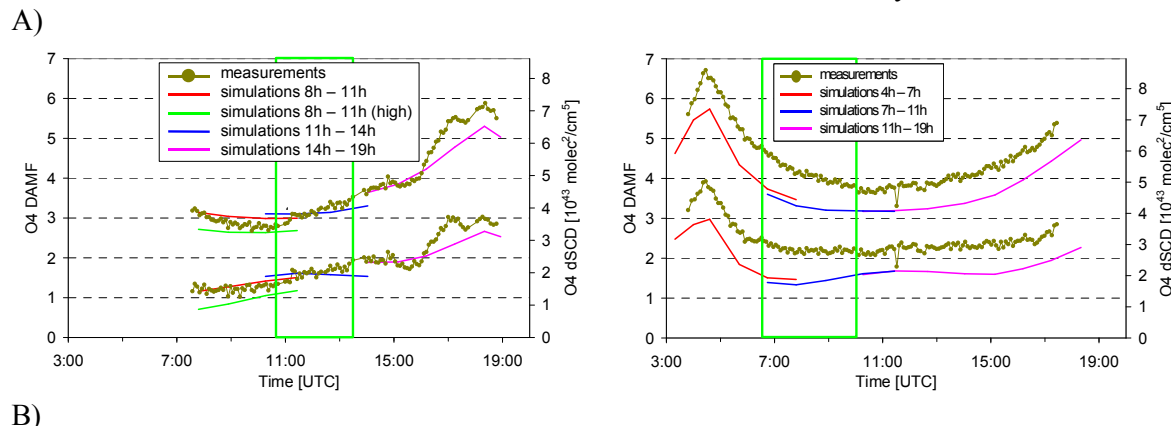


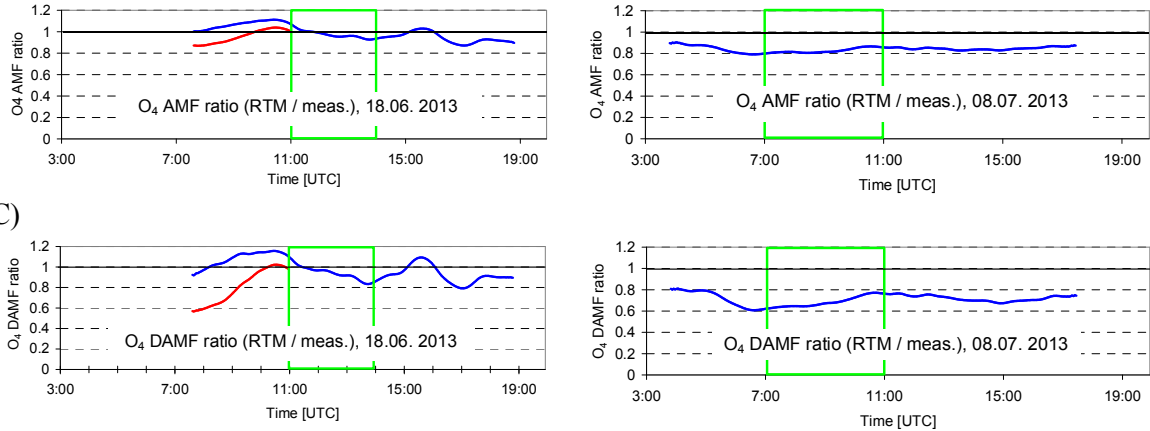
1773 Fig. 1 Various aerosol properties on the two selected days (left: 18 June 2013; right: 8 July
 1774 2013). A) Aerosol backscatter profiles from ceilometer measurements; B) AOD at 340, 360,
 1775 and 380 nm (360 values are interpolated from 340 and 380 nm) from AERONET sun
 1776 photometer measurements; C) Ångström parameters for two wavelength pairs (340 – 440 nm
 1777 and 440 – 870 nm) from AERONET sun photometer measurements; D) Surface in situ
 1778 measurements of $\text{PM}_{2.5}$ and PM_{10} measured at different air quality monitoring stations in
 1779 Mainz and the nearby city of Wiesbaden .



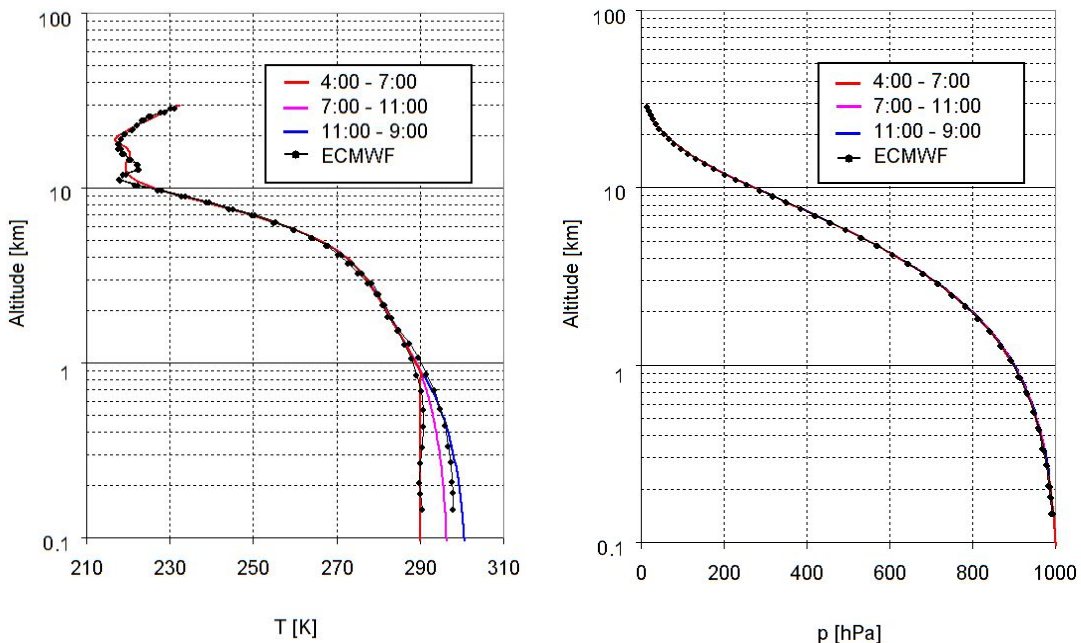
1788 Fig. 2 O_4 AMFs (upper lines) and dAMFs (lower lines) for 1° , 3° , and 6° elevation angles
 1789 derived from the MPIC MAX-DOAS measurements on the two selected days. Interestingly,
 1790 on 18 June the lowest values are in general found for the lowest elevation angles, which is an
 1791 indication for the high aerosol load close to the surface. The y-axis on the right side shows the
 1792 corresponding O_4 (d)SCDs for O_4 VCDs of $1.23 \cdot 10^{43} \text{ molec}^2/\text{cm}^5$ and of $1.28 \cdot 10^{43}$
 1793 $\text{molec}^2/\text{cm}^5$ for 18 June and 08 July, respectively (see section 4.1.2).

18 June 2013 08 July 2013





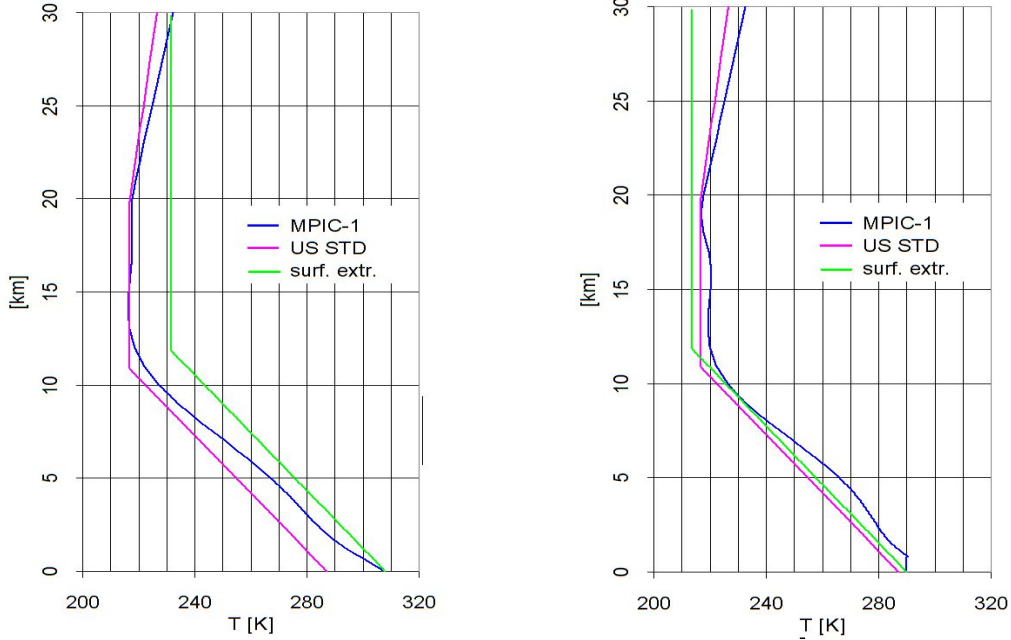
1796 Fig. 3 A) Comparison of O_4 (d)AMFs from MAX-DOAS measurements and forward model
1797 simulations for the two selected days. The green rectangle indicates the middle periods on
1798 both days, which are the focus of the quantitative comparison. The green line on 18 June
1799 represents forward model results for a modified aerosol profile (see text). The y-axis on the
1800 right side shows the corresponding O_4 (d)SCDs for O_4 VCDs of $1.23 \cdot 10^{43}$ molec 2 /cm 5 and of
1801 $1.28 \cdot 10^{43}$ molec 2 /cm 5 for 18 June and 08 July, respectively (see section 4.1.2). In B) and C)
1802 the ratios of the simulated and measured AMFs and dAMFs are shown, respectively. The red
1803 line on 18 June represents the ratios for the modified aerosol scenario.
1804



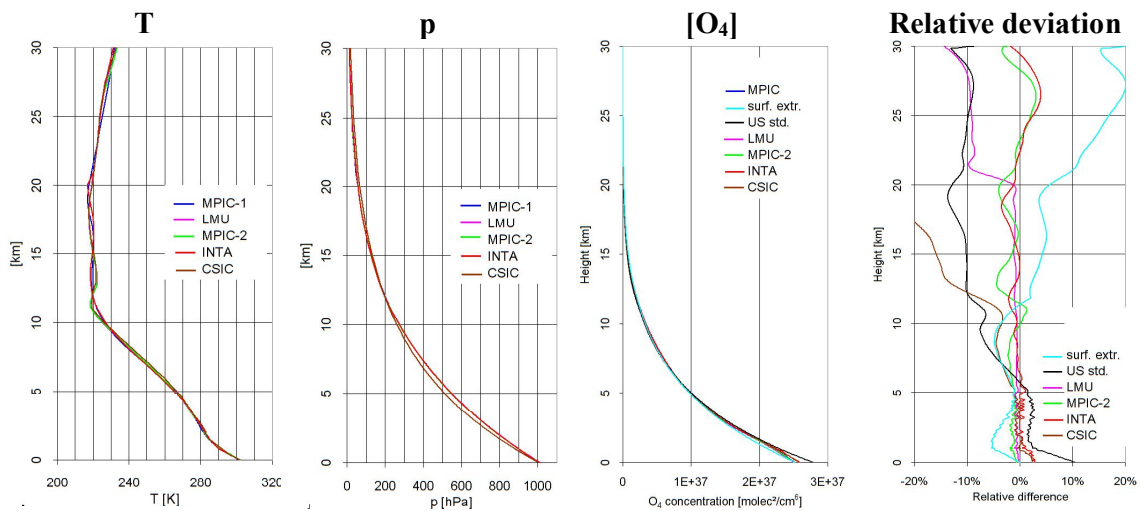
1805 Fig. 4 Extracted temperature (left) and pressure (right) profiles for the three periods on 8 July
1806 2013. Also shown are ECMWF profiles above Mainz for 6:00 and 18:00. To better account
1807 for the diurnal variation of the temperatures near the surface, below 1 km the temperature is
1808 linearly interpolated between the surface measurements and the ECMWF temperatures at 1
1809 km (for details see text). Note that the altitude is given relative to the height of the
1810 measurement site (150 m).
1811

18 June 14:00 – 19:00

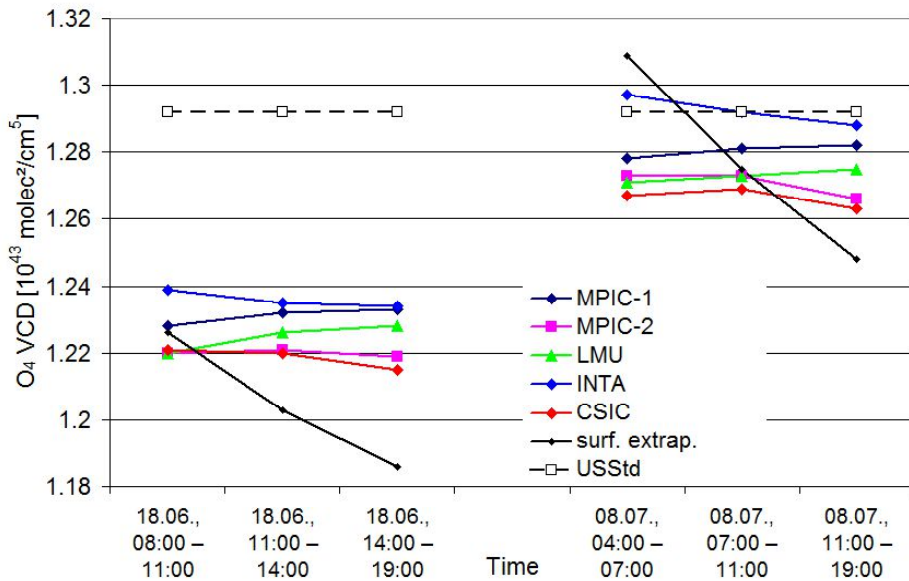
8 July 4:00 – 7:00



1812 Fig. 5 Temperature profiles extracted in different ways for two periods (Left: 18 June 14:00 –
1813 19:00; right: 8 July 4:00 – 7:00). The blue profiles are extracted from in situ measurements
1814 and ECMWF profiles as described in the text. The green profiles are extracted from the
1815 surface temperatures and assuming a constant lapse rate of $-6.5\text{K} / \text{km}$ up to 12 km and a
1816 constant temperature above. The pink curves represent the temperature profile from the US
1817 standard atmosphere.
1818

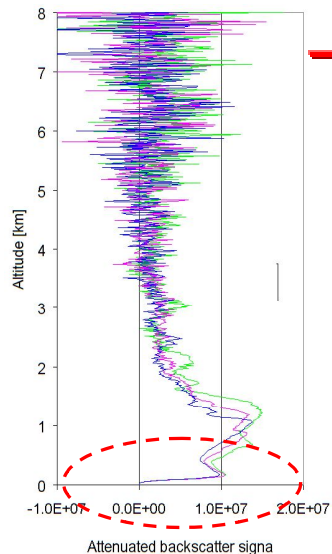


1819 Fig. 6 Comparison of the vertical profiles of temperature, pressure and O_4 concentration
1820 (expressed as the square of the O_2 concentration) for 8 July, 11:00 – 19:00, extracted by the
1821 different groups. In the right figure the relative deviations of the O_4 concentration compared
1822 to the MPIC standard extraction are shown. There, also the profiles derived from the
1823 extrapolation from the surface values and the US standard atmosphere are included.
1824
1825



1826
1827
1828 Fig. 7 Comparison of the O₄ VCDs for the selected periods on both days calculated from the
1829 profiles extracted by the different groups. Also the results for the profiles extrapolated from
1830 the surface values and the US standard atmosphere are shown.

1831
1832
1833
1834
1835
1836
1837
1838
Ceilometer backscatter
profiles at 1064 nm
(hourly averages)

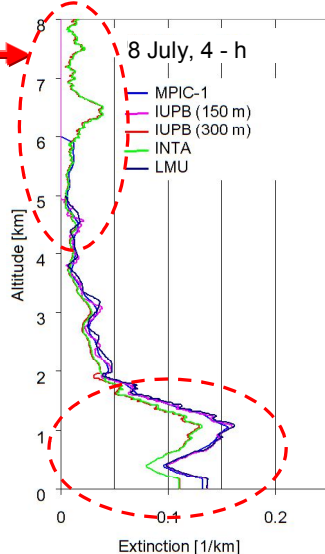


The backscatter profiles are converted into extinction profiles by scaling with the AOD from the sun photometer.

The self attenuation of the aerosol is accounted for.

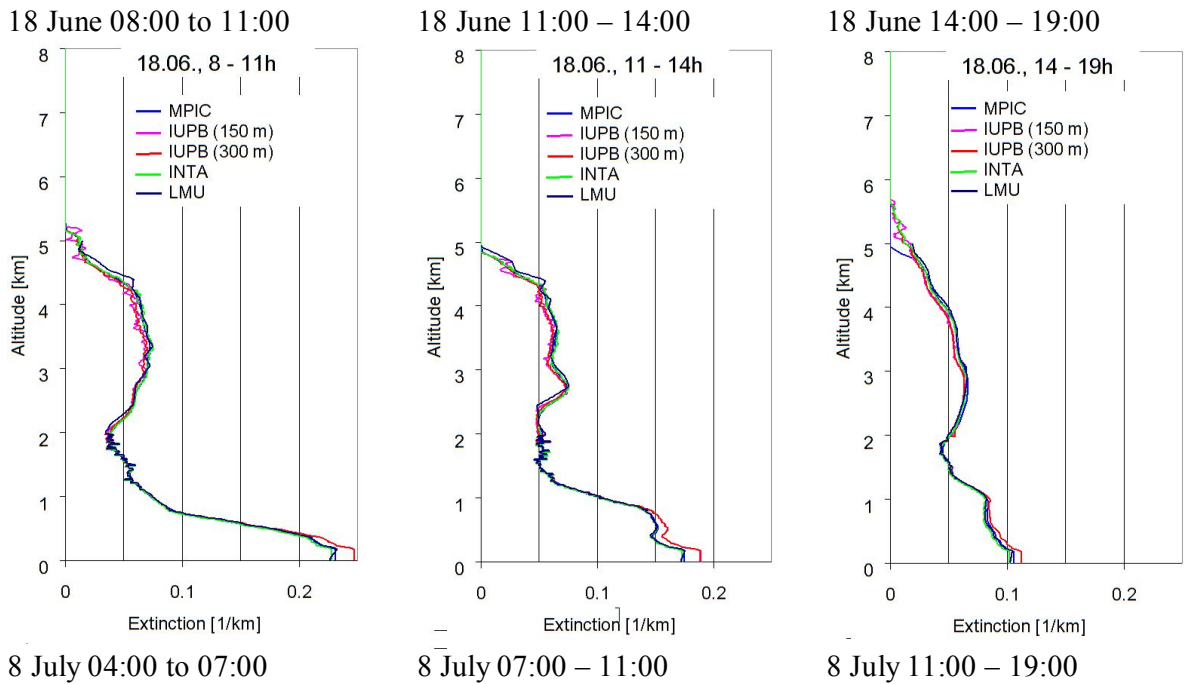
Below 180m, the profiles are extrapolated (constant value, or constant or double slope).

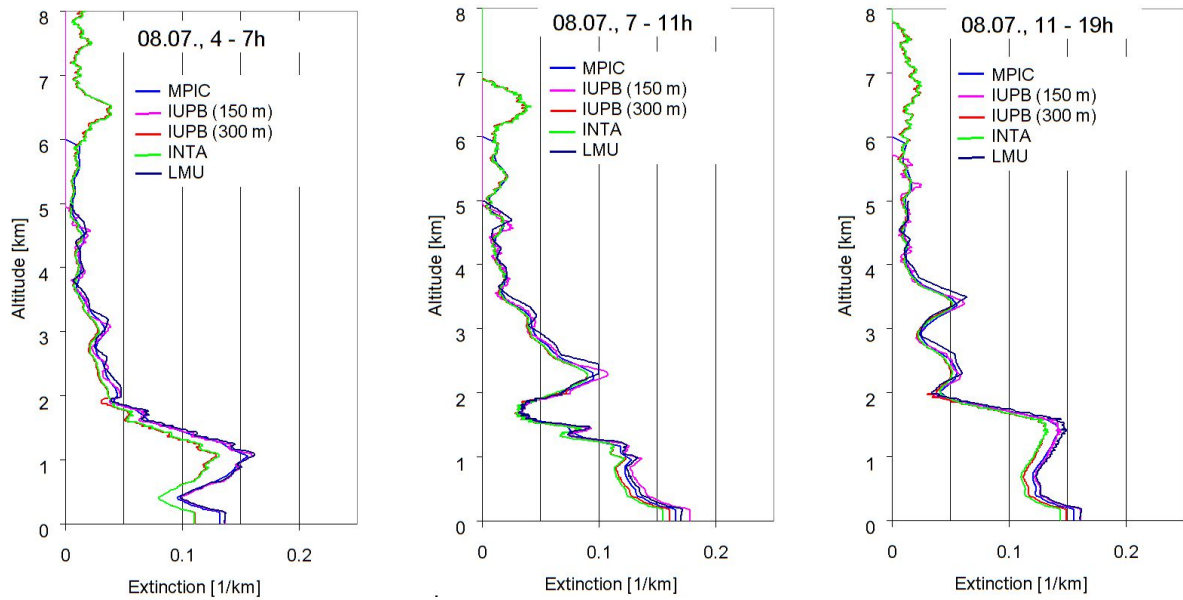
Extinction profiles at
360 nm derived by
different groups



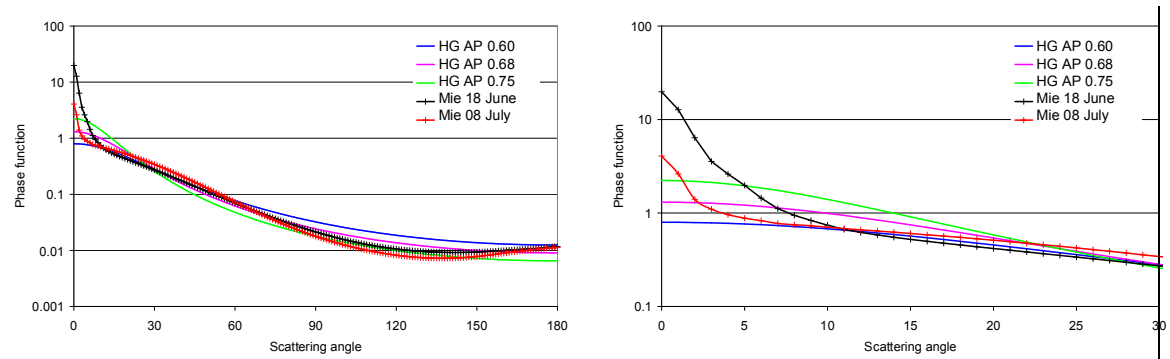
1839
1840 Fig. 8 Left: Hourly averaged backscatter profiles from the ceilometer measurements for the
1841 period 4:00 – 7:00 on 8 July 2013. Below 180 m the values rapidly decrease to zero due to the

1842 missing overlap between the outgoing beam and the field of view of the telescope. Right:
 1843 Aerosol extinction profiles extracted by the different groups from the ceilometer profiles
 1844 (assuming a constant extinction below 180 m). The red circles indicate the height intervals
 1845 with the largest deviations (IUPB 150 m and IUPB 300 m indicate profile extractions with
 1846 different widths of the smoothing kernels: Hanning windows of 150 and 300 m, respectively).
 1847
 1848
 1849
 1850
 1851
 1852
 1853
 1854
 1855
 1856
 1857
 1858
 1859
 1860
 1861
 1862
 1863
 1864
 1865
 1866
 1867
 1868
 1869
 1870
 1871





1872 Fig. 9 Comparison of the aerosol extinction profiles extracted by the different groups for all
 1873 three periods on both days.

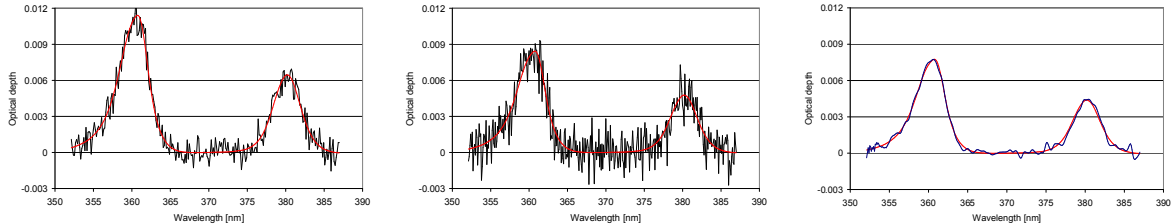


1886 Fig. 10 Comparison of different aerosol phase functions used in the radiative transfer
 1887 simulations. The right figure is a zoom of the left figure.

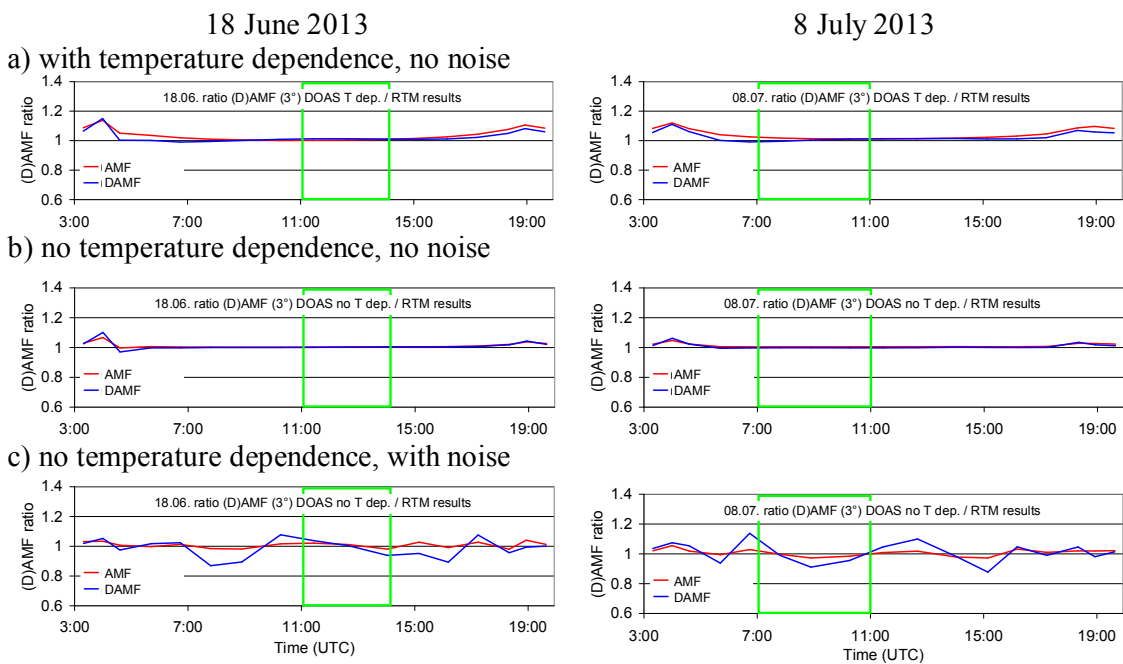
Real measurements
 $2.71 \cdot 10^{43} \text{ molec}^2/\text{cm}^5$

Synthetic spectra with noise
 $2.00 \cdot 10^{43} \text{ molec}^2/\text{cm}^5$

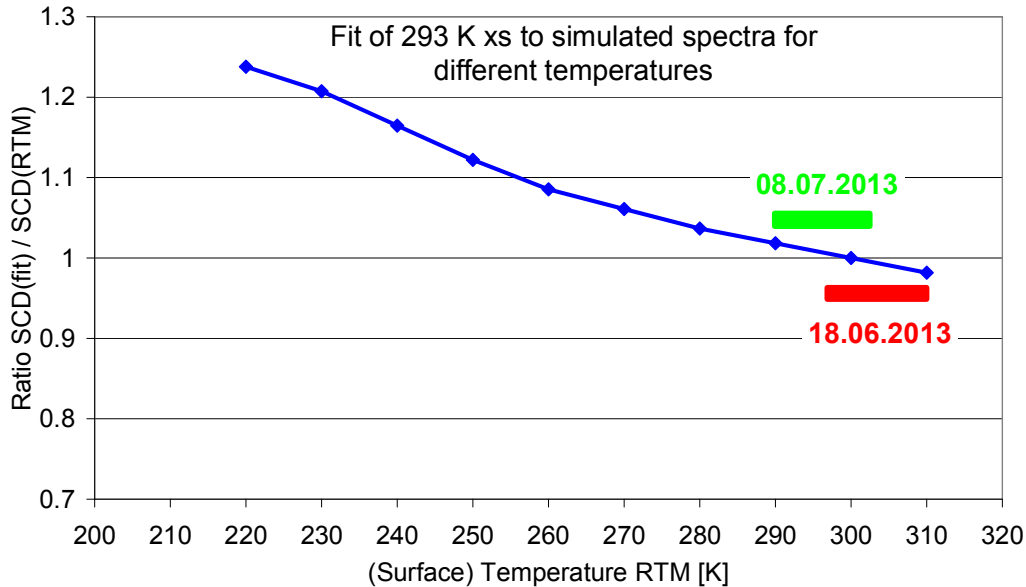
Synthetic spectra without noise
 $1.84 \cdot 10^{43} \text{ molec}^2/\text{cm}^5$



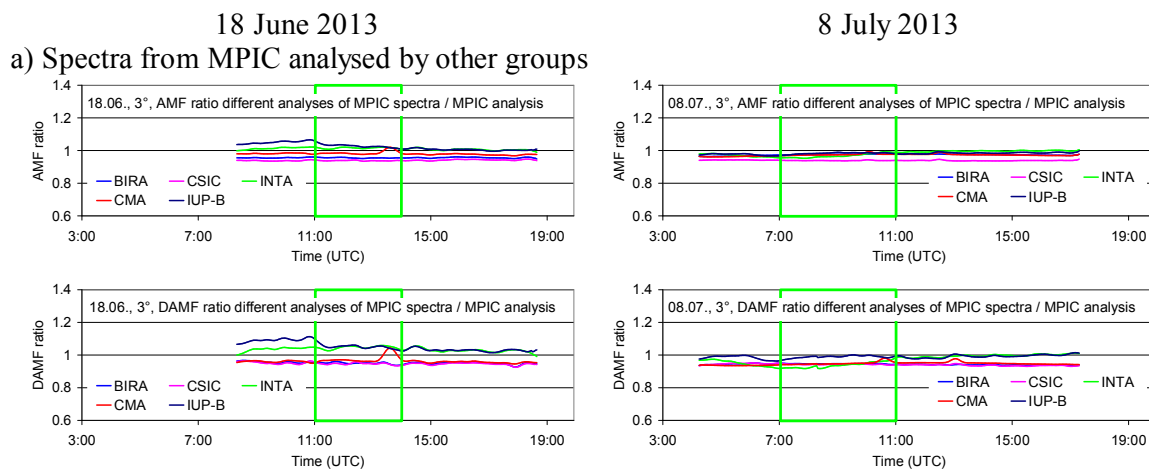
1892 Fig. 11 Spectral analysis results for a real measurement from the MPIC instrument (left) and a
 1893 synthetic spectrum with and without noise. Spectra are taken from 8 July 2013 at 11:26
 1894 (elevation angle = 1°). The derived O₄ dSCD is shown above the individual plots.
 1895
 1896
 1897
 1898
 1899
 1900
 1901
 1902
 1903
 1904
 1905
 1906
 1907
 1908
 1909
 1910
 1911
 1912
 1913
 1914
 1915



1916 Fig. 12 Ratio of the O₄ (d)AMFs derived from synthetic spectra versus those obtained from
 1917 radiative transfer simulations at 360 nm for both selected days.

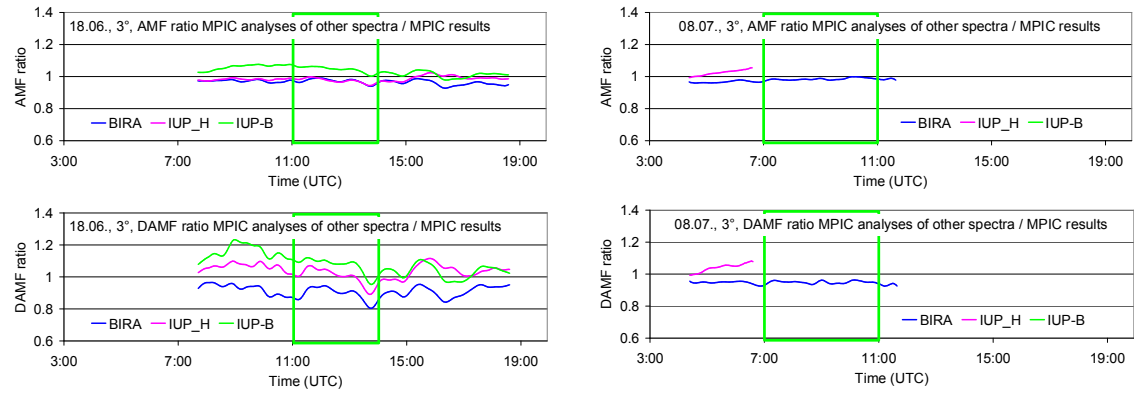


1923 Fig. 13 Ratio of the O₄ dAMF obtained from simulated spectra for different surface
 1924 temperatures by the corresponding O₄ dAMFs derived from radiative transfer simulations.
 1925 The results represent MAX-DOAS observations at low elevation angles (2° to 3°).



1935 b) Spectra from other groups analysed by MPIC (all analyses for 335 – 374 nm)

1937
1938



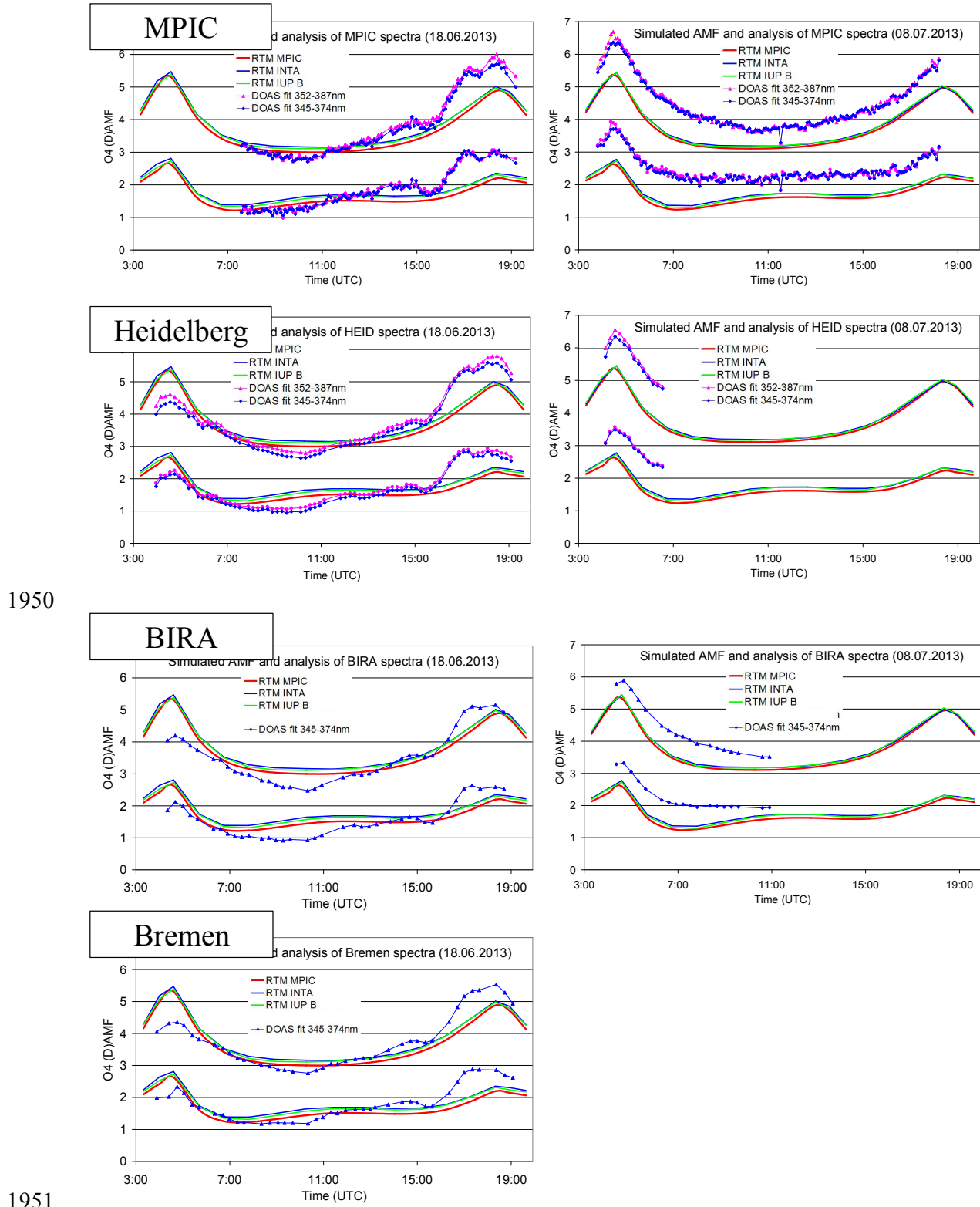
c) Spectra from other groups analysed by the same groups

1939
1940
1941
1942
1943
1944
1945
1946
1947
1948
1949

Fig. 14 a) Ratio of the O₄ (d)AMFs derived from MPIC spectra when analysed by other groups versus those analysed by MPIC for both selected days; b) Ratio of the O₄ (d)AMFs derived from spectra measured and analysed by other groups (using different wavelength ranges and settings) versus those for the MPIC instrument analysed by MPIC; c) Ratio of the O₄ (d)AMFs derived from spectra measured by other groups but analysed by MPIC versus those for the MPIC instrument analysed by MPIC (using the spectral range 335 – 374 nm for all instruments).

18 June 2013

8 July 2013



1950
1951
1952
1953
1954
1955
1956

Fig. 15 Comparison of measured and simulated O_4 (d)AMFs for both selected days. Measurements are from 4 different instruments, but analysed by MPIC using the standard settings (see Table 7). Simulations are performed by three different groups using Mie phase functions and otherwise the standard settings (see Table 6).

1957 **Appendix A1 Settings used for the simulation of synthetic spectra**

1958

1959

1960 Table A1 Vertical resolution used in radiative transfer simulations for different altitude
1961 ranges.

Lower boundary [km]	Upper boundary [km]	Vertical resolution [km]
0	0.5	0.02
0.5	2	0.1
2	12	0.2
12	25	1
25	45	2
45	100	5
100	1000	900

1962

1963

1964

1965

1966 Table A2 Dependence of SZA and relative azimuth angle on time (UTC) for the standard
1967 viewing direction (51° with respect to North).

Time (UTC)	SZA	RAZI
03:19	90	-0.1
04:00	85	7.7
04:36	80	14.2
05:42	70	26
06:44	60	37.5
07:48	50	50.1
08:54	40	66.2
10:16	30	94.6
11:26	26	129
12:40	30	163.3
14:02	40	191.8
15:09	50	207.9
16:11	60	220.5
17:14	70	232
18:20	80	243.8
18:56	85	250.3
19:38	90	258

1968

1969

1970

1971

1972

1973

1974

1975

1976

1977

1978

1979

1980 Table A3 Trace gas profiles and cross sections used for the simulation of the synthetic
 1981 spectra.

Trace gas	Vertical profile	Cross section (reference and T)
O ₄	Derived from temperature and pressure profiles during. 18.06.: average profiles 11:00 – 14:00 08.07.: average profiles 7:00 – 11:00	Thalman and Volkamer (2013) (203, 223, 253, 273, 293 K)*
HCHO	18.06.: 0-1000m, constant concentration of $2 \cdot 10^{11}$ molec/cm ³ (about 8 ppb) 08.07.: 0-1000m, constant concentration of $1 \cdot 10^{11}$ molec/cm ³ (about 4 ppb)	Meller and Moortgat (2000) (298 K)
NO ₂	Troposphere 18.06.: 0-500m, constant concentration of $4 \cdot 10^{11}$ molec/cm ³ (about 16 ppb) 08.07.: 0-500m, constant concentration of $2 \cdot 10^{11}$ molec/cm ³ (about 8 ppb) Stratosphere: Gaussian profile with maximum at 25 km, and FWHM of 16 km, VCD = $5 \cdot 10^{15}$ molec/cm ²	Vandaele et al. (1997) (220, 294 K)
O ₃	Troposphere (0-8km): constant concentration $6 \cdot 10^{11}$ molec/cm ³ (about 24 ppb) Stratosphere: Gaussian profile with maximum at 22 km, and FWHM of 15 km, VCD = 314 DU	Serdychenko et al. (2014) (193 – 293 K in steps of 10 K)**

1982 *The temperature dependence is either considered or a constant temperature of 293 K is
 1983 assumed (see text for details).

1984 **The temperature dependence was parameterised according to Paur and Bass (1984).

1985

1986

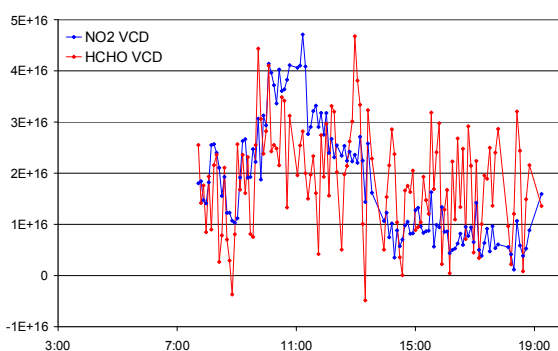
1987

1988

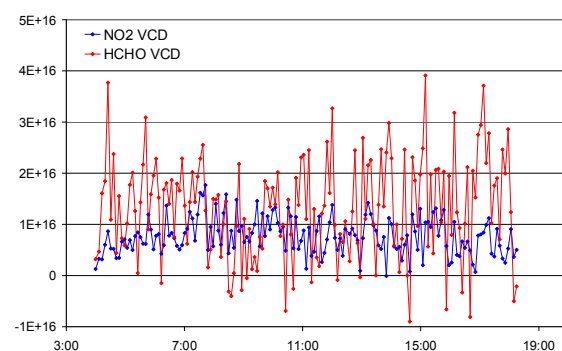
1989

1990

18 June 2013



8 July 2013



1991 Fig. A1 Tropospheric VCDs of NO₂ (blue) and HCHO (red) derived from measurements at
 1992 30° elevation using the geometric approximation.

1993

1994

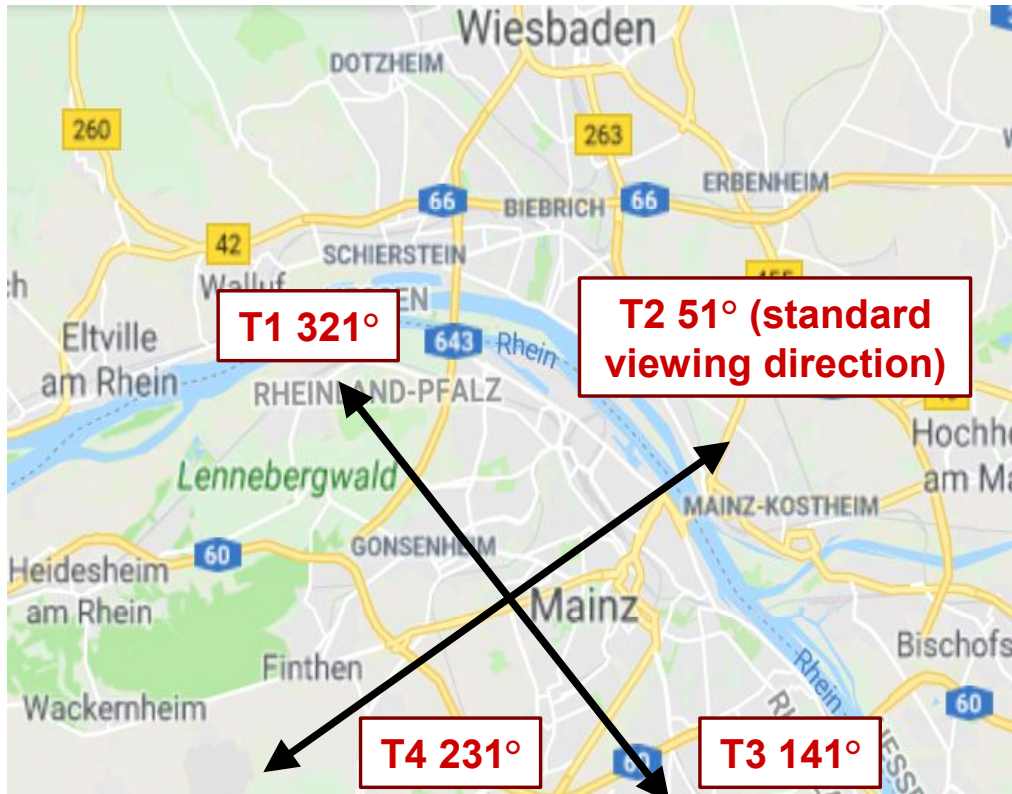
1995 **Appendix A2 Comparison of measured and simulated O₄ (d)AMFs for all azimuth and**
1996 **elevation angles of the MPIC MAX-DOAS measurements.**

1997

1998 The settings for the simulation of the synthetic spectra are given in Table 6 and Tables A1,
1999 A2, and A3 in appendix 1. Measurements are analysed using the standard settings (see Table
2000 7).

2001

2002



2003

2004 Fig. A2 Azimuth viewing directions of the 4 telescopes (T1 to T4) of the MPIC MAX-DOAS
2005 instrument. The azimuth angles are defined with respect to North (map: © google maps).

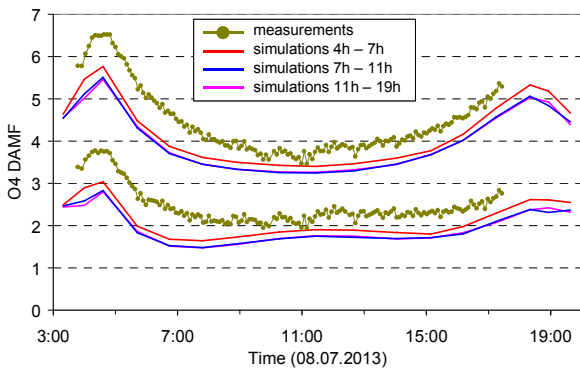
2006

2007

T1 North-West

For T1 and T4 azimuth direction, no measurements at 1° elevation were possible due to obstacles.

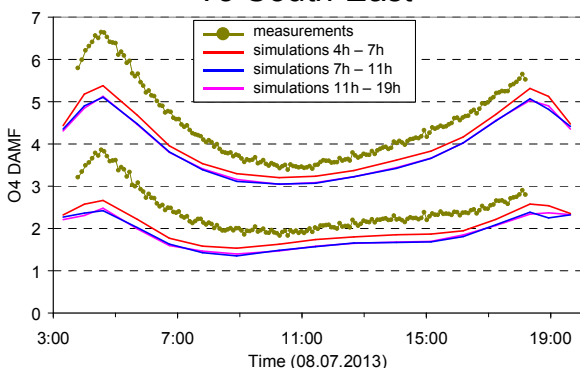
T2 North-East



T4 South-West

For T1 and T4 azimuth direction, no measurements at 1° elevation were possible due to obstacles.

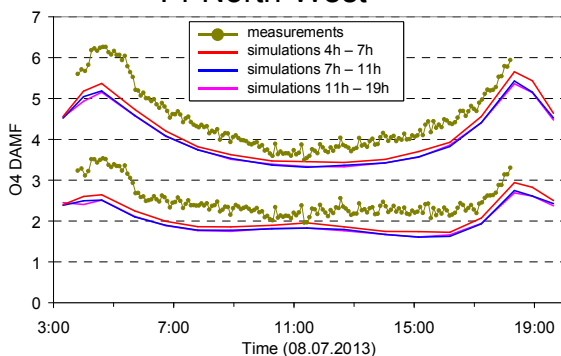
T3 South-East



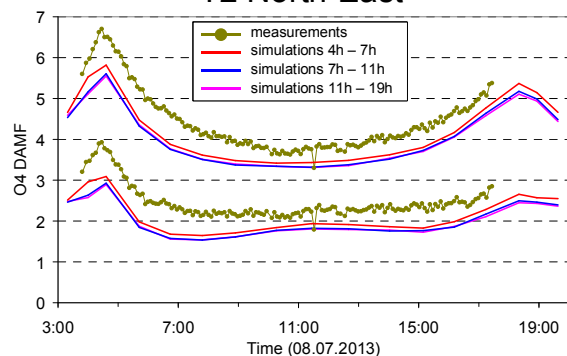
2008
2009
2010
2011

Fig. A3a Comparison results for 1° elevation angles on 8 July 2013. The upper lines indicate the O₄ AMFs, the lower lines the O₄ dAMFs (see also Fig. 2 and 3).

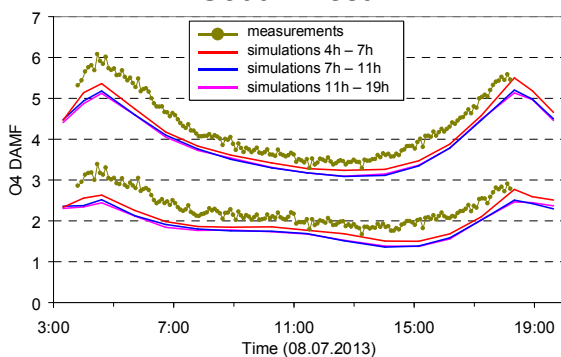
T1 North-West



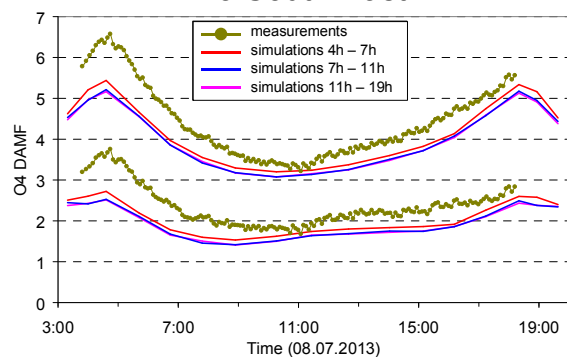
T2 North-East



T4 South-West



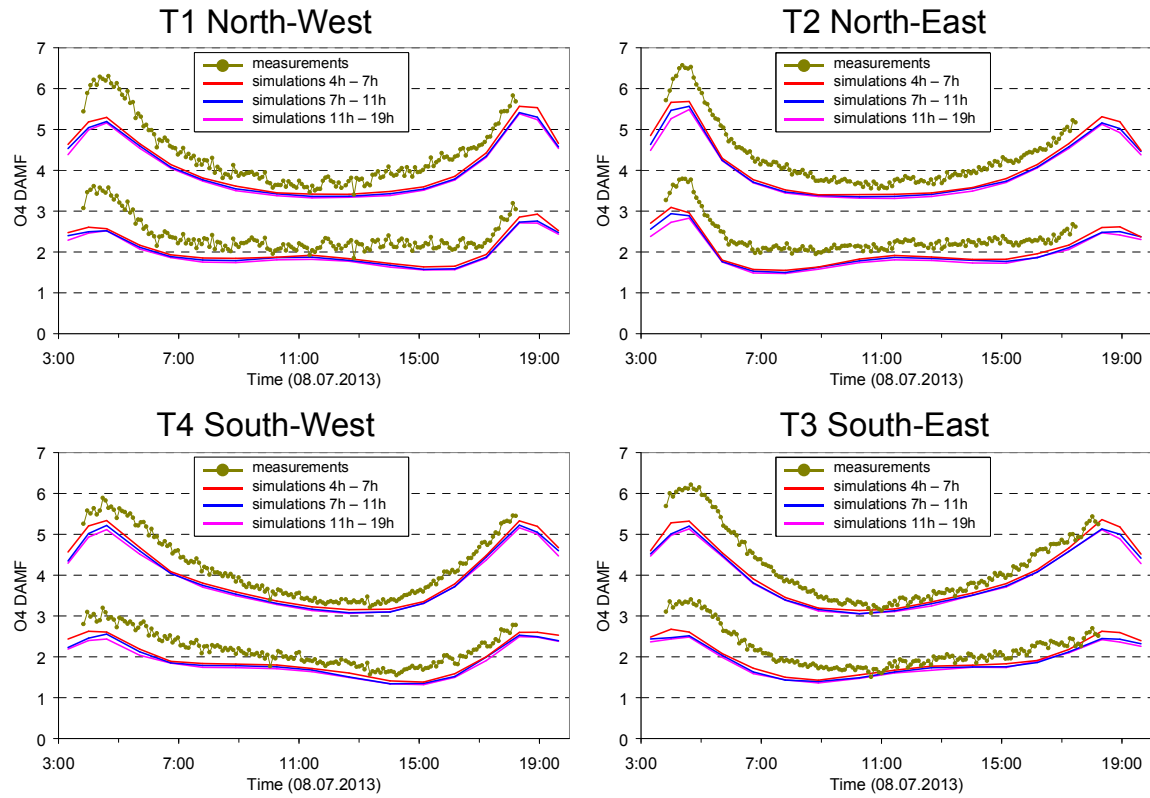
T3 South-East



2012
2013

Fig. A3b Comparison results for 3° elevation angles on 8 July 2013.

2014



2015

2016

2017

Fig. A3c Comparison results for 6° elevation angles on 8 July 2013.

2018

2019

2020

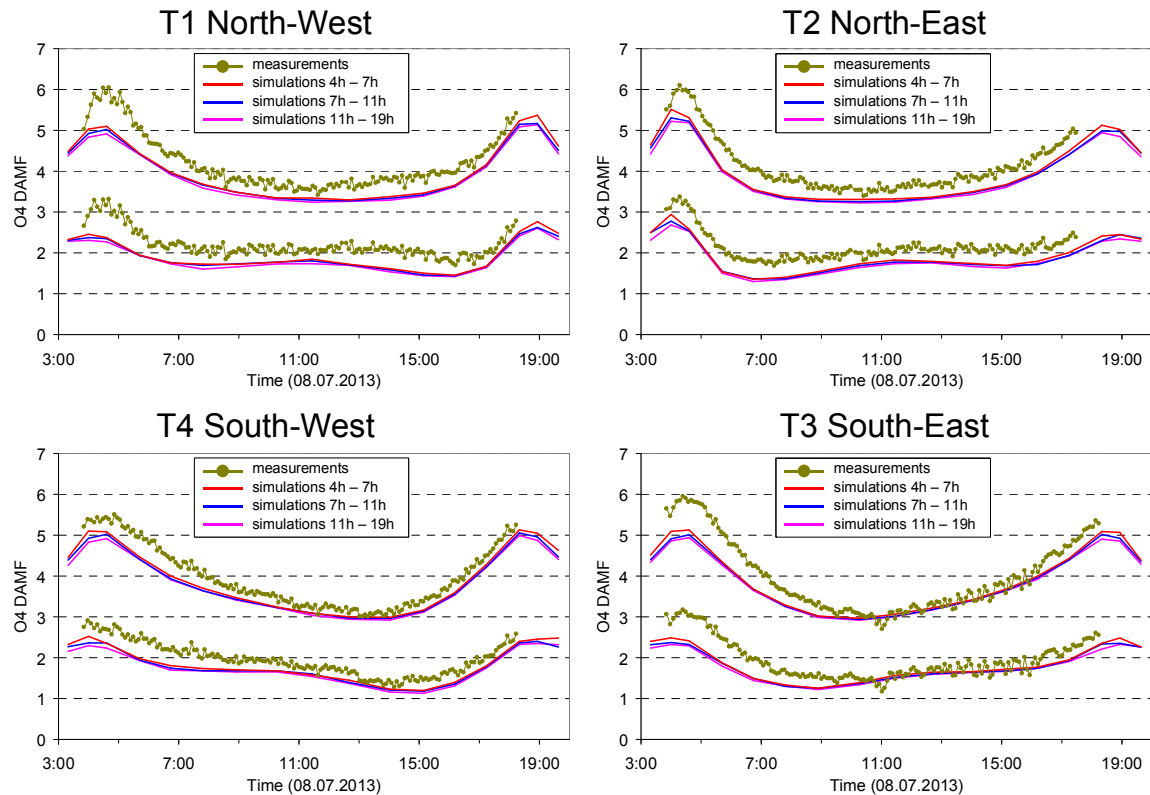


Fig. A3d Comparison results for 10° elevation angles on 8 July 2013.

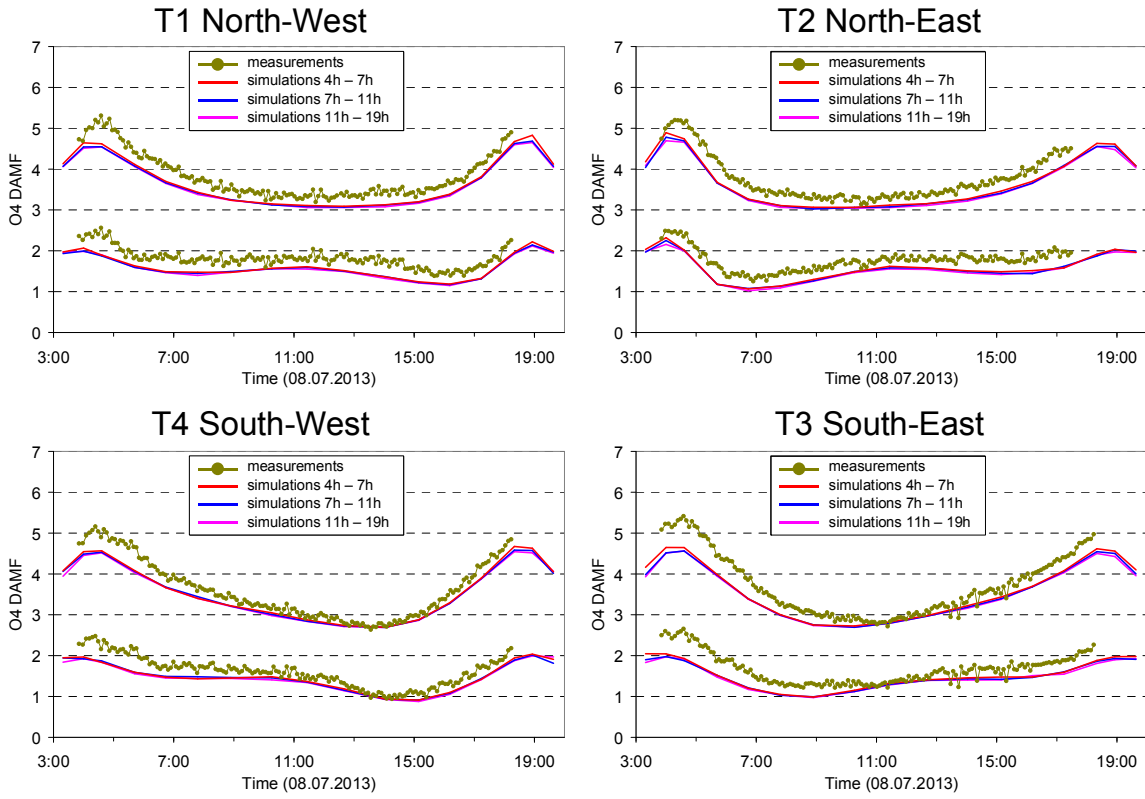


Fig. A3e Comparison results for 15° elevation angles on 8 July 2013.

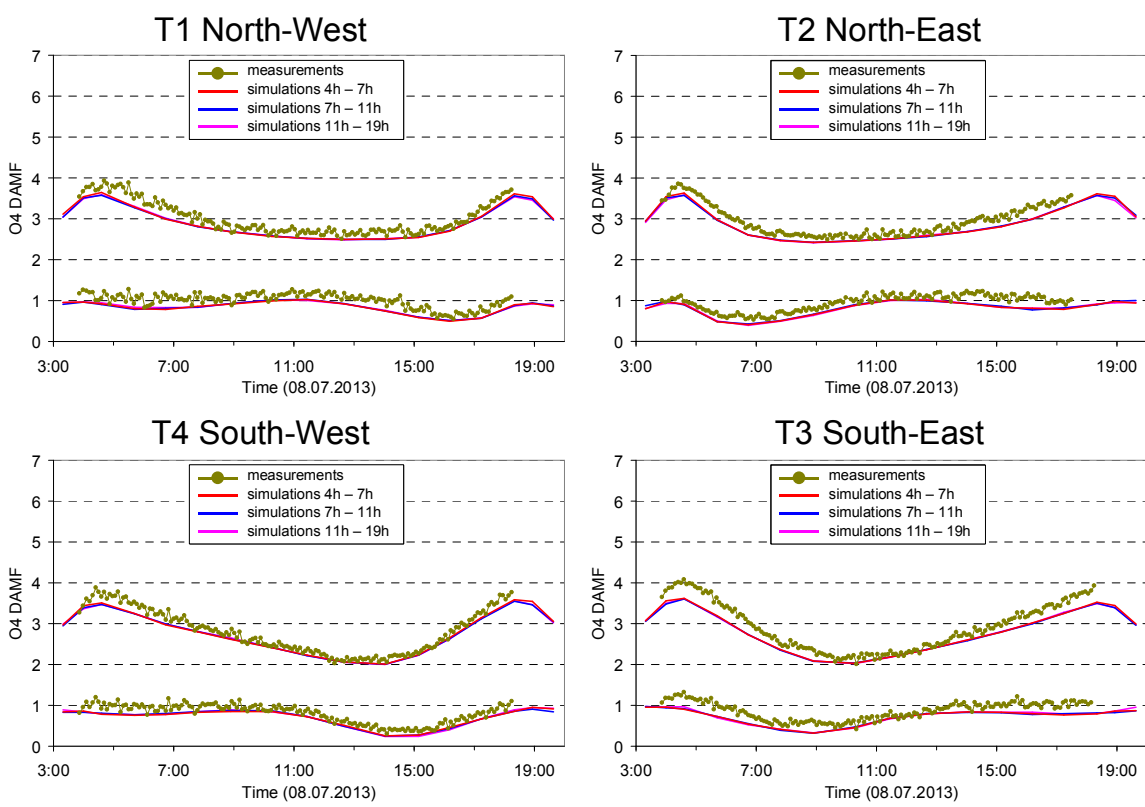
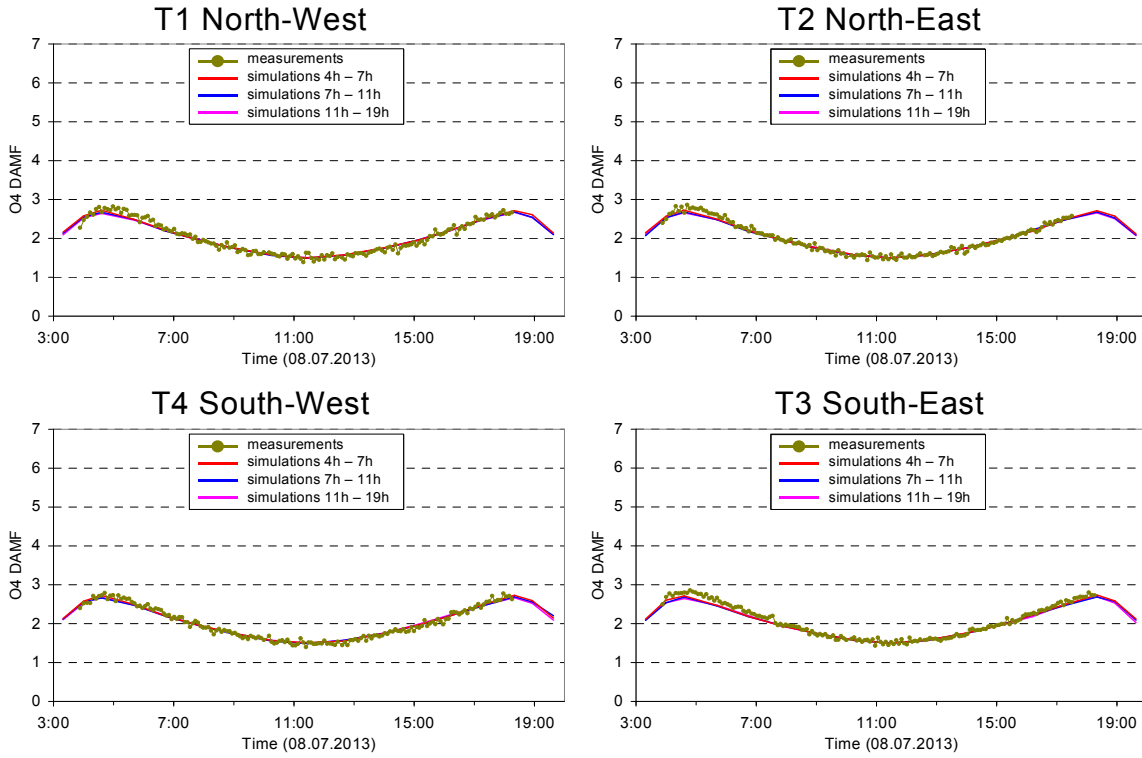


Fig. A3f Comparison results for 30° elevation angles on 8 July 2013.



2028
2029
2030

Fig. A3g Comparison results (only O₄ AMFs) for 90° elevation angles on 8 July 2013.

T1 North-West

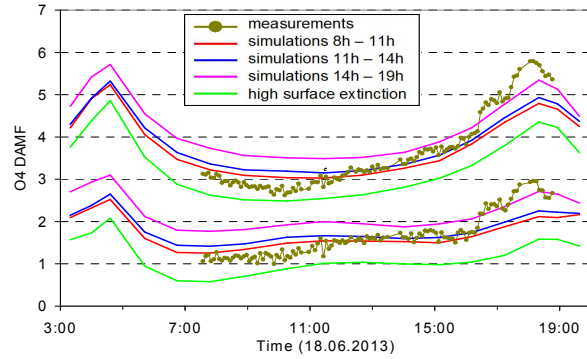
For T1 and T4 azimuth direction, no measurements at 1° elevation were possible due to obstacles.

In the following figures, the green lines indicate the results for the modified aerosol profile

T4 South-West

For T1 and T4 azimuth direction, no measurements at 1° elevation were possible due to obstacles.

T2 North-East



2031
2032
2033
2034

T3 South-East

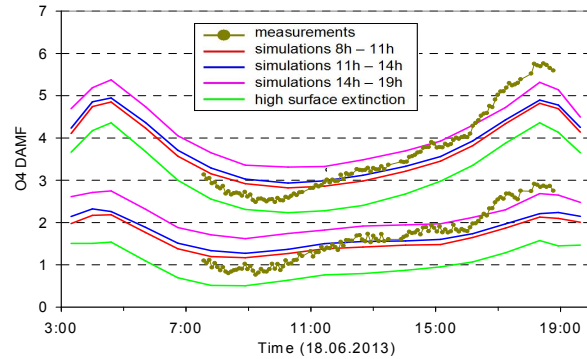
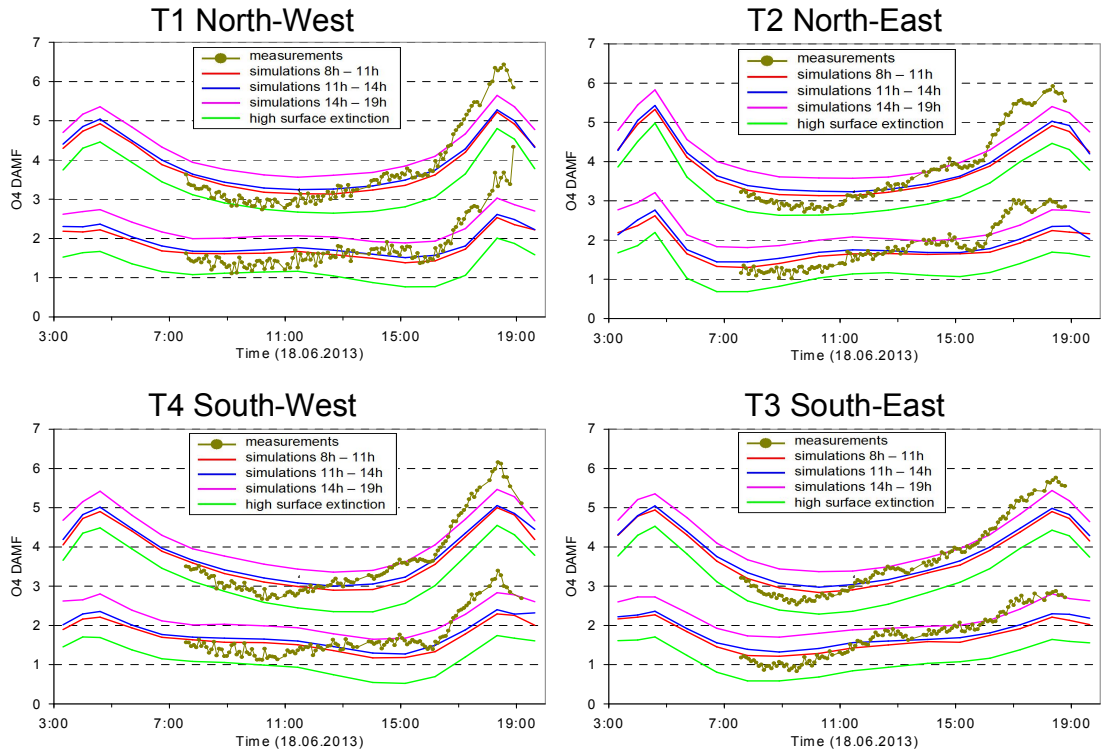
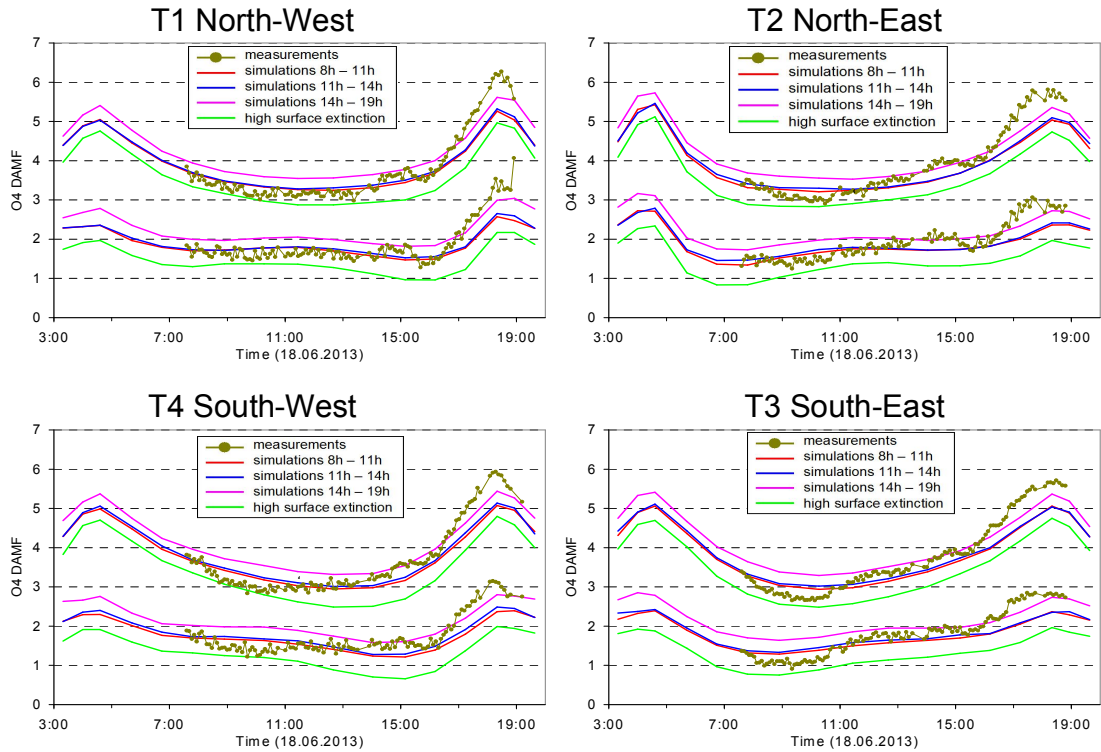


Fig. A4a Comparison results for 1° elevation angles on 18 June 2013 including the RTM results for the modified aerosol extinction profile (green line).



2038
2039
2040



2041
2042
2043
2044

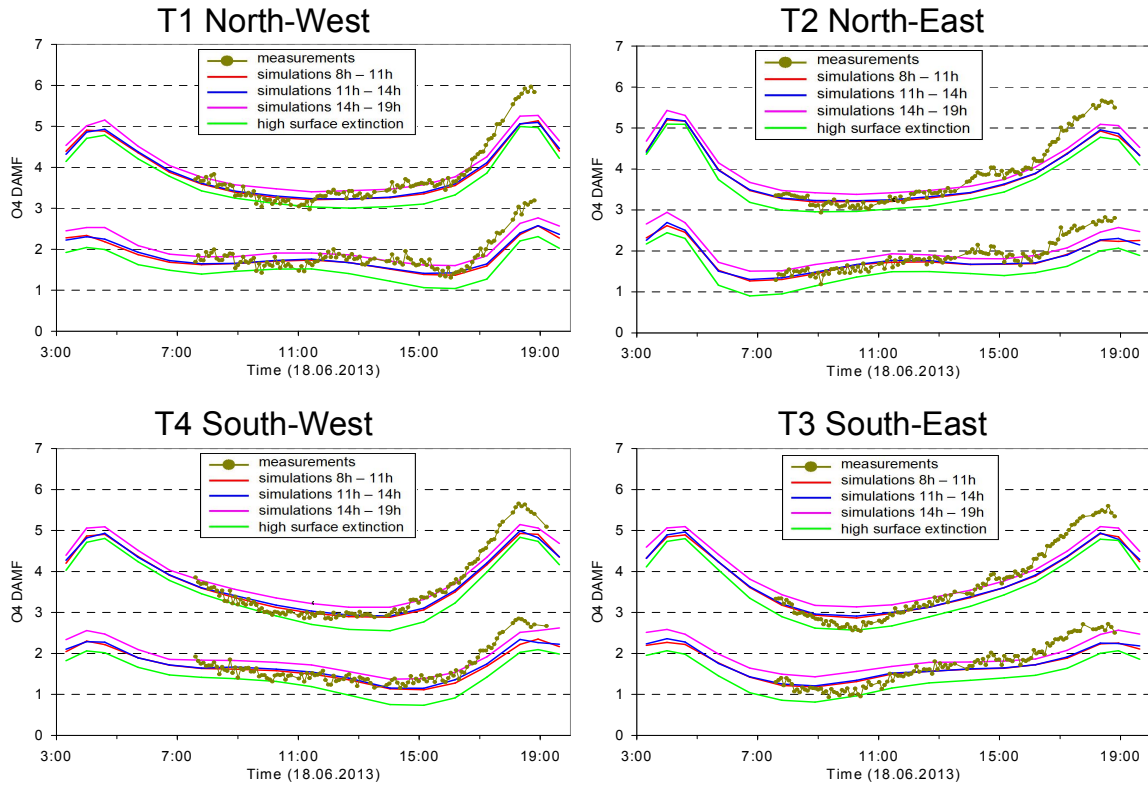


Fig. A4d Comparison results for 10° elevation angles on 18 June 2013 including the RTM results for the modified aerosol extinction profile (green line).

2045
2046
2047

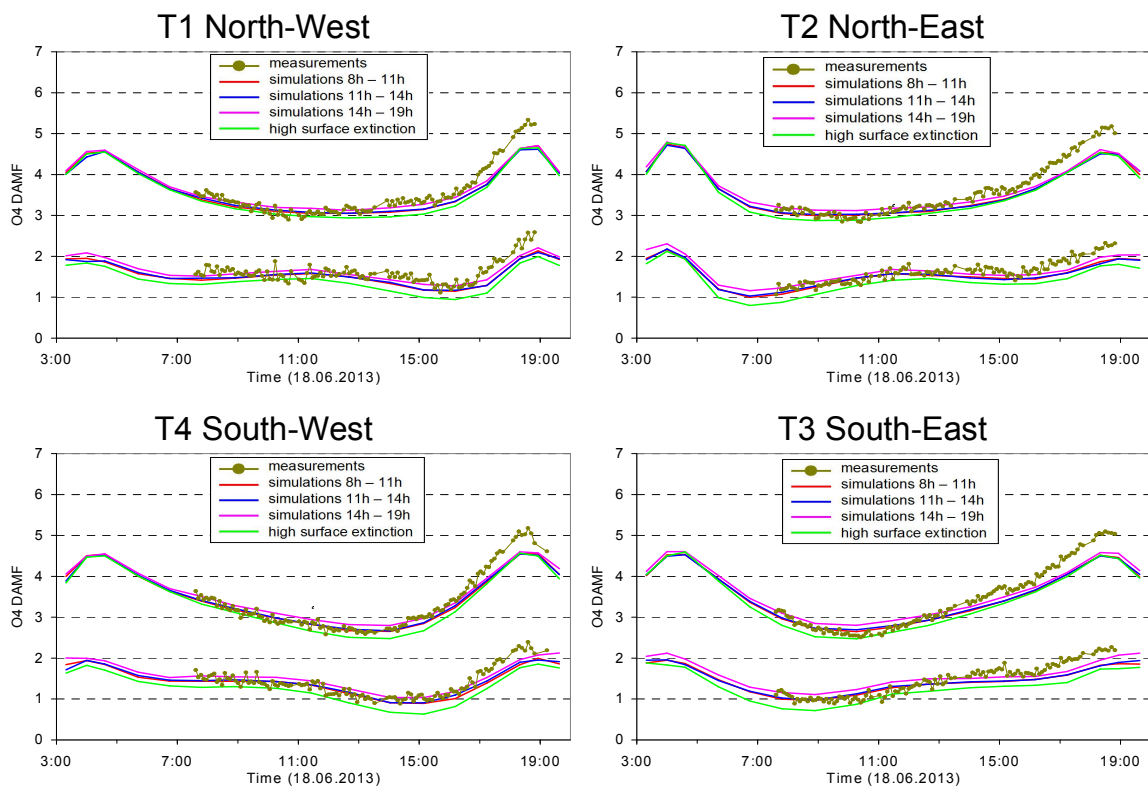


Fig. A4e Comparison results for 15° elevation angles on 18 June 2013 including the RTM results for the modified aerosol extinction profile (green line)..

2048
2049
2050
2051

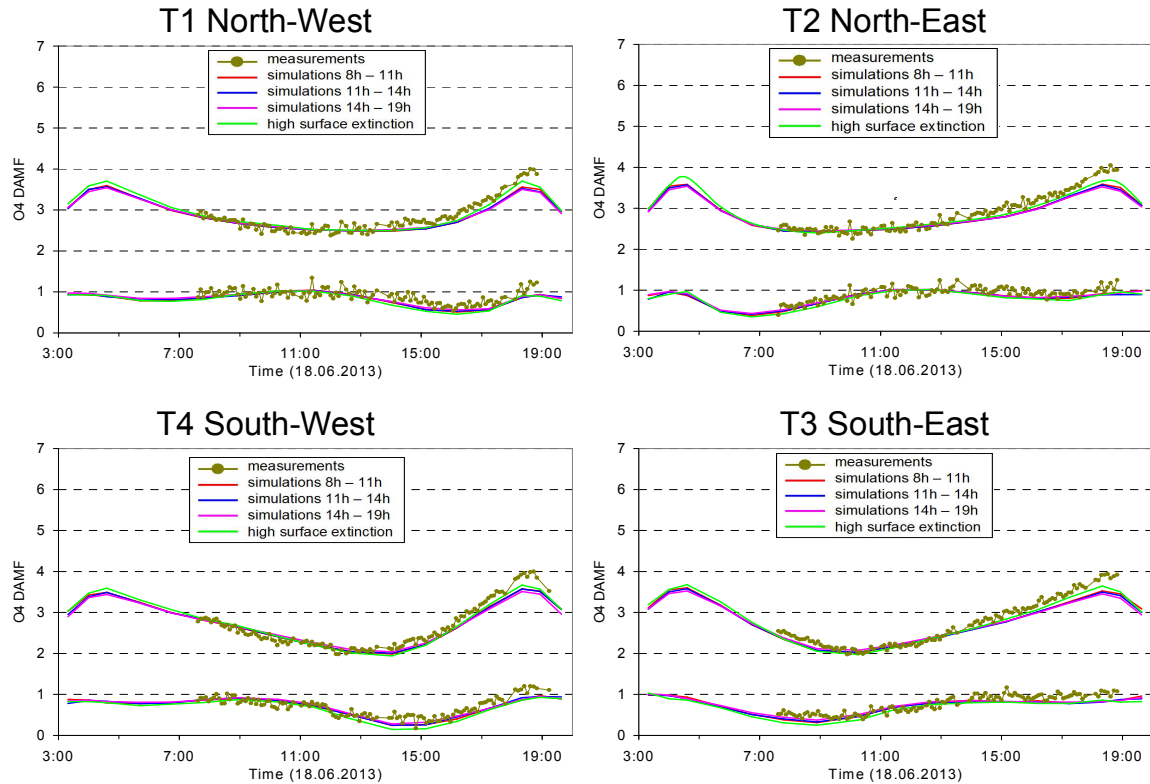


Fig. A4f Comparison results for 30° elevation angles on 18 June 2013 including the RTM results for the modified aerosol extinction profile (green line)..

2052
2053
2054

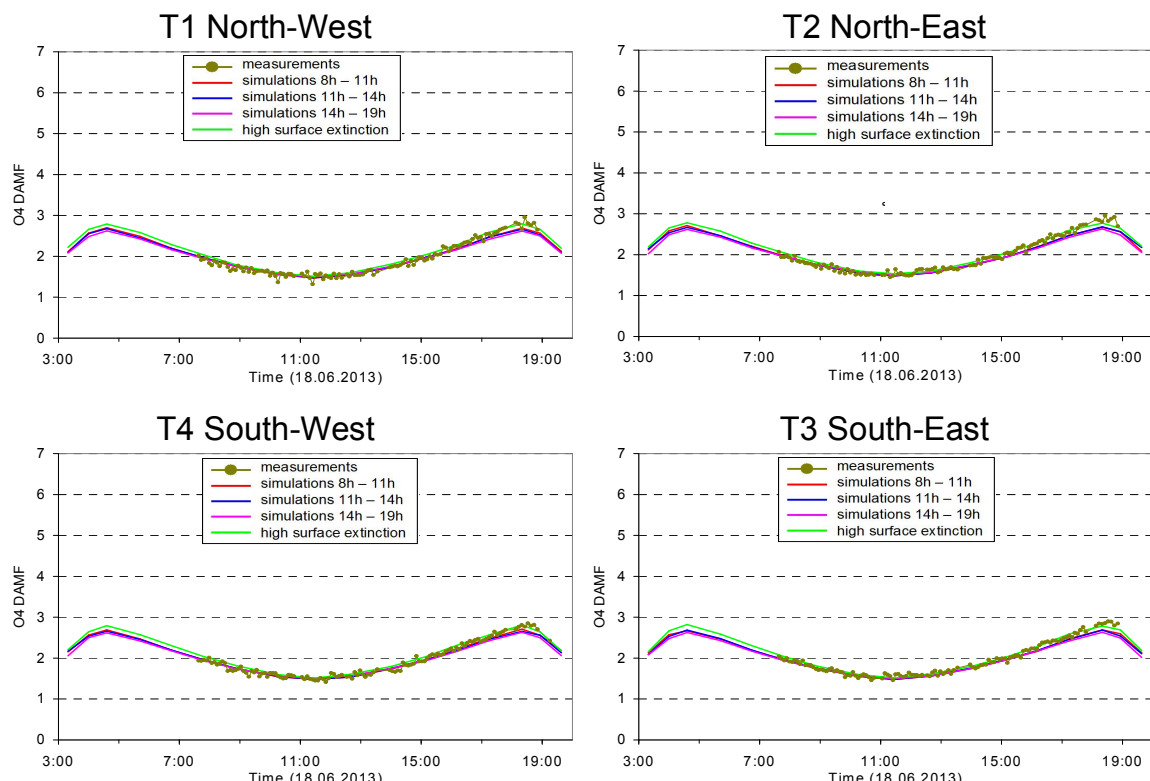


Fig. A4g Comparison results (only O₄ AMFs) for 90° elevation angles on 18 June 2013 including the RTM results for the modified aerosol extinction profile (green line).

2055 **Appendix A3 Comparison of the different procedures to extracted height profiles of**
2056 **temperature, pressure and O₄ concentration**

2058 **Extraction of temperature and pressure profiles**

2059
2060 For the two selected days during the MAD-CAT campaign two data sets of temperature and
2061 pressure are available: surface measurements close to the measurement site and vertical
2062 profiles from ECMWF ERA-Interim re-analysis data (see Table 5). Both data sets are used to
2063 derive the O₄ concentration profiles for the three selected periods on both days. The general
2064 procedure is that first the temperature profiles are determined. In a second step, the pressure
2065 profiles are derived from the temperature profiles and the measured surface pressure. For the
2066 temperature profile extraction, three height layers are treated differently:

2067 -below 1 km

2068 Between the surface (~150 m above sea level) and 1 km, the temperature is linearly
2069 interpolated between the average of the in situ measurements of the respective period and the
2070 ECMWF data at 1 km (see next paragraph). This procedure is used to account for the diurnal
2071 variation of the temperature close to the surface. Here it is important to note that for this
2072 surface-near layer the highest accuracy is required, because a) the maximum O₄ concentration
2073 is located near the surface, and b) the MAX-DOAS measurements are most sensitive close to
2074 the surface.

2075 -1 km to 20 km

2076 In this altitude range, the diurnal variation of the temperature becomes very small. Thus the
2077 average of the four ECMWF profiles of each day is used (for simplicity, a 6th order
2078 polynomial is fitted to the ECMWF data).

2079 -Above 20 km

2080 In this altitude range the accuracy of the temperature profile is not critical and thus the
2081 ECMWF temperature profile for 00:00 UTC of the respective day is used for simplicity.

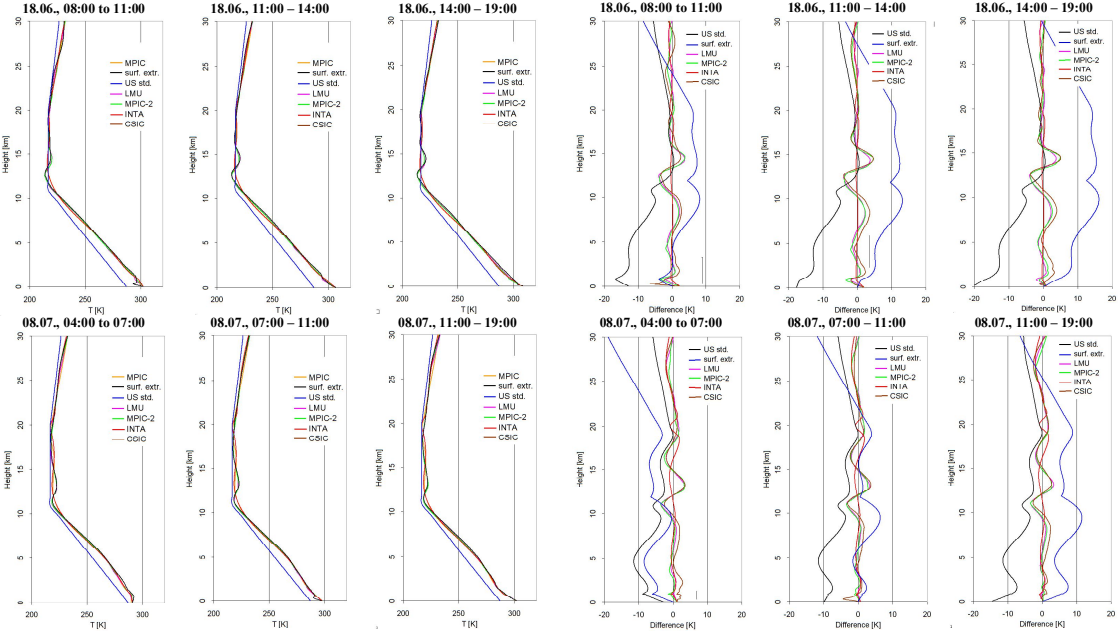
2082 The temperature profiles for 8 July 2013 extracted in this way are shown in Fig. 4 (left). Close
2083 to the surface the temperature variation during the day is about 10 K.

2084 In the next step, the pressure profiles are determined from the surface pressure (obtained from
2085 the in situ measurements) and the extracted temperature profiles according to the ideal gas
2086 law. In principle the effect of atmospheric humidity could also be taken into account, but the
2087 effect is very small for surface-near layers and is thus ignored here. The derived pressure
2088 profiles for 8 July 2013 are shown in Fig. 4 (right). Excellent agreement with the
2089 corresponding ECMWF pressure profiles is found.

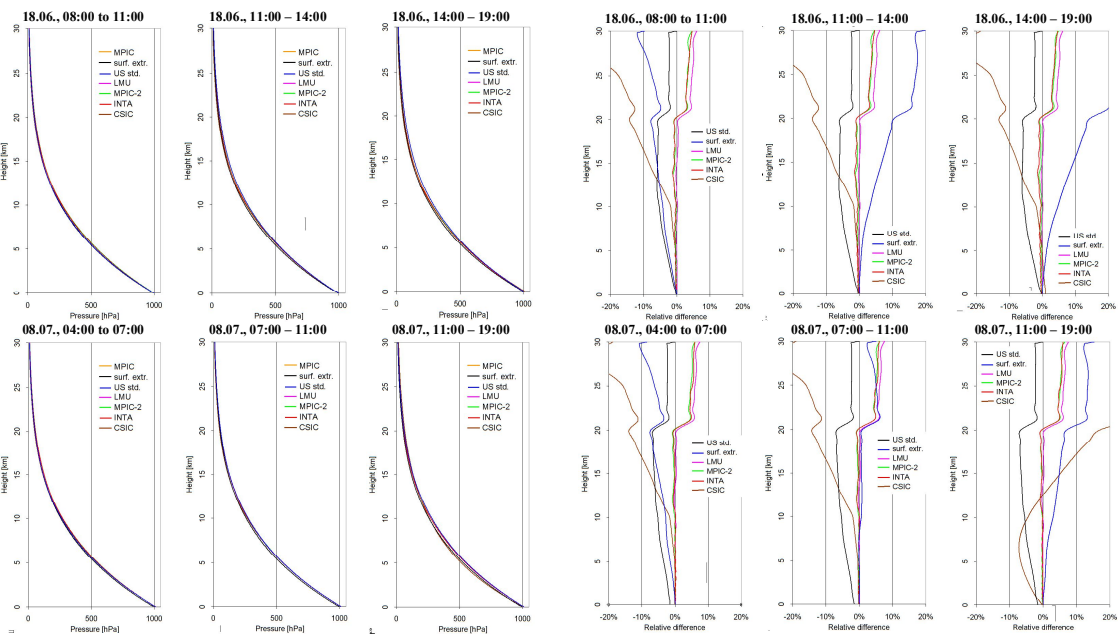
2090 Here it should be noted that in principle also the ECMWF pressure profiles could be used.
2091 However, we chose to determine the pressure profiles from the surface pressure and the
2092 extracted temperature profiles, because this procedure can also be applied if no ECMWF data
2093 (or other information on temperature and pressure profiles) is available.

2094 If no profile data (e.g. from ECMWF) are available, temperature and pressure profiles can
2095 also be extrapolated from surface measurements e.g. by assuming a constant lapse rate of
2096 -0.65 K / 100 m for the altitude range between the surface and 12 km, and a constant
2097 temperature above 12 km (as stated above, uncertainties at this altitude range have only a
2098 negligible effect on the O₄ VCD). If no measurements or model data are available at all, a
2099 fixed temperature and pressure profile can be used, e.g. the US standard atmosphere (United
2100 States Committee on Extension to the Standard Atmosphere, 1976).

2101



2102
2103 Fig. A5a Left: Comparison of temperature profiles extracted by the different groups (also
2104 shown are the profiles from the US standard atmosphere and the profiles extrapolated from
2105 the surface measurements). Right: Differences of these profiles compared to the MPIC
2106 standard extraction.
2107



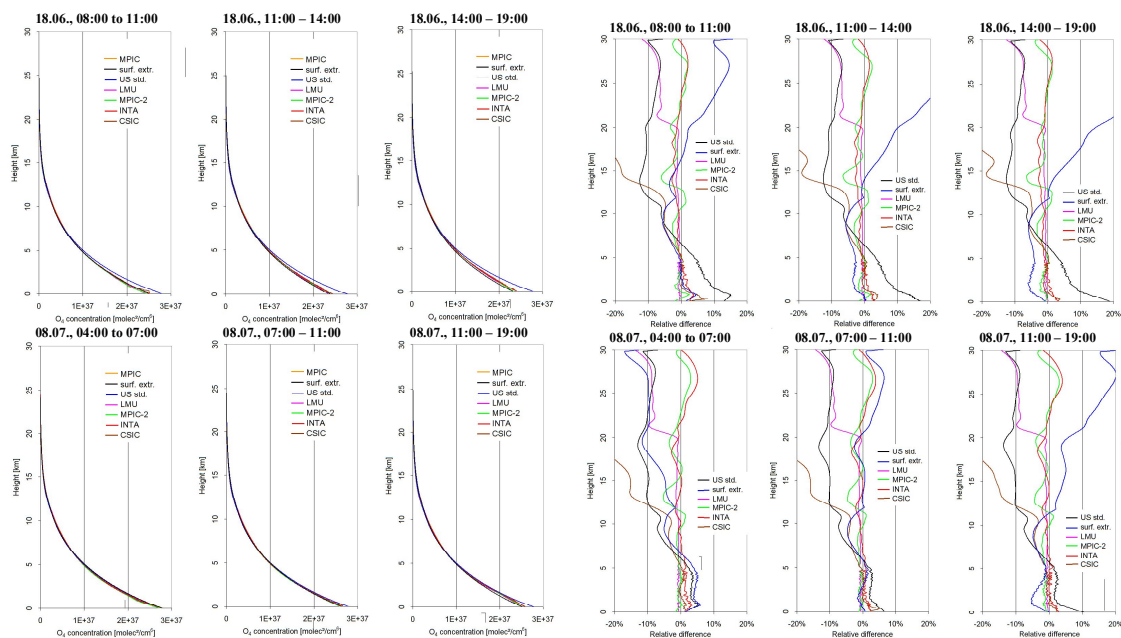
2108
2109 Fig. A5b Left: Comparison of pressure profiles extracted by the different groups (also shown
2110 are the profiles from the US standard atmosphere and the profiles extrapolated from the
2111 surface measurements). Right: Differences of these profiles compared to the MPIC standard
2112 extraction.
2113
2114
2115
2116
2117

2118 **Determination of the uncertainties of the O₄ profiles and O₄ VCDs caused by**
 2119 **uncertainties of the input parameters**
 2120

2121 The uncertainties of the O₄ profiles and O₄ VCDs are derived by varying the input parameters
 2122 according to their uncertainties. The following results are obtained:

2123 -The variation of the temperature (whole profile) by about 2K leads to variations of the O₄
 2124 concentration (or O₄ VCD) by about 0.8%.
 2125 -The variation of the surface pressure by about 3 hPa leads to variations of the O₄
 2126 concentration (or O₄ VCD) by about 0.7%.
 2127 -The effect of uncertainties of the relative humidity depends strongly on temperature: For
 2128 surface temperatures of 0°C, 10°C, 20°C, 30°C, and 35°C a variation of the relative humidity
 2129 of 30% leads to variations of the O₄ concentration (or O₄ VCDs) of about 0.15%, 0.3%, 0.6%,
 2130 1.2%, and 1.6%, respectively. If the effect of atmospheric humidity is completely ignored (dry
 2131 air is assumed), the resulting O₄ concentrations (or O₄ VCDs) are systematically
 2132 overestimated by about 0.3%, 0.7%, 1.3%, 2.5%, and 4% for surface temperatures of 0°C,
 2133 10°C, 20°C, 30°C, and 35°C, respectively (assuming a relative humidity of 70%). In this
 2134 study we used the relative humidity measured by the in situ sensors. We took these values not
 2135 only for the surface layers, but also for the whole troposphere. Here it should be noted that the
 2136 related uncertainties of the absolute humidity decrease quickly with altitude because the
 2137 absolute humidity itself decreases quickly with altitude. Since both selected days were warm
 2138 or even hot summer days, we estimate the uncertainty of the O₄ concentration and O₄ VCDs
 2139 due to uncertainties of the relative humidity to 1% and 0.4% on 18 June and 8 July,
 2140 respectively.

2141 Assuming that the uncertainties of the three input parameters are independent, the total
 2142 uncertainty related to these parameters is estimated to be about 1.5%.
 2143

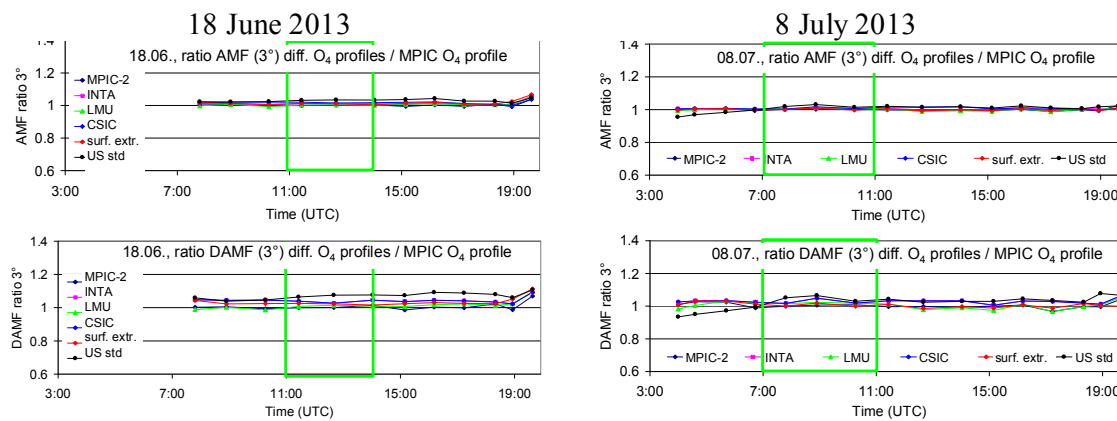


2144 Fig. A5c Left: Comparison of O₄ concentration profiles extracted by the different groups (also
 2145 shown are the profiles from the US standard atmosphere and the profiles extrapolated from
 2146 the surface measurements). Right: Differences of these profiles compared to the MPIC
 2147 standard extraction.
 2148

2149
 2150
 2151

2152
2153
2154
2155
2156
2157
2158
2159
2160
2161
2162
2163
2164
2165
2166
2167
2168
2169
2170
2171
2172
2173
2174
2175
2176

Appendix A4 Results of the sensitivity studies of simulated and measured O₄ (d)MFs

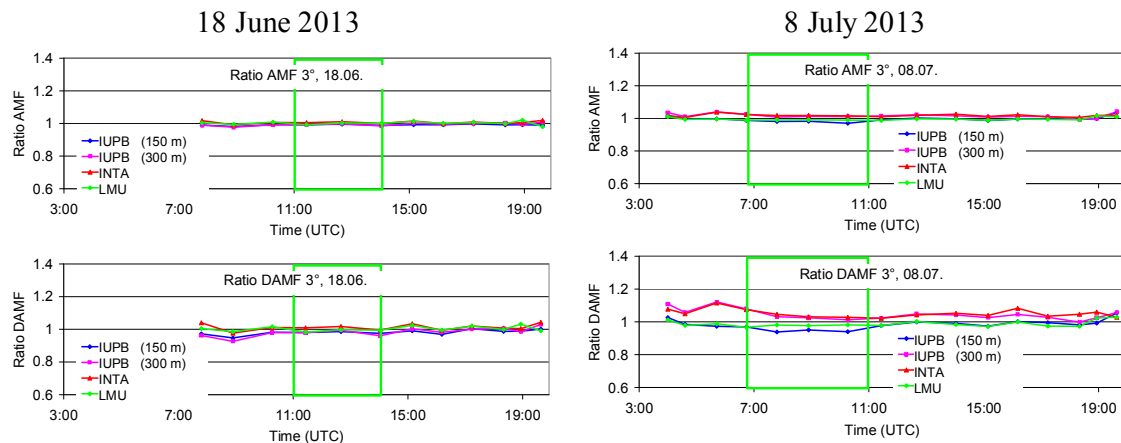


2177
2178 Fig. A6 Ratio of the O₄ AMFs (top) and O₄ dAMFs (bottom) derived for different O₄ profiles
2179 versus the standard O₄ profile (MPIC) for both selected days. Besides the O₄ profiles
2180 extracted by the different groups, also the O₄ profiles derived from the US standard
2181 atmosphere and for the extrapolation of the surface values are included.
2182
2183
2184
2185
2186
2187
2188

2189 Table A4 Average ratios of O₄ (d)AMFs simulated for different O₄ profiles versus the results
 2190 for the standard settings (using the MPIC O₄ profiles) for the two middle periods on both
 2191 selected days.

O ₄ profile extraction	AMF ratios		dAMF ratios	
	18 June 2013, 11:00 – 14:00	8 July 2013, 7:00 – 11:00	18 June 2013, 11:00 – 14:00	8 July 2013, 7:00 – 11:00
MPIC-2	1.00	1.00	1.00	1.00
INTA	1.01	1.01	1.02	1.01
LMU	1.00	1.00	1.01	1.02
CSIC	1.02	1.01	1.04	1.02
Lapse rate	1.01	1.00	1.02	1.01
US std. atm.	1.03	1.02	1.07	1.04

2192
 2193
 2194
 2195
 2196
 2197
 2198
 2199
 2200



2201 Fig. A7 Ratio of the O₄ AMFs (top) and O₄ dAMFs (bottom) derived for aerosol extinction
 2202 profiles extracted by different groups versus the standard aerosol extinction profiles (MPIC)
 2203 for both selected days.

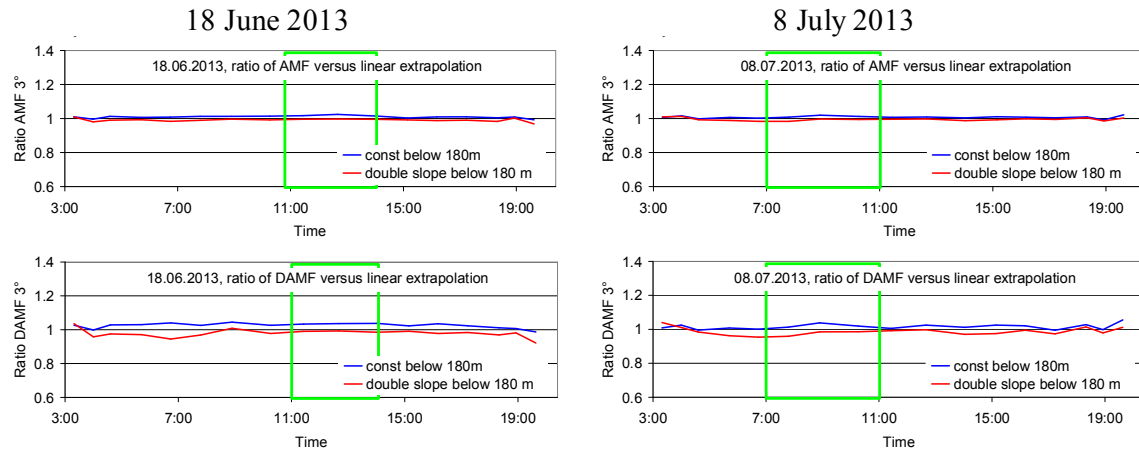
2204
 2205

2206 Table A5 Average ratios of O₄ (d)AMFs simulated for different aerosol extinction profiles
 2207 versus the results for the standard settings (using the MPIC aerosol extinction profiles) for the
 2208 two middle periods on both selected days.

Aerosol profile extraction	AMF ratios		dAMF ratios	
	18 June 2013, 11:00 – 14:00	8 July 2013, 7:00 – 11:00	18 June 2013, 11:00 – 14:00	8 July 2013, 7:00 – 11:00
INTA	1.01	1.02	1.01	1.04

IUP-B 150 m	0.99	0.98		0.98	0.96
IUP-B 300 m	0.99	1.01		0.98	1.03
LMU	1.00	0.99		0.99	0.98

2209
2210



2211

2212 Fig. A8 Ratio of the O_4 AMFs (top) and O_4 dAMFs (bottom) derived for different
2213 extrapolations of the aerosol extinction profiles below 180 m versus those for the standard
2214 settings (linearly extrapolated profiles) for both selected days.

2215

2216

2217

2218 Table A6 Average ratios of O_4 (d)AMFs simulated for aerosol extinction profiles with
2219 different extrapolations below 180 m versus the results for the standard settings (linear
2220 extrapolation) for the two middle periods on both selected days.

	AMF ratios		dAMF ratios		
Extrapolation below 180 m	18 June 2013, 11:00 – 14:00	8 July 2013, 7:00 – 11:00		18 June 2013, 11:00 – 14:00	8 July 2013, 7:00 – 11:00
Constant extinction	1.02	1.01		1.04	1.02
Double slope	1.00	0.99		0.99	0.98

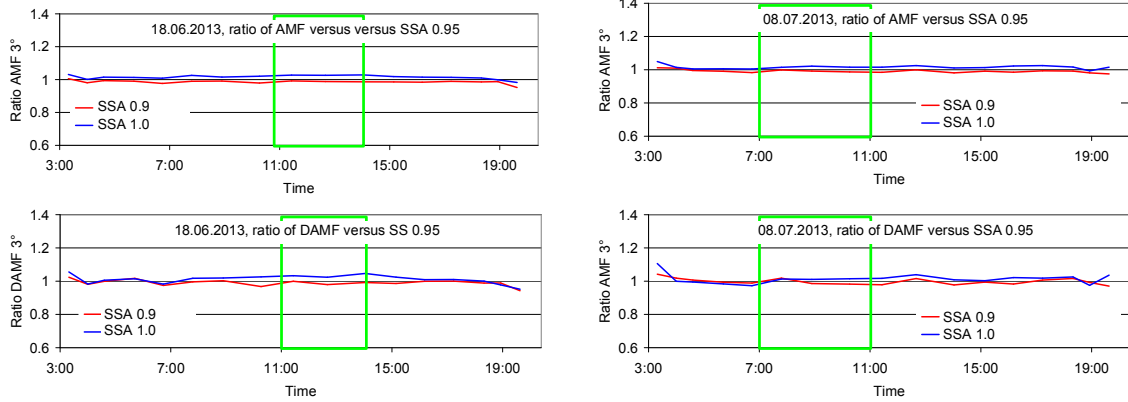
2221

2222

2223

18 June 2013

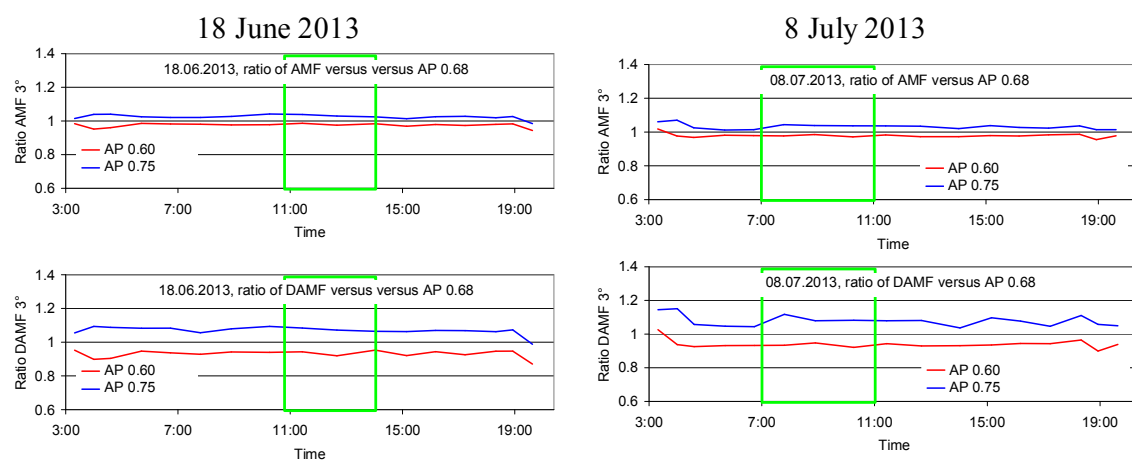
8 July 2013



2224
2225 Fig. A9 Ratio of the O_4 AMFs (top) and O_4 dAMFs (bottom) derived for different aerosol
2226 single scattering albedos versus those for the standard settings (single scattering albedo of
2227 0.95) for both selected days.

2228
2229
2230
2231
2232 Table A7 Average ratios of O_4 (d)AMFs simulated for different aerosol single scattering
2233 albedos (SSA) versus the results for the standard settings (single scattering albedo of 0.95) for
2234 the two middle periods on both selected days.

	AMF ratios			dAMF ratios	
Single scattering albedo	18 June 2013, 11:00 – 14:00	8 July 2013, 7:00 – 11:00		18 June 2013, 11:00 – 14:00	8 July 2013, 7:00 – 11:00
0.9	0.99	0.99		0.99	0.99
1.0	1.03	1.01		1.03	1.01



2242 Fig. A10 Ratio of the O₄ AMFs (top) and O₄ dAMFs (bottom) derived for different aerosol
 2243 phase functions (HG-parameterisation with different asymmetry parameters) versus those for
 2244 the standard settings (asymmetry parameter of 0.68) for both selected days.

2245

2246

2247

2248

2249 Table A8 Average ratios of O₄ (d)AMFs simulated for different aerosol phase functions (HG-
 2250 parameterisation with different asymmetry parameters (AP) versus the results for the standard
 2251 settings (asymmetry parameter of 0.68) for the two middle periods on both selected days.

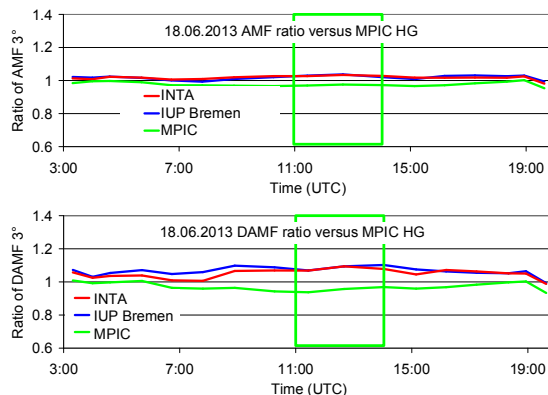
Asymmetry parameter	AMF ratios		dAMF ratios	
	18 June 2013, 11:00 – 14:00	8 July 2013, 7:00 – 11:00	18 June 2013, 11:00 – 14:00	8 July 2013, 7:00 – 11:00
0.6	0.98	0.98	0.94	0.94
0.75	1.03	1.03	1.08	1.07

2252

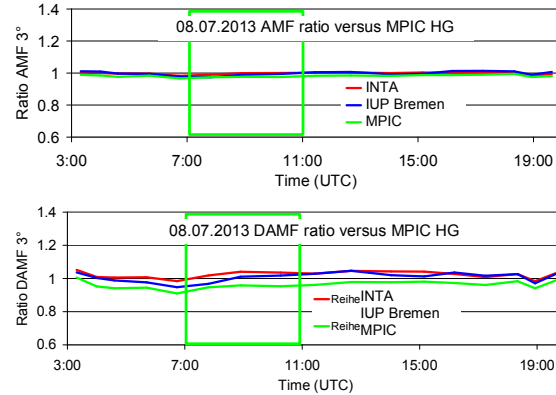
2253

2254

18 June 2013



8 July 2013



2255 Fig. A11 Ratio of the O₄ AMFs (top) and O₄ dAMFs (bottom) simulated by INTA and IUP-
 2256 Bremen and MPIC (SCIATRAN) for phase functions derived from the sun photometer
 2257 measurements versus those simulated by MPIC using the Henyey Greenstein phase function
 2258 for asymmetry parameter of 0.68 for both selected days.

2259

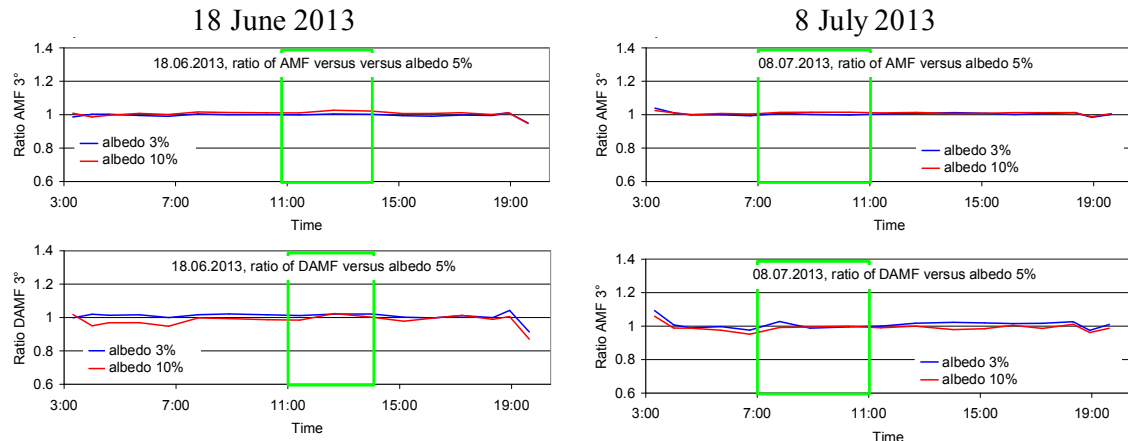
2260

2261 Table A9 Average ratios of O₄ (d)AMFs simulated by INTA and IUP-Bremen and MPIC
 2262 (SCIATRAN) for phase functions derived from the sun photometer measurements versus
 2263 those simulated by MPIC using the Henyey Greenstein phase function for asymmetry
 2264 parameter of 0.68 for the two middle periods on both selected days.

Group (RTM)	AMF ratios		dAMF ratios	
	18 June 2013, 11:00 – 14:00	8 July 2013, 7:00 – 11:00	18 June 2013, 11:00 – 14:00	8 July 2013, 7:00 – 11:00
INTA (LIDORT)	1.03	1.00	1.09	1.02
IUP-Bremen (SCIATRAN)	1.03	0.99	1.08	0.99
MPIC	0.97	0.98	0.95	0.95

(SCIATRAN)					
------------	--	--	--	--	--

2265
2266
2267



2268
2269 Fig. A12 Ratio of the O₄ AMFs (top) and O₄ dAMFs (bottom) for different surface albedos
2270 versus those for an albedo of 5 % for both selected days.
2271
2272
2273
2274
2275

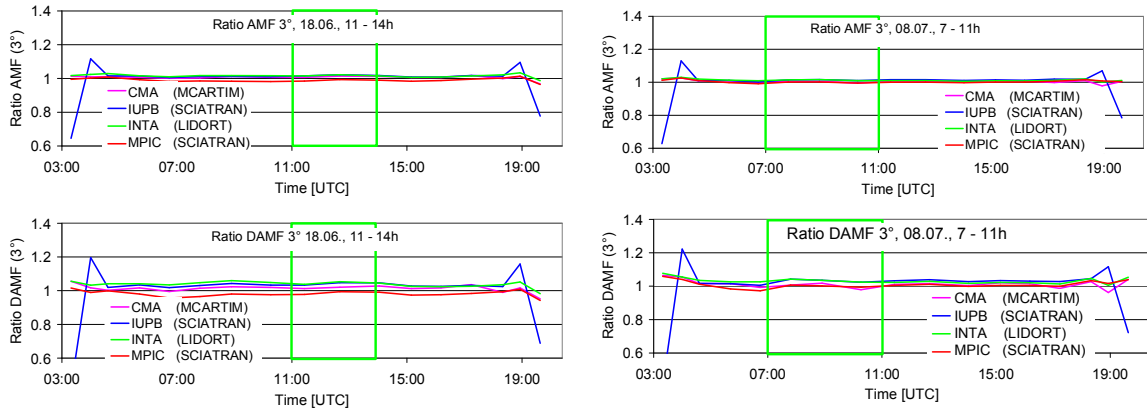
2276 Table A12–A10 Average ratios of O₄ (d)AMFs for different surface albedos versus those for
2277 an albedo of 5 % for the two middle periods on both selected days.

	AMF ratios			dAMF ratios	
	18 June 2013, 11:00 – 14:00	8 July 2013, 7:00 – 11:00		18 June 2013, 11:00 – 14:00	8 July 2013, 7:00 – 11:00
3 %	1.00	1.00		1.02	1.00
10 %	1.02	1.01		1.00	0.99

2278
2279
2280
2281
2282
2283
2284

18 June 2013

8 July 2013



2285
 2286 Fig. A13 Ratio of the O_4 AMFs (top) and O_4 dAMFs (bottom) simulated by different groups
 2287 using different radiative transfer models versus those for the MPIC simulations using
 2288 MCARTIM for both selected days.

2289

2290

2291

2292

2293 Table A11 Average ratios of O_4 (d)AMFs simulated by different groups using different
 2294 radiative transfer models versus those for the MPIC simulations using MCARTIM for the two
 2295 middle periods on both selected days.

Group (RTM)	AMF ratios		dAMF ratios	
	18 June 2013, 11:00 – 14:00	8 July 2013, 7:00 – 11:00	18 June 2013, 11:00 – 14:00	8 July 2013, 7:00 – 11:00
CMA (MACARTIM)	1.01	1.00	1.02	1.00
IUP-Bremen (SCIATRAN)	1.02	1.01	1.04	1.03
INTA (LIDORT)	1.02	1.01	1.05	1.03
MPIC (SCIATRAN)	0.99	1.00	0.99	1.00

2296

2297

2298

2299

2300

2301

2302

2303

2304

2305

2306

2307

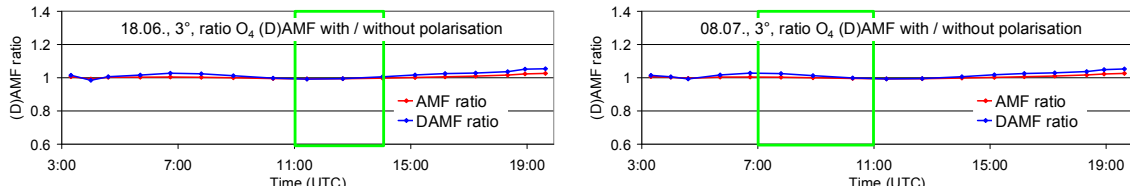
2308

2309

2310

18 June 2013

8 July 2013



2311
 2312 Fig. A14 Ratio of the O_4 (d)AMFs considering polarisation versus those without considering
 2313 polarisation for both selected days.

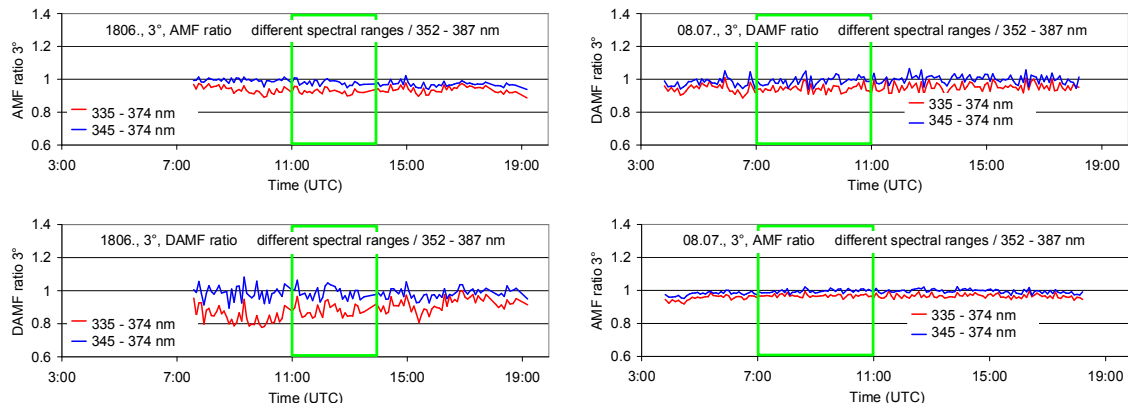
2314
 2315
 2316
 2317 Table A12 Average ratios of O_4 (d)AMFs considering polarisation versus those without
 2318 considering polarisation for the two middle periods on both selected days.

	AMF ratios		dAMF ratios	
	18 June 2013, 11:00 – 14:00	8 July 2013, 7:00 – 11:00	18 June 2013, 11:00 – 14:00	8 July 2013, 7:00 – 11:00
Considering polarisation	1.00	1.00	1.00	1.01

2319
 2320
 2321
 2322
 2323
 2324
 2325 Table A13 Average ratios of O_4 (d)AMFs derived from synthetic spectra versus those
 2326 obtained from radiative transfer simulations at 360 nm for the two middle periods on both
 2327 selected days.

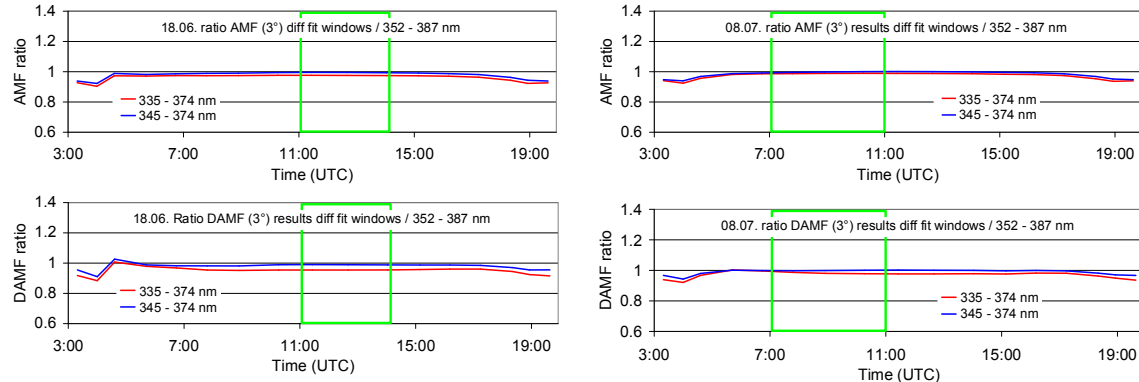
	AMF ratios		dAMF ratios	
Temperature dependence / noise	18 June 2013, 11:00 – 14:00	8 July 2013, 7:00 – 11:00	18 June 2013, 11:00 – 14:00	8 July 2013, 7:00 – 11:00
T dep. considered / no noise	1.01	1.02	1.01	1.00
no T dep. considered / no noise	1.00	1.01	1.00	1.00
no T dep. considered / noise	0.99	1.00	1.00	1.01

2336 a) measured spectra



2337
2338

b) synthetic spectra



2339
2340
2341
2342
2343

2344
2345
2346
2347
2348
2349

Fig. A15 Ratio of the O_4 (d)AMFs derived for different fit windows versus those for the standard fit window (352 – 387 nm) for both selected days (top: results for spectra measured by the MPIC instrument; bottom: results for synthetic spectra taking into account the temperature dependence of the O_4 cross section).

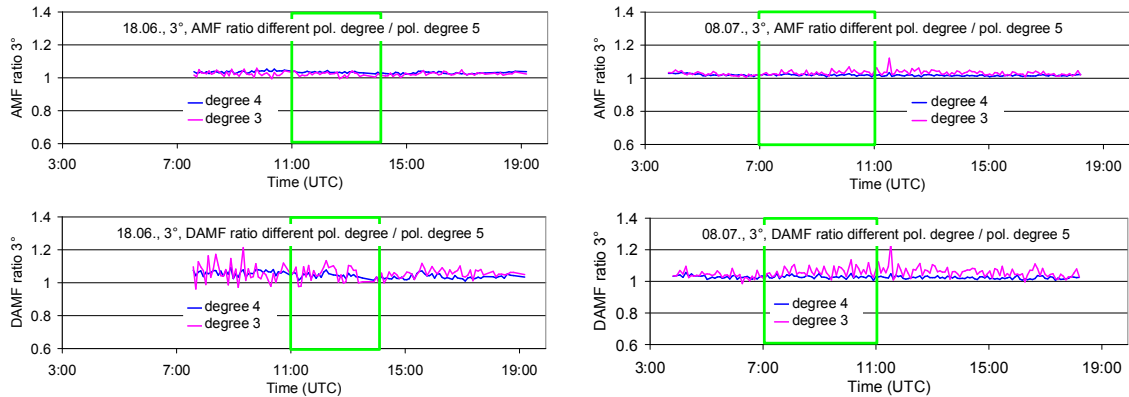
	AMF ratios		dAMF ratios		
Spectral range	18 June 2013, 11:00 – 14:00	8 July 2013, 7:00 – 11:00		18 June 2013, 11:00 – 14:00	8 July 2013, 7:00 – 11:00
Measured Spectra					
335 – 374 nm	0.93	0.97		0.88	0.94
345 – 374 nm	0.98	1.00		0.99	0.99
Synthetic Spectra					
335 – 374 nm	0.98	0.99		0.95	0.98
345 – 374 nm	0.99	1.00		0.99	1.00

2350

18 June 2013

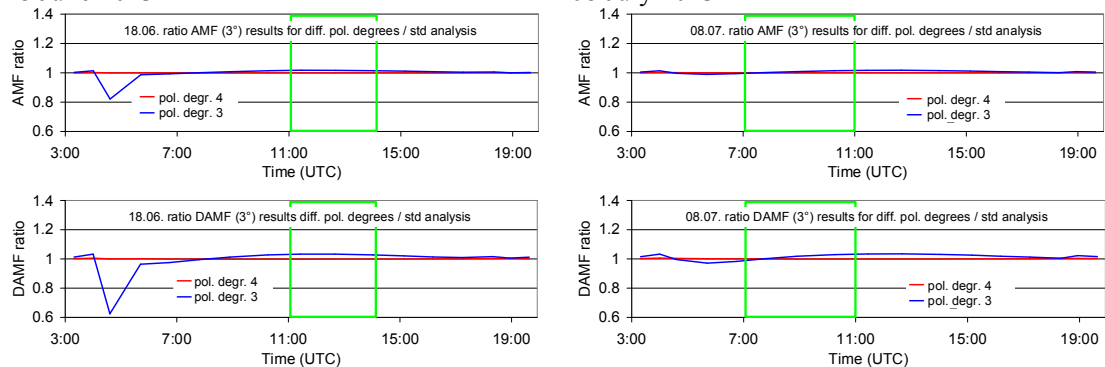
8 July 2013

2351 a) measured spectra



2352
2353

b) synthetic spectra



2354
2355
2356
2357
2358

Fig. A16 Ratio of the O_4 (d)AMFs derived for different polynomials versus those for the standard analysis (polynomial degree 5) for both selected days (top: results for spectra measured by the MPIC instrument; bottom: results for synthetic spectra taking into account the temperature dependence of the O_4 cross section).

2359
2360
2361
2362
2363
2364
2365

Table A15 Average ratios of O_4 (d)AMFs derived for different polynomials versus those for the standard analysis (polynomial degree 5) for the two middle periods on both selected days (top: results for spectra measured by the MPIC instrument; bottom: results for synthetic spectra taking into account the temperature dependence of the O_4 cross section).

	AMF ratios		dAMF ratios		
Degree of polynomial	18 June 2013, 11:00 – 14:00	8 July 2013, 7:00 – 11:00		18 June 2013, 11:00 – 14:00	8 July 2013, 7:00 – 11:00
Measured Spectra					
4	1.04	1.02		1.06	1.03
3	1.03	1.03		1.06	1.06
Synthetic Spectra					
4	1.00	1.00		1.00	1.00
3	1.02	1.01		1.03	1.01

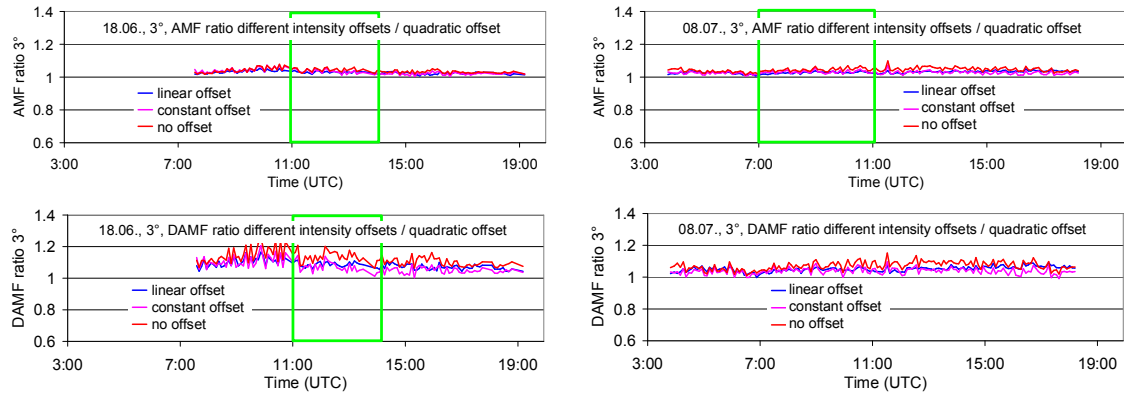
2366

18 June 2013

8 July 2013

2367

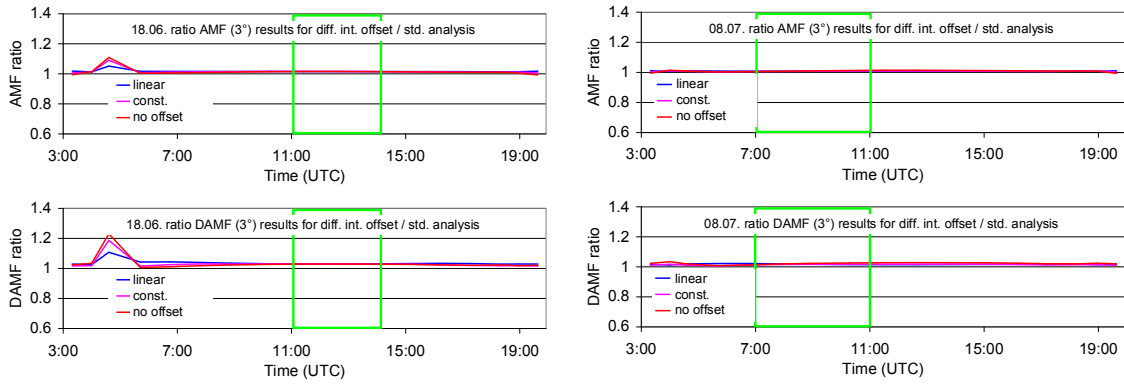
a) measured spectra



2368

2369

b) synthetic spectra



2370

2371

2372

2373

2374

2375

2376

2377

2378

2379

2380

2381

2382

2383

2384

2385

2386

2387

2388

2389

2390

2391

2392

2393

2394

2395

2396

Fig. A17 Ratio of the O_4 (d)AMFs derived for different intensity offsets versus those for the standard analysis (intensity offset of degree 2) for both selected days (top: results for spectra measured by the MPIC instrument; bottom: results for synthetic spectra taking into account the temperature dependence of the O_4 cross section).

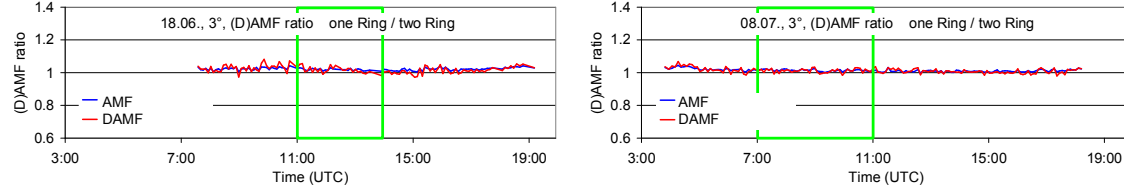
2397 selected days (top: results for spectra measured by the MPIC instrument; bottom: results for
 2398 synthetic spectra taking into account the temperature dependence of the O₄ cross section).

	AMF ratios		dAMF ratios		
Intensity offset	18 June 2013, 11:00 – 14:00	8 July 2013, 7:00 – 11:00		18 June 2013, 11:00 – 14:00	8 July 2013, 7:00 – 11:00
Measured Spectra					
Linear	1.04	1.03		1.11	1.05
Constant	1.05	1.03		1.11	1.04
No offset	1.05	1.05		1.16	1.07
Synthetic Spectra					
Linear	1.01	1.01		1.03	1.02
Constant	1.02	1.01		1.03	1.02
No offset	1.02	1.01		1.03	1.02

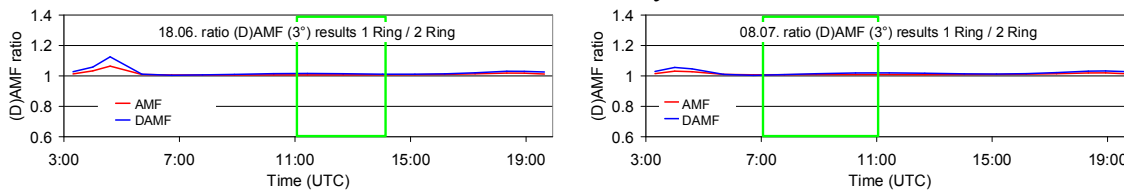
2399
 2400
 2401
 2402

2403 18 June 2013 8 July 2013

a) measured spectra



b) synthetic spectra



2404
 2405

2406 Fig. A18 Ratio of the O₄ (d)AMFs derived for the analysis with only one Ring spectrum
 2407 versus those for the standard analysis (using two Ring spectra) for both selected days (top:
 2408 results for spectra measured by the MPIC instrument; bottom: results for synthetic spectra
 2409 taking into account the temperature dependence of the O₄ cross section).

2410

2411

2412

2413

2414

2415

2416

2417

2418

2419

2420

Table A17 Average ratios of O₄ (d)AMFs derived for the analysis with only one Ring spectrum versus those for the standard analysis (using two Ring spectra) for the two middle periods on both selected days (top: results for spectra measured by the MPIC instrument;

2421 bottom: results for synthetic spectra taking into account the temperature dependence of the O₄
 2422 cross section).

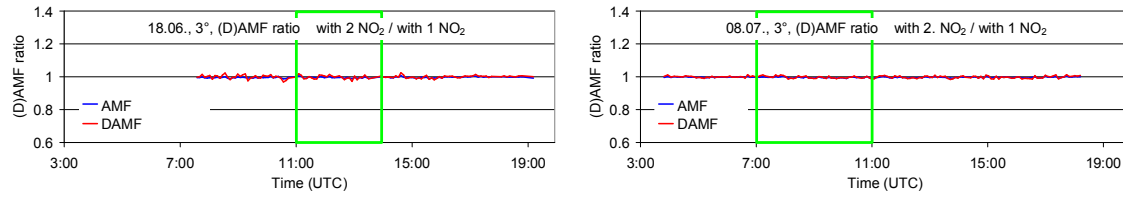
	AMF ratios			dAMF ratios	
Ring correction	18 June 2013, 11:00 – 14:00	8 July 2013, 7:00 – 11:00		18 June 2013, 11:00 – 14:00	8 July 2013, 7:00 – 11:00
Measured Spectra					
Only one Ring spectrum	1.02	0.99		1.01	0.99
Synthetic Spectra					
Only one Ring spectrum	1.01	1.01		1.01	1.01

2423
 2424
 2425
 2426

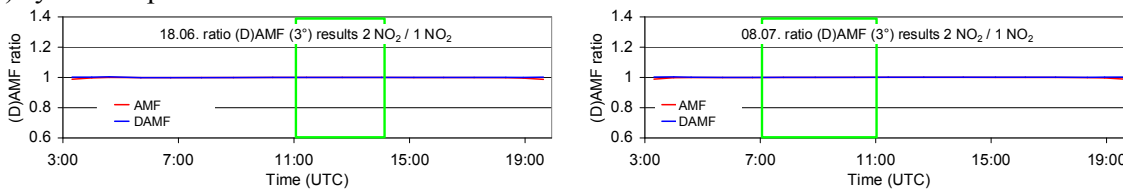
18 June 2013

8 July 2013

2427 a) measured spectra



2428
 2429 b) synthetic spectra



2430
 2431
 2432
 2433
 2434
 2435
 2436
 2437
 2438
 2439
 2440
 2441
 2442
 2443
 2444
 2445
 2446
 2447

Fig. A19 Ratio of the O₄ (d)AMFs derived for the analysis with a second NO₂ cross section (for 220 K) versus those for the standard analysis (only NO₂ cross section for 294 K) for both selected days (top: results for spectra measured by the MPIC instrument; bottom: results for synthetic spectra taking into account the temperature dependence of the O₄ cross section).

2448 Table A18 Average ratios of O₄ (d)AMFs derived for the analysis with a second NO₂ cross
 2449 section (for 220 K) versus those for the standard analysis (only NO₂ cross section for 294 K)
 2450 for the two middle periods on both selected days (top: results for spectra measured by the
 2451 MPIC instrument; bottom: results for synthetic spectra taking into account the temperature
 2452 dependence of the O₄ cross section).

	AMF ratios		dAMF ratios	
NO ₂ cross sections	18 June 2013, 11:00 – 14:00	8 July 2013, 7:00 – 11:00	18 June 2013, 11:00 – 14:00	8 July 2013, 7:00 – 11:00
Measured Spectra				
294 & 220 K	1.00	1.00	1.00	1.00
Synthetic Spectra				
294 & 220 K	1.00	1.00	1.00	1.00

2453

2454

2455

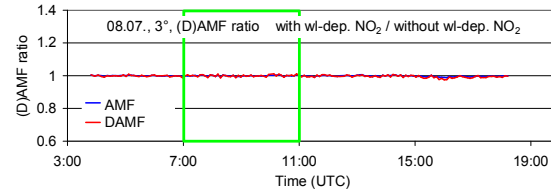
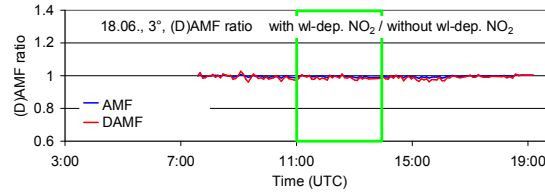
2456

18 June 2013

8 July 2013

2457

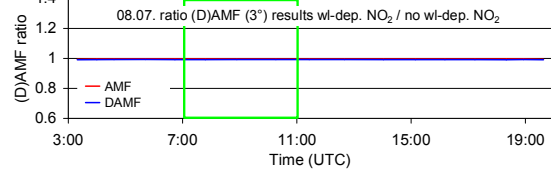
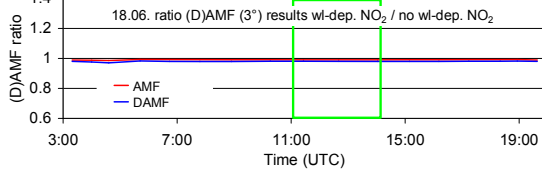
a) measured spectra



2458

2459

b) synthetic spectra



2460

2461

2462

2463

2464

2465

Fig. A20 Ratio of the O₄ (d)AMFs derived for the analysis with a second NO₂ cross section (cross section times wavelength) versus those for the standard analysis (only one NO₂ cross section) for both selected days (top: results for spectra measured by the MPIC instrument; bottom: results for synthetic spectra taking into account the temperature dependence of the O₄ cross section).

2466

2467

2468

2469

2470

2471

2472

2473

2474

2475

2476

2477 Table A19 Average ratios of O₄ (d)AMFs derived for the analysis with a second NO₂ cross
 2478 section (cross section times wavelength) versus those for the standard analysis (only one NO₂
 2479 cross section) for the two middle periods on both selected days (top: results for spectra
 2480 measured by the MPIC instrument; bottom: results for synthetic spectra taking into account
 2481 the temperature dependence of the O₄ cross section).

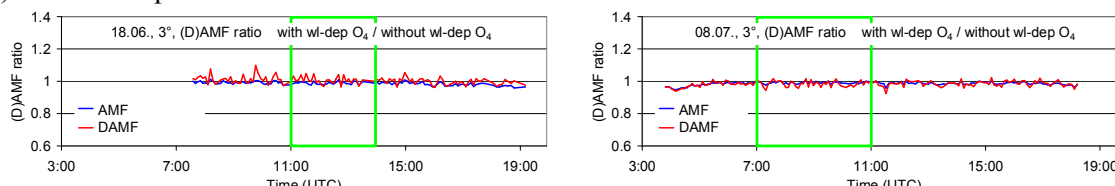
	AMF ratios		dAMF ratios		
NO ₂ wavelength dependence	18 June 2013, 11:00 – 14:00	8 July 2013, 7:00 – 11:00		18 June 2013, 11:00 – 14:00	8 July 2013, 7:00 – 11:00
Measured Spectra					
additional cross for wavelength dependence	1.00	1.00		0.99	1.00
Synthetic Spectra					
additional cross for wavelength dependence	0.99	1.00		0.98	0.99

2482
 2483
 2484
 2485

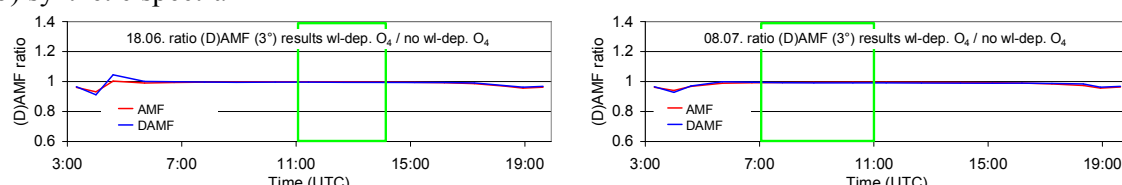
18 June 2013

8 July 2013

2486 a) measured spectra



2487
 2488 b) synthetic spectra



2489

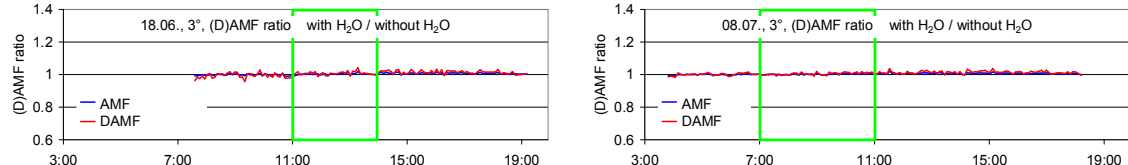
2490 Fig. A21 Ratio of the O₄ (d)AMFs derived for the analysis with a second O₄ cross section
 2491 (accounting for the wavelength dependence) versus those for the standard analysis (only one O₄
 2492 cross section) for both selected days (top: results for spectra measured by the MPIC
 2493 instrument; bottom: results for synthetic spectra taking into account the temperature
 2494 dependence of the O₄ cross section).

2495
 2496
 2497
 2498
 2499
 2500
 2501

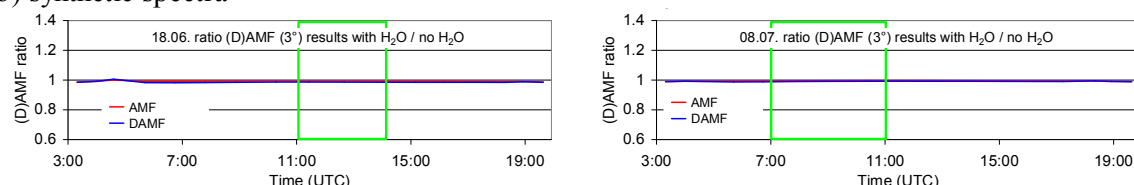
2502
 2503 Table A20 Average ratios of O₄ (d)AMFs derived for the analysis with a second O₄ cross
 2504 section (accounting for the wavelength dependence) versus those for the standard analysis
 2505 (only one O₄ cross section) for the two middle periods on both selected days (top: results for
 2506 spectra measured by the MPIC instrument; bottom: results for synthetic spectra taking into
 2507 account the temperature dependence of the O₄ cross section).

	AMF ratios		dAMF ratios	
O ₄ wavelength dependence	18 June 2013, 11:00 – 14:00	8 July 2013, 7:00 – 11:00	18 June 2013, 11:00 – 14:00	8 July 2013, 7:00 – 11:00
Measured Spectra				
additional cross for wavelength dependence	0.99	0.99	1.01	0.99
Synthetic Spectra				
additional cross for wavelength dependence	1.00	0.99	1.00	0.99

2508
 2509
 2510
 2511
 2512
 2513 18 June 2013 8 July 2013
 a) measured spectra



2514
 2515 b) synthetic spectra



2516 Fig. A22 Ratio of the O₄ (d)AMFs derived for the analysis including a H₂O cross section
 2517 versus those for the standard analysis (no H₂O cross section) for both selected days (top: results for spectra measured by the MPIC instrument; bottom: results for synthetic spectra taking into account the temperature dependence of the O₄ cross section).

2529

2530 Table A21 Average ratios of O₄ (d)AMFs derived for the analysis including a H₂O cross
 2531 section versus those for the standard analysis (no H₂O cross section) for the standard analysis
 2532 (only one O₄ cross section) for the two middle periods on both selected days (top: results for
 2533 spectra measured by the MPIC instrument; bottom: results for synthetic spectra taking into
 2534 account the temperature dependence of the O₄ cross section).

	AMF ratios		dAMF ratios	
H ₂ O cross section	18 June 2013, 11:00 – 14:00	8 July 2013, 7:00 – 11:00	18 June 2013, 11:00 – 14:00	8 July 2013, 7:00 – 11:00
Measured spectra				
H ₂ O cross section included	1.00	1.00	1.01	1.01
Synthetic Spectra				
H ₂ O cross section included	0.99	1.00	0.99	0.99

2535

2536

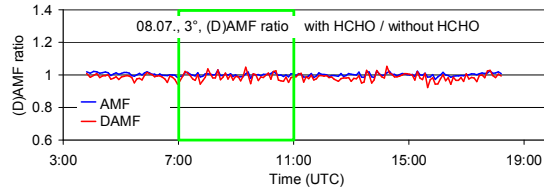
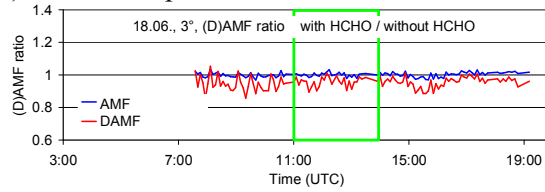
2537

2538

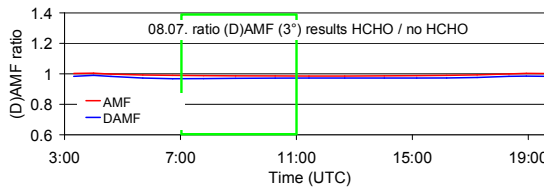
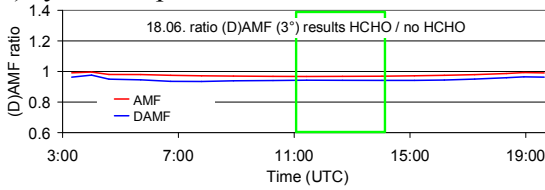
18 June 2013

8 July 2013

a) measured spectra



b) synthetic spectra



2540

2541

2542

2543

2544

2545

2546

2547

2548

2549

2550

2551

2552

2553

Fig. A23 Ratio of the O₄ (d)AMFs derived for the analysis including a HCHO cross section versus those for the standard analysis (no HCHO cross section) for both selected days (top: results for spectra measured by the MPIC instrument; bottom: results for synthetic spectra taking into account the temperature dependence of the O₄ cross section).

2554
 2555 Table A22 Average ratios of O₄ (d)AMFs derived for the analysis including a HCHO cross
 2556 section versus those for the standard analysis (no HCHO cross section) for the standard
 2557 analysis (only one O₄ cross section) for the two middle periods on both selected days (top:
 2558 results for spectra measured by the MPIC instrument; bottom: results for synthetic spectra
 2559 taking into account the temperature dependence of the O₄ cross section).

	AMF ratios			dAMF ratios	
HCHO cross section	18 June 2013, 11:00 – 14:00	8 July 2013, 7:00 – 11:00		18 June 2013, 11:00 – 14:00	8 July 2013, 7:00 – 11:00
Measured Spectra					
HCHO cross section included	1.00	1.00		0.96	0.98
Synthetic Spectra					
HCHO cross section included	0.97	0.99		0.94	0.97

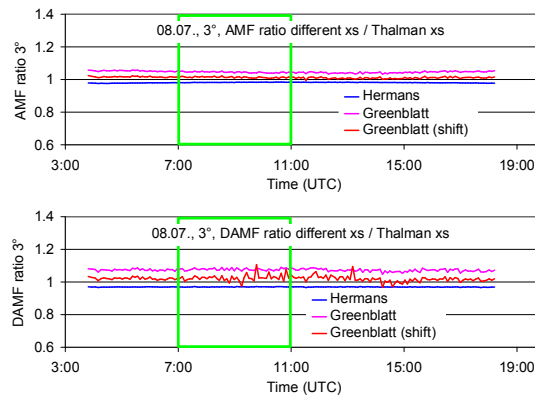
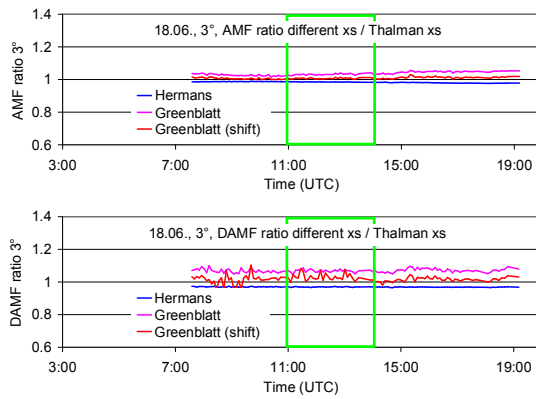
2560
 2561
 2562
 2563
 2564
 2565
 2566
 2567
 2568
 2569
 2570
 2571
 2572
 2573
 2574
 2575
 2576
 2577
 2578
 2579
 2580
 2581
 2582
 2583
 2584
 2585
 2586
 2587
 2588
 2589
 2590

18 June 2013

8 July 2013

2591

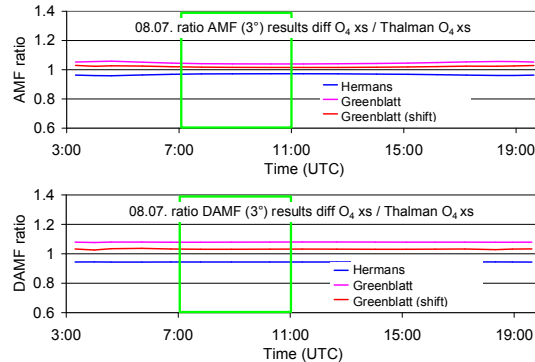
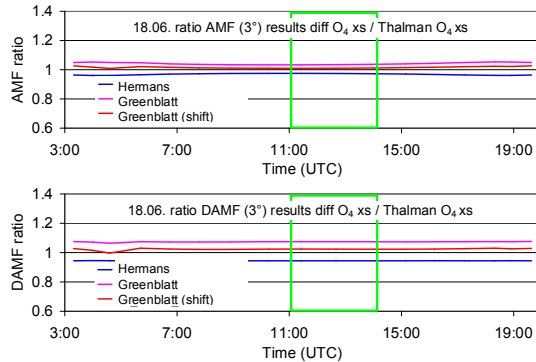
a) measured spectra



2592

2593

b) synthetic spectra



2594

2595

2596

2597

2598

2599

2600

2601

2602

2603

2604

2605

2606

2607

2608

2609

2610

2611

2612

2613

2614

2615

2616

2617

2618

2619

Fig. A24 Ratio of the O₄ (d)AMFs derived for the analyses using different O₄ cross sections versus those for the standard analysis (using the Thalman and Volkamer (2013) cross section) for both selected days (top: results for spectra measured by the MPIC instrument; bottom: results for synthetic spectra taking into account the temperature dependence of the O₄ cross section).

2620 Table A23 Average ratios of O_4 (d)AMFs derived for the analyses using different O_4 cross
 2621 section versus those for the standard analysis (using the Thalman et al. cross section) for the
 2622 standard analysis (only one O_4 cross section) for the two middle periods on both selected days
 2623 (top: results for spectra measured by the MPIC instrument; bottom: results for synthetic
 2624 spectra taking into account the temperature dependence of the O_4 cross section).

	AMF ratios		dAMF ratios		
O_4 cross section	18 June 2013, 11:00 – 14:00	8 July 2013, 7:00 – 11:00		18 June 2013, 11:00 – 14:00	8 July 2013, 7:00 – 11:00
Measured spectra					
Hermans	0.98	0.98		0.97	0.97
Greenblatt	1.03	1.04		1.07	1.08
Greenblatt shifted	1.01	1.01		1.03	1.03
Synthetic Spectra					
Hermans	0.97	0.97		0.94	0.94
Greenblatt	1.03	1.04		1.07	1.08
Greenblatt shifted	1.01	1.02		1.02	1.03

2625
 2626
 2627

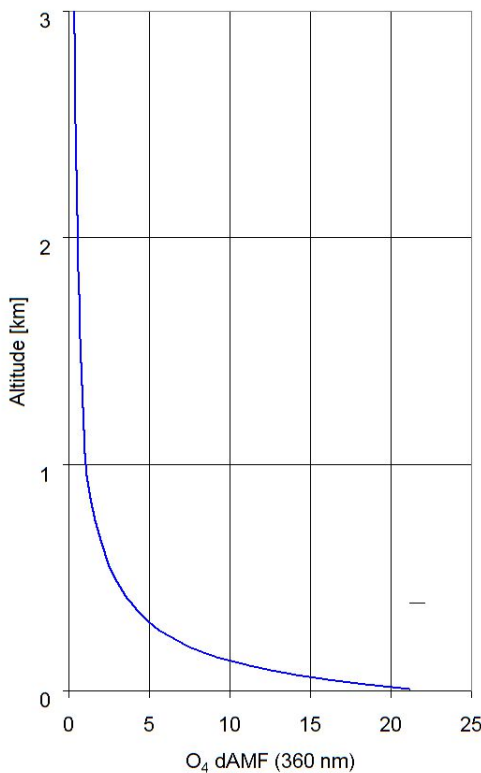


Fig. 25 O_4 differential box-AMFs (with 20m vertical resolution) used for the simulation of the temperature-dependent O_4 absorption spectra. They are averages of radiative transfer simulations for several scenarios. Simulations are performed for a surface albedo of 6 %, aerosol profiles with constant extinction between 0 and 1000m and different AOD (0.1, 0.3, 0.7) and for all combinations of SZA (40, 60°), relative azimuth angles (0, 90, 180°) and elevation angles (2° and 3°).

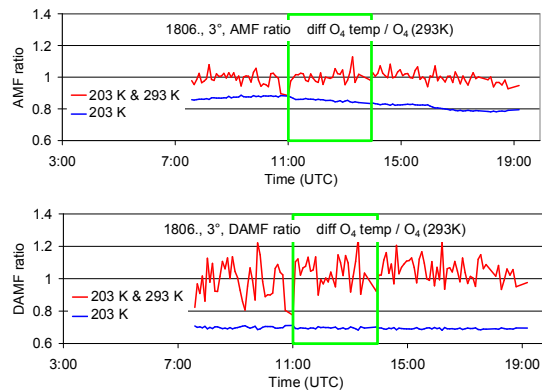
2628

18 June 2013

8 July 2013

2629

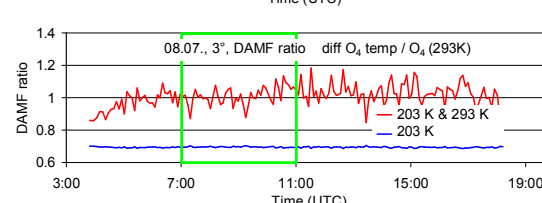
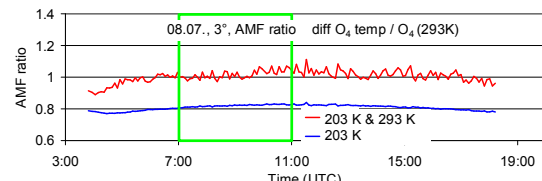
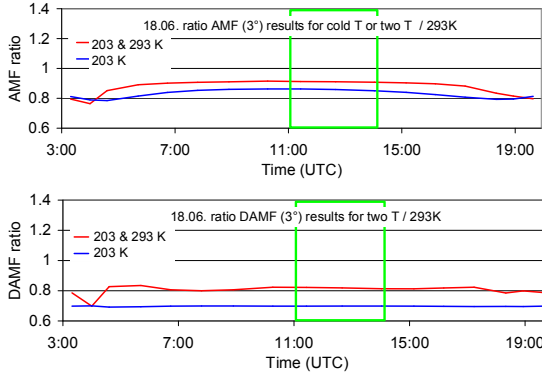
a) measured spectra



2630

2631

b) synthetic spectra



2632

2633

2634

2635

2636

2637

Fig. A26 Ratio of the O_4 (d)AMFs derived for O_4 cross sections at different temperatures (either 203 K or both 203 and 293 K) versus those for the standard analysis (using the O_4 cross section for 293 K) for both selected days (top: results for spectra measured by the MPIC instrument; bottom: results for synthetic spectra taking into account the temperature dependence of the O_4 cross section).

2638

2639

2640

2641

2642

2643

2644

2645

2646

2647

2648

2649

2650

2651

2652

2653

2654

2655

2656

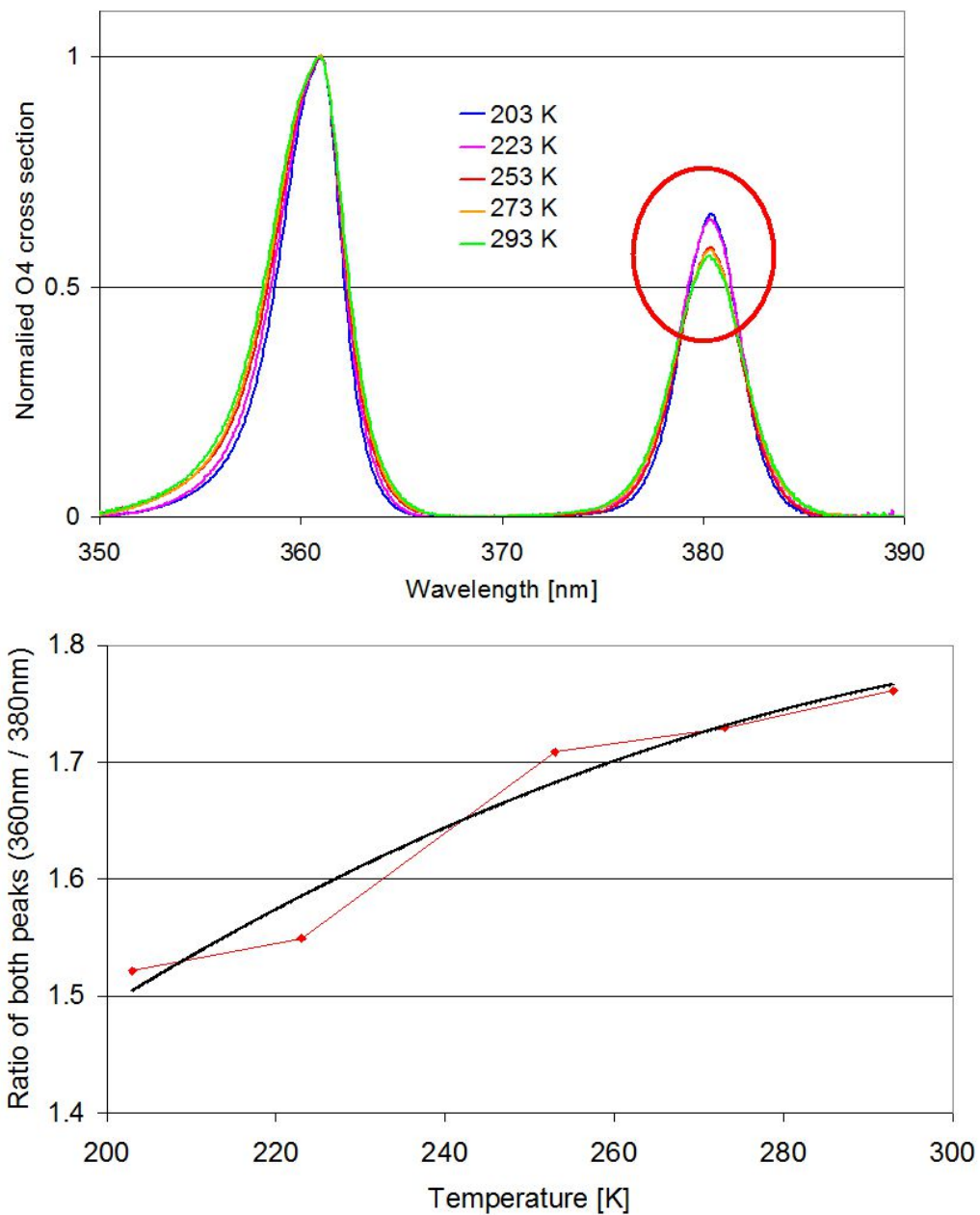
2657

2658

2659 Table A24 Average ratios of O₄ (d)AMFs derived O₄ cross sections at different temperatures
 2660 (either 203 K or both 203 and 293 K) versus those for the standard analysis (using the O₄
 2661 cross section for 293 K) for the two middle periods on both selected days (top: results for
 2662 spectra measured by the MPIC instrument; bottom: results for synthetic spectra taking into
 2663 account the temperature dependence of the O₄ cross section). For the simultaneous fit of both
 2664 temperatures also the results for the spectral range 345 – 374 nm (one O₄ absorption band) are
 2665 included.

	AMF ratios			dAMF ratios	
O ₄ cross sections	18 June 2013, 11:00 – 14:00	8 July 2013, 7:00 – 11:00		18 June 2013, 11:00 – 14:00	8 July 2013, 7:00 – 11:00
Measured Spectra					
203 K	0.85	0.82		0.70	0.70
203 & 293 K	1.00	1.02		1.04	1.01
203 & 293 K (345 – 374 nm)	0.91	1.04		0.95	1.02
Synthetic Spectra					
203 K	0.86	0.84		0.70	0.69
203 & 293 K	0.91	0.94		0.82	0.89
203 & 293 K (345 – 374 nm)	0.99	1.00		0.99	1.00

2666
 2667
 2668
 2669
 2670
 2671
 2672
 2673
 2674
 2675
 2676
 2677
 2678
 2679
 2680
 2681
 2682
 2683
 2684
 2685
 2686
 2687
 2688
 2689
 2690
 2691



2693 Fig. A27 Top: Comparison of the O₄ cross sections from Thalman and Volkamer (2013) for
2694 different temperatures. The cross sections are divided by the maximum values at 360 nm.
2695 After this normalisation, the resulting values at 380 nm fall into two groups (high values for
2696 203 & 223K, low values for 253, 273, 293K). Bottom: Ratio of the peaks of the O₄ cross
2697 section at 360 nm and 380 nm as function of temperature (red points). The black curve is a
2698 fitted low order polynomial.

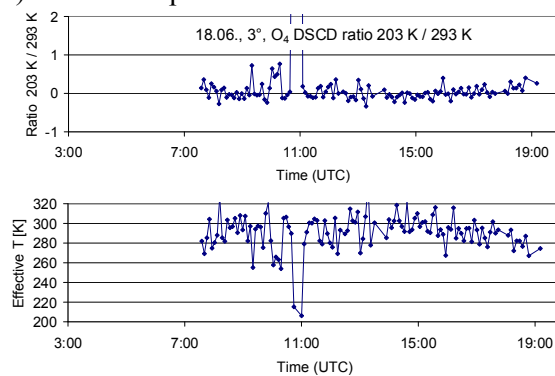
2699
2700
2701
2702
2703
2704
2705

2706
2707

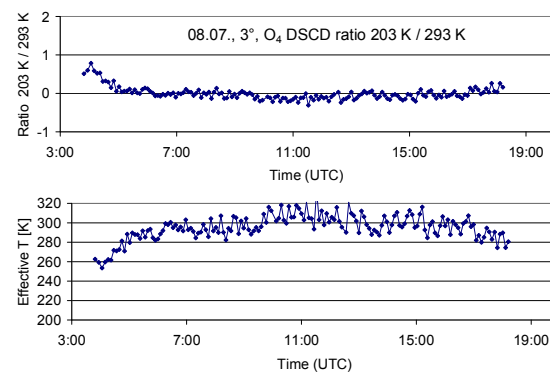
18 June 2013

2708

a) measured spectra

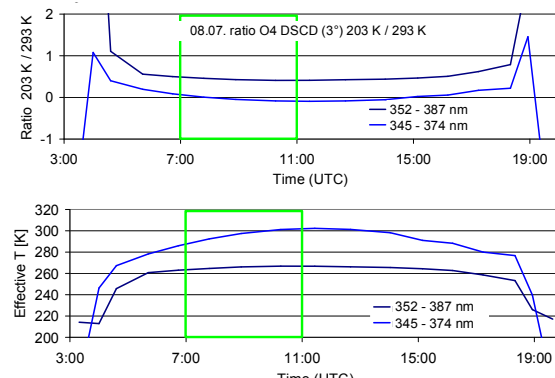
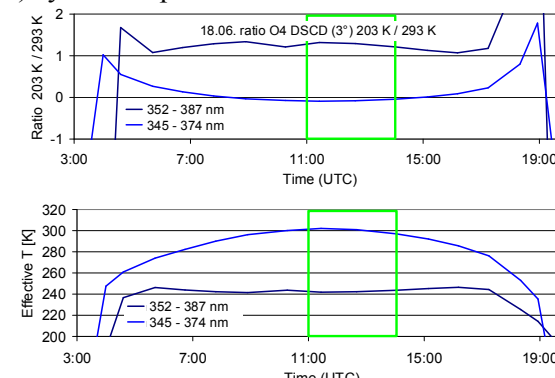


8 July 2013



2709

b) synthetic spectra



2710

2711

Fig. A28 Ratio of the derived O₄ dSCDs for 203 K and 293 K as well as the derived effective temperatures for the analyses with both cross sections included.

2712

2713

2714

2715

2716

2717

2718

2719

2720

2721

2722

2723

2724

2725

2726

2727

2728

2729

2730

2731

2732

2733

2734

2735
 2736
 2737 Table A25 a) Average ratios of O₄ (d)AMFs derived from the analysis of MPIC spectra by
 2738 different groups versus the analysis of MPIC spectra by MPIC (standard analysis). b) Average
 2739 ratios of O₄ (d)AMFs derived from spectra of other groups analysed by MPIC versus the
 2740 analysis of MPIC spectra by MPIC (using the same analysis settings and spectral range: 335 –
 2741 374 nm). c) Average ratios of O₄ (d)AMFs derived from spectra of other groups analysed by
 2742 the same groups using individual analysis settings versus the analysis of MPIC spectra by
 2743 MPIC (standard analysis).

	AMF ratios		dAMF ratios		
Measurements / Analysis	18 June 2013, 11:00 – 14:00	8 July 2013, 7:00 – 11:00		18 June 2013, 11:00 – 14:00	8 July 2013, 7:00 – 11:00
a) MPIC spectra analysed by other groups					
BIRA	0.96	0.98		0.95	0.95
IUP-B	1.03	0.98		1.05	0.99
INTA	1.02	0.97		1.05	0.94
CMA	0.97	0.98		0.98	0.95
CSIC	0.94	0.94		0.95	0.94
b) Other spectra analysed by MPIC (335 – 374 nm)					
BIRA	0.98	0.99		0.89	0.95
IUP-B	1.05			1.07	
IUP-HD	0.97			1.00	
c) Other spectra analysed by the same groups					
BIRA	0.94	0.94		0.91	0.92
IUP-B	0.95			0.88	
IUP-HD	1.01			1.04	

2744
 2745
 2746
 2747
 2748
 2749
 2750
 2751
 2752
 2753
 2754
 2755
 2756
 2757
 2758
 2759
 2760
 2761
 2762
 2763

2764 **Appendix A5 Extraction of aerosol extinction profiles**

2765
2766 In this section, the procedure for the extraction of aerosol extinction profiles is described. The
2767 aerosol profiles are derived from the ceilometer measurements (yielding the profile
2768 information) in combination with the sun photometer measurements (yielding the vertically
2769 integrated aerosol extinction, the aerosol optical depth AOD).

2770 The ceilometer raw data consist of range-corrected backscatter profiles averaged over 15
2771 minutes. The profiles range from the surface to an altitude of 15360m with a height resolution
2772 of 15m. Here it is important to note that due to limited overlap of the outgoing Laser beam and
2773 the field of view of the telescope, no profile data is available below 180 m. The ceilometer
2774 profiles (hourly averages) are shown in Fig. A29 for both selected days.

2775 The AERONET sun photometer data provide the AOD at different wavelengths (340, 360,
2776 440, 500, 675, 870, and 1020 nm) in time intervals of 2 – 25 min if the direct sun is visible.

2777 To determine profiles of aerosol extinction from the ceilometer backscatter data, several
2778 processing steps have to be performed. They are described in the sub-sections below.

2779
2780 **A) Smoothing and extrapolating of the ceilometer backscatter profiles**

2781
2782 First, the ceilometer data are averaged over several hours to reduce the scatter. For that
2783 purpose on both days three time periods are identified, for which the backscatter profile show
2784 relatively small variations. The profiles for these periods are shown in Fig. A29. In addition
2785 to the temporal averaging, the profiles are also vertically smoothed above 2 km. Above
2786 altitudes between 5 to 6 km (depending on the period) the (smoothed) ceilometer backscatter
2787 profiles become zero. Thus the aerosol extinction profiles above these altitudes are set to zero.
2788 Below 180 m above the surface the ceilometer becomes ‘blind’ for the aerosol extinction
2789 because of the insufficient overlap between the outgoing laser beam and the field of view of
2790 the telescope. Thus the profiles have to be extrapolated down to the surface. This
2791 extrapolation constitutes an important source of uncertainty. To estimate the associated errors,
2792 the extrapolation is performed in three different ways:

2793 1) The value below 180 m are set to the value measured at 180m.
2794 2) The values below 180m are linearly extrapolated assuming the same slope below 180 m as
2795 between 180m and 240m.
2796 3) The values below 180m are linearly extrapolated by the double slope between 180m and
2797 240m.

2798

2799

2800

2801

2802

2803

2804

2805

2806

2807

2808

2809

2810

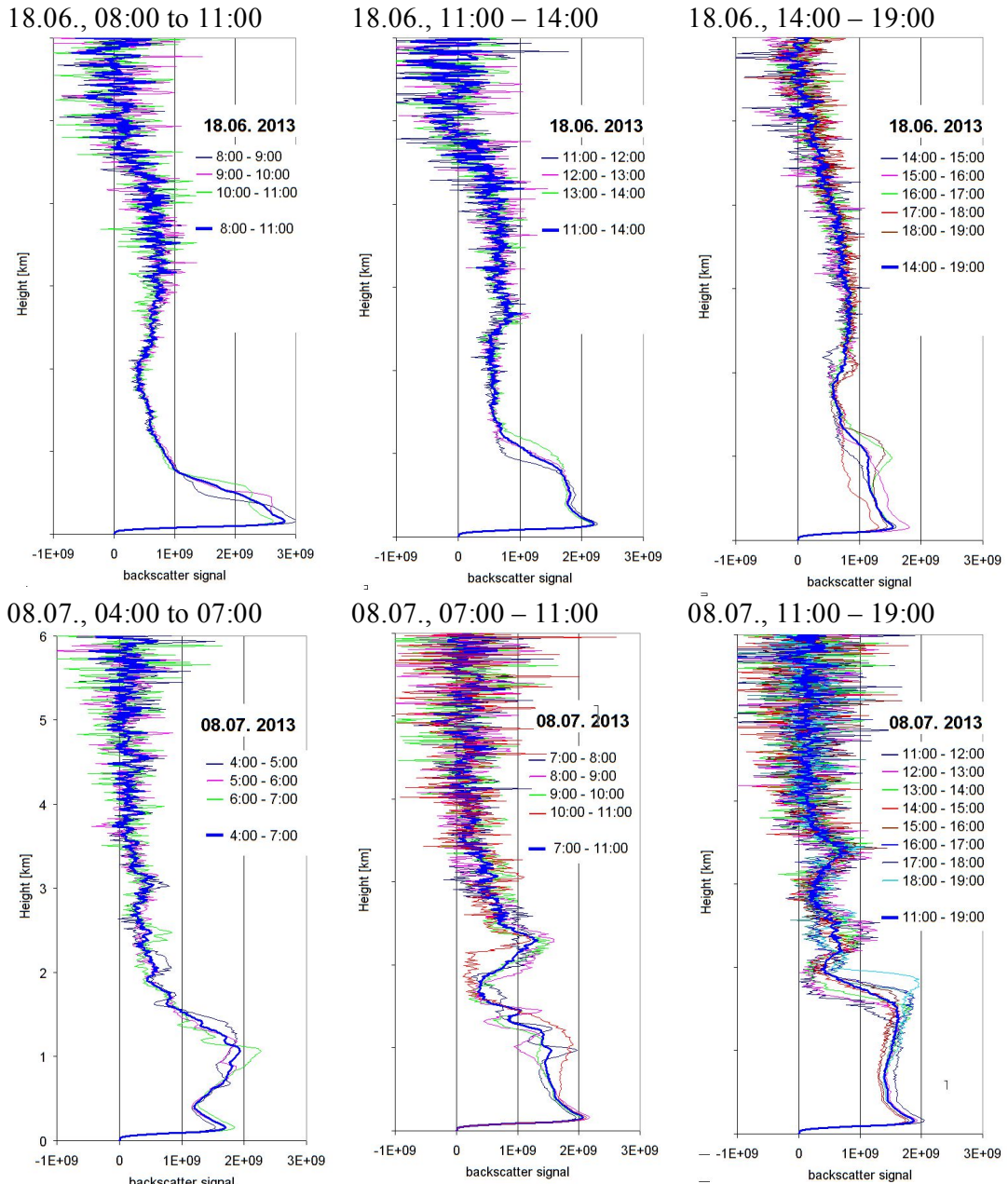
2811

2812

2813

2814

2815



2816 Fig. A29 Range-corrected backscatter profiles (hourly averages) for the three selected periods
 2817 on both days. Also the averages over the the whole periods are shown (thick lines).

2818

2819

2820 B) Scaling of the Ceilometer profiles by sun photometer AOD at 1020 nm

2821

2822 The scaling of the ceilometer backscatter profiles by the AOD at 1020 nm is an intermediate
 2823 step, which is necessary for the correction of the aerosol self-extinction. The average AOD at
 2824 1020 nm for the different selected time periods on both days is shown in Table A26. In that
 2825 table also the average values at 380 nm are shown, which are used for a second scaling (see
 2826 below).

2827 The backscatter profiles are vertically integrated and then the whole profiles are scaled by the
 2828 ratio:

2829
 2830 $AOD_{1020\text{nm}} / B_{\text{int}}$ (A1)
 2831

2832 Here B_{int} indicates the integrated backscatter profile.
 2833

2834 Note that the wavelength of the ceilometer measurements (1064 nm) is slightly different from
 2835 the sun photometer measurements (1020 nm), but the difference of the AOD is negligible
 2836 (typically < 4%).
 2837

2838 Table A26 Average AOD at 1020 and 360 nm derived from the sun photometer.

Time	AOD 1020 nm	AOD 360 nm*
18.06.2013, 08:00 - 11:00	0.124	0.379
18.06.2013, 11:00 - 14:00	0.122	0.367
18.06.2013, 14:00 - 19:00	0.118	0.296
08.07.2013, 04:00 - 07:00	0.045	0.295
08.07.2013, 07:00 - 14:00	0.053	0.333
08.07.2013, 11:00 - 19:00	0.055	0.348

2839 *Average of AOD at 340 nm and 380 nm.
 2840
 2841

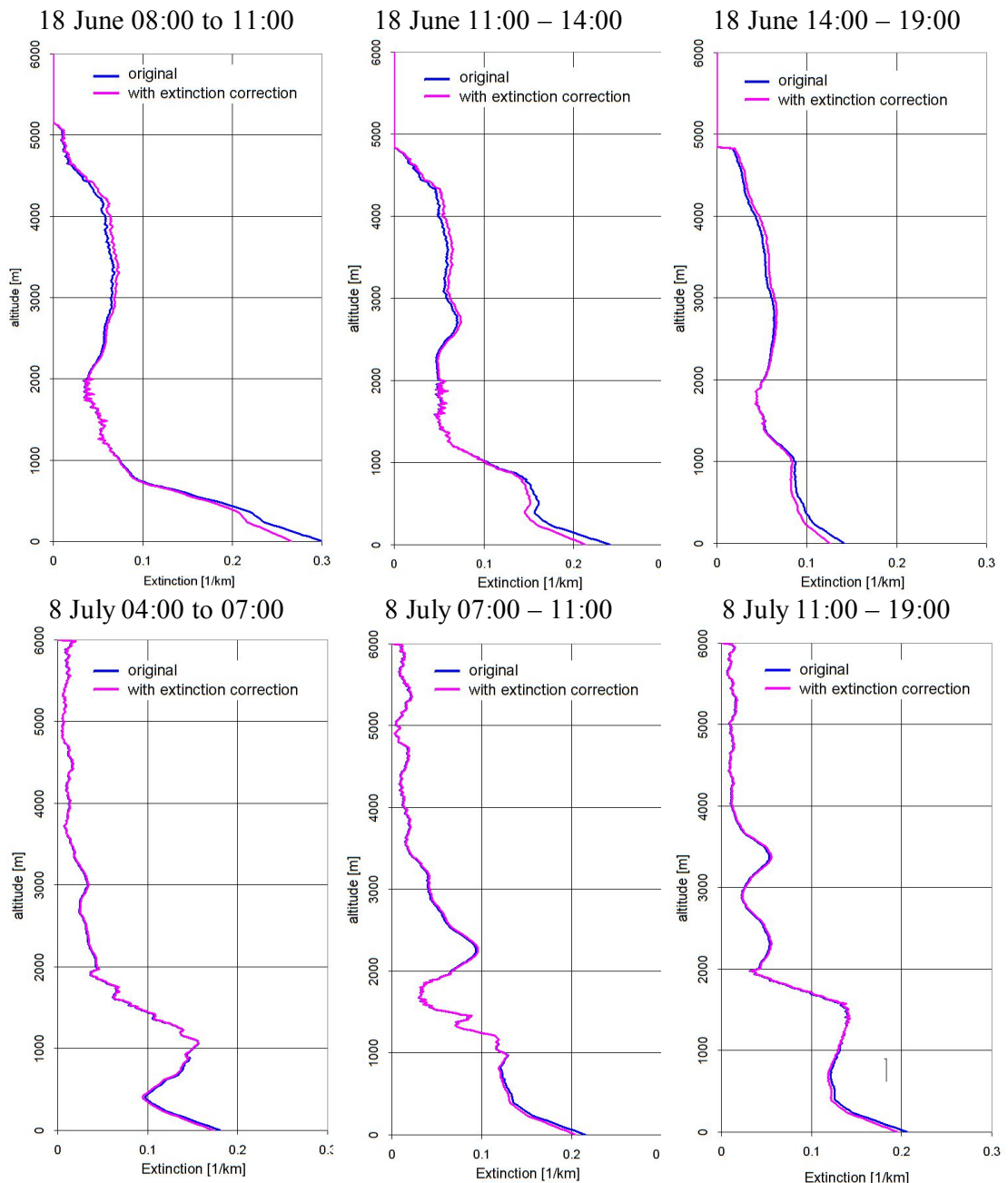
2842 C) Correction of the aerosol extinction 2843

2844 The photons received by the ceilometer have undergone atmospheric extinction. Here,
 2845 Rayleigh scattering can be ignored because of the long wavelength of the ceilometer (optical
 2846 depth below 2 km is < 0.001). However, while the extinction due to aerosol scattering is also
 2847 small at these long wavelengths it systematically affects the ceilometer signal and has to be
 2848 corrected. The extinction correction is performed according to the following formula:
 2849

2850
$$\alpha_{i,\text{corr}} = \frac{\alpha_i}{\exp\left(-2 \cdot \sum_{z_0}^{z_{i-1}} \alpha_{j,\text{corr}} \cdot (z_j - z_{j-1})\right)}$$
 (A2)

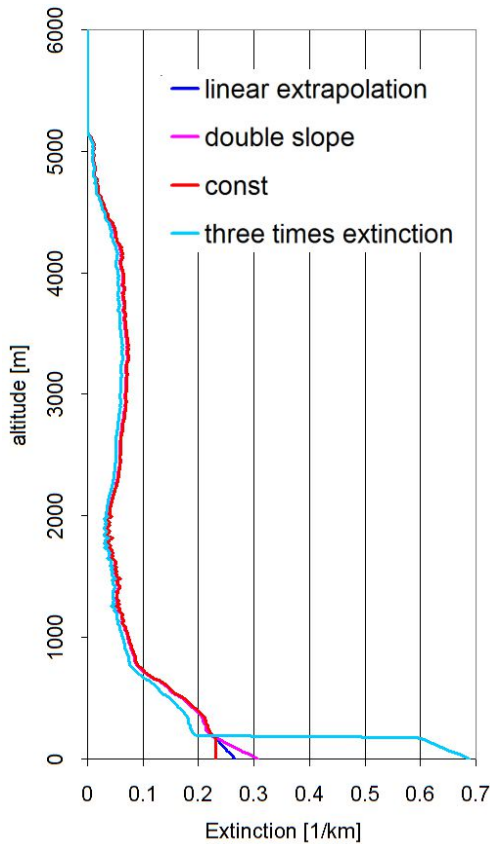
2851 Here α_i represent the uncorrected extinction and $\alpha_{i,\text{corr}}$ represents the corrected extinction at
 2852 height layer i (with z_i is the lower boundary of that height layer). Equation C1 has to be
 2853 subsequently applied to all height layers starting from the surface (z_0). Note that the factor of
 2854 two accounts for the extinction both paths between the instrument and the scattering altitude
 2855 (way up and down). The extinction correction is performed at a vertical resolution of 15m.
 2856 After the extinction correction, the profiles are scaled by the corresponding AOD at 360 nm
 2857 (see table A26 In Fig. A30 the profiles with and without extinction correction are shown. The
 2858 extinction correction slightly increases the values at higher altitudes and decreases the values
 2859 close to the surface. The effect of the extinction correction is larger on 18 June 2013 (up to 12
 2860 %).
 2861

2862
 2863
 2864
 2865
 2866
 2867
 2868



2869 Fig. A30 Comparison of profiles (linear extrapolation below 180 m) without (blue)
 2870 and with (magenta) extinction correction. Both profiles are scaled to the same total AOD (at 360 nm)
 2871 determined from the sun photometer.

2872
 2873



2874
2875 Fig. A31 Aerosol profile (light blue) with extreme extinction close to the surface (below 180
2876 m, the altitude for which the ceilometer is sensitive) extracted for the first period (8:00 –
2877 11:00) on 18 June 2013. Also shown are the profiles extrapolated below 180 as described
2878 above.

D) Influence of a changing LIDAR ratio with altitude

2884 For the extraction of the aerosol profiles described above, a fixed LIDAR ratio was assumed,
2885 which implies that the aerosol properties are independent from altitude. However, this is a
2886 rather strong assumption, because it can be expected that the aerosol properties (e.g. the size)
2887 change with altitude. With the available limited information, it is impossible to derive detailed
2888 information about the altitude dependence of the aerosol properties, but it can be quantified
2889 how representative the ceilometer measurements at 1064 nm are for the aerosol extinction
2890 profiles at 360 nm. For these investigations we again focus on the middle periods of both
2891 selected days. From the AERONET Almucantar observations information on the size
2892 distribution for these periods is available (see Fig. A32). On both days two pronounced modes
2893 (fine and coarse mode) are found with a much larger coarse mode fraction on 18 June
2894 compared to 8 July. From the AERONET observations, also separate phase functions for the
2895 fine and coarse mode as well as the relative contributions of both modes to the total aerosol
2896 optical depth at 500 nm are available. On 18 June and 8 July the relative contributions to the
2897 total AOD at 500 nm are 40 % and 5 %, respectively. Assuming that the AOD of the coarse
2898 mode fraction is independent on wavelength, the relative contributions of the coarse mode at
2899 360 nm and 1064 nm can be derived (see Table A27).

2900
2901

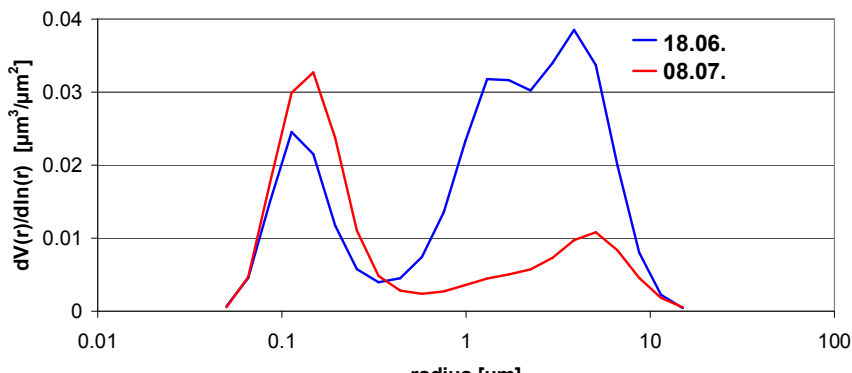


Fig. A32 Size distributions derived from AERONET Almucantar observations on 18 June (07:24 & 15:34) and 08 July (07:32 & 15:38).

Table A27 Contribution of the coarse mode to the total AOD at different wavelengths

Date	Total AOD 360 nm	Total AOD 1064 nm	Relative contribution of coarse mode 360 nm	Relative contribution of coarse mode 1064 nm
18 June, 11:00 – 14:00	0.37	0.12	24.9%	77.7%
08 July, 07:00 – 11:00	0.33	0.0535	3.0%	18.7%

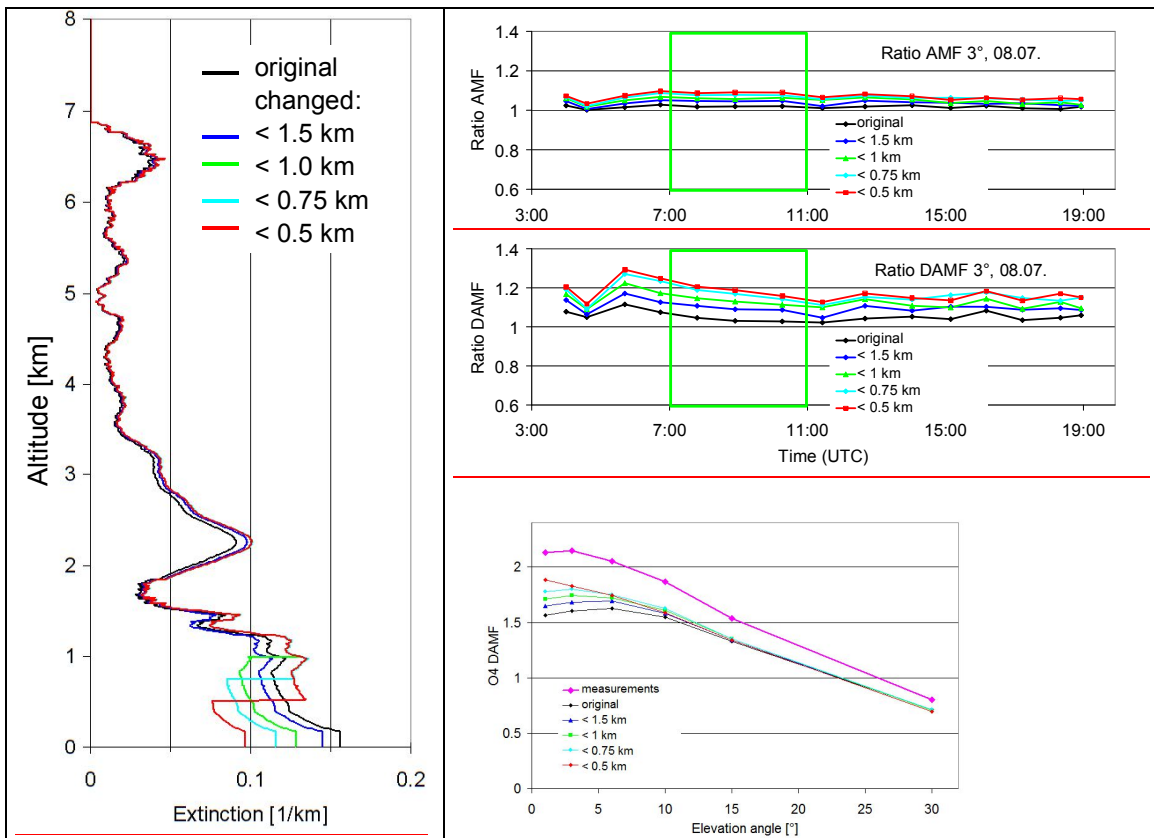
It is found that on 18 June the coarse mode clearly dominates the AOD at 1064 nm, whereas on 8 July it only contributes about 20 % to the total AOD. As expected the relative contributions of the coarse mode to the AOD at 360 nm are much smaller (25 % and 3%). In the last step the probability of aerosol scattering in backward direction is considered, because the ceilometer receives scattered light from that direction. For that purpose the ratios of the optical depths are multiplied by the corresponding values of the normalised phase functions at 180° and in this way the relative contributions to the backscattered signals from the coarse mode for both wavelengths and both days are calculated (Table A28). Interestingly, on 8 July the contributions of the coarse mode to the backscattered signal at both wavelengths differs by only about 10%. In contrast, on 18 June the difference is much larger.

Table A28 Ratio of phase functions (coarse / fine) in backward direction and relative contribution of coarse mode to the backscattered signal at both wavelengths

Date	Ratio phase function at 360 nm	Ratio phase function at 1064 nm	Relative contribution of coarse mode at 360 nm	Relative contribution of coarse mode at 1064 nm
18 June, 11:00 – 14:00	1.13	0.61	27.3%	68.0%
08 July, 07:00 – 11:00	2.7	0.99	7.8%	18.3%

For 8 July, the results can be interpreted in the following way: at 360 nm the aerosol profiles extracted as described above overestimate the contribution from the coarse mode by about

2929 10%. To estimate the effect of this overestimation we construct modified aerosol extinction
 2930 profiles, in which 10% of the total AOD is relocated. Since we expect that the coarse mode
 2931 aerosols are usually located at low altitude, we construct 4 different modified profiles (see
 2932 Fig. A33) with different altitudes (1.5 km, 1 km, 0.75 km, or 0.5 km), below which 10% of
 2933 the aerosol extinction is relocated to altitudes above (assuming that the coarse mode aerosol is
 2934 only located below these altitudes). Of course, such a sharp boundary is not very realistic, but
 2935 it allows to quantify the overall effect of the relocation. We selected the aerosol profile for 8
 2936 July extracted by INTA, which reached up to 7 km (see Fig. 9). It should be noted that if 10
 2937 % of the total AOD is relocated from the lowest layer to only the upper most layer no further
 2938 enhancement of the O_4 dAMF is found (see appendix A6).
 2939
 2940



2941 Fig. A33 Left: Modified aerosol profiles for 08 July assuming that the coarse mode aerosol is
 2942 only located in the lowest part of the atmosphere. Top right: ratios of the (d)AMFs calculated
 2943 for the modified profiles compared to the dAMFs for the standard settings. With decreasing
 2944 layer height the (d)AMFs increase systematically, because the aerosol extinction close to the
 2945 surface decreases. Right bottom: comparison of the measured elevation dependence of the O_4
 2946 dAMFs for the period 7:00 – 11:00 on 8 July and simulation results for the different profiles.
 2947
 2948

2949 Table A29 Ratio of the (d)AMFs for the modified profiles versus those of the standard
 2950 settings

	original INTA	coarse mode below 1.5 km	coarse mode below 1 km	coarse mode below 0.75 km	coarse mode below 0.5 km
AMF	1.02	1.04	1.05	1.06	1.08
dAMF	1.04	1.09	1.13	1.17	1.18

2951

2952 For all modified profiles, a systematic increase of the O_4 (d)AMFs compared to those for the
2953 standard settings is found. For the O_4 dAMFs this increase can be up to 18 % (see Table A29).
2954 From the comparison of the elevation dependence of the measured and simulated O_4 dAMFs
2955 (see Fig. A33), we conclude that the aerosol profile with the coarse mode aerosol below 0.75
2956 km is probably the most realistic one. The main conclusion from this section is that the
2957 dAMFs for 8 July derived from the standard settings probably underestimates the true dAMF
2958 by about $15 \pm 5 \%$.

2959 For 18 June we did not perform similarly detailed calculations, because on that day the
2960 uncertainties of the aerosol extinction profile caused by the missing sensitivity of the
2961 ceilometer below 180 m are much larger than on 8 July. On 18 June also the magnitude of the
2962 relocation of the aerosol extinction between different altitudes would be much larger than on
2963 8 July.

2968 Appendix A6 Influence of elevated aerosol layers on the O_4 (d)AMF

2969
2970 Ortega et al. (2016) showed that for their measurements the consideration of elevated aerosol
2971 layers (between about 3 and 5 km) is essential to bring measured and simulated O_4 (d)AMFs
2972 into agreement. In our study, we consider aerosol layers over an even larger altitude range (up
2973 to 7 km). Nevertheless, it is interesting to see how the simulated O_4 (d)AMFs change if the
2974 extinctions at various altitude ranges are changed systematically. Here we chose the aerosol
2975 extinction profile extracted by INTA for the period 7:00 to 11:00 on 8 July, because it
2976 contains substantial amounts of aerosols in elevated layers (see Fig. 9). During that period
2977 three distinct aerosol layers can be identified (see Table A30).

2978
2979 Table A30 Selection of different aerosol layers on 08 July (07:00 – 11:00)

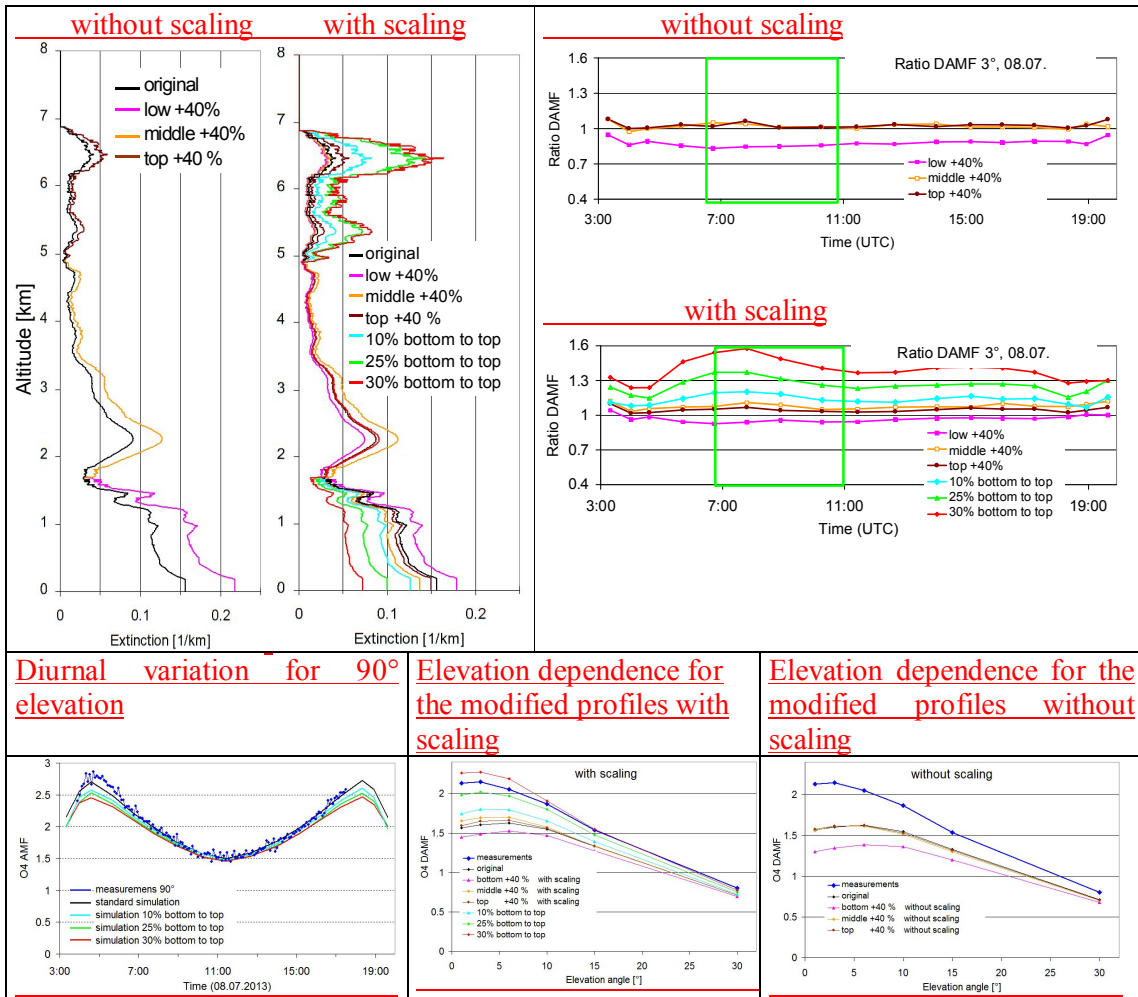
layer	AOD	Relative contribution to total AOD
0 – 1.68 km	0.186	55.4 %
1.68 – 4.9 km	0.116	34.5 %
4.9 – 7 km	0.035	10.4 %

2980
2981 Then, the extinction of the individual aerosol layers were increased by 40 % compared to the
2982 original profile. These profiles (referred to as ‘without scaling’) were used for the simulation
2983 of O_4 (d)AMFs. A second set of O_4 (d)AMFs was simulated for the same profiles, after they
2984 were scaled by a constant factor to match the AOD of the original extinction profile (referred
2985 to as ‘with scaling’). A third set of profiles was created assuming that a certain fraction of the
2986 total AOD was relocated from the bottom layer to the top layer. Here fractions of 10%, 25%
2987 and 30% were assumed.

2988 The modified profiles and the ratios of the corresponding O_4 DAMFs versus the O_4 dAMFs of
2989 the original profile are shown in Fig. A34. For the unscaled profiles the O_4 dAMFs strongly
2990 decrease (by about 30%) if the extinction in the lowest layer is increased. If the extinction in
2991 the middle or upper layer is increased a slight increase (about 3 %) of the O_4 dAMFs is found.
2992 For the scaled profiles different results are found, because the increase of the extinction in one
2993 layer is now balanced by a decrease of the aerosol extinction in the other layers. If the
2994 extinction in the lowest layer is increased by 40%, the O_4 dAMFs still decrease, but only by
2995 about 7%. If the extinction in the middle or upper layer is increased the O_4 dAMFs increase
2996 by about 3 % and 7 %, respectively (see Table A31). For the profiles in which a certain
2997 fraction of the total AOD was relocated from the bottom to the top layer, the O_4 dAMFs

2998 increase strongly compared to those of the standard profiles. If 10% of the total AOD were
2999 relocated the increase is similar to that for the modified profile 'below 0.75km' in appendix
3000 A5. However, if 25% or 30% of the total AOD were relocated, the O₄ dAMFs increase much
3001 stronger. For a relocation of about 27% almost perfect agreement with the measurements is
3002 found (see Fig. A34). That means for such an aerosol profile simulations and measurements
3003 are in agreement wthout the need for a scaling factor. However, it should be noted that such a
3004 large redistribution is not supported by the AERONET inersion products (see appendix A5).
3005 Here it should be noted that for such a profile, about 73% of the total AOD would be located
3006 above about 1.7km. Also, for such aerosol profiles the simulated O₄ AMFs for 90° elevation
3007 systematically underestimate the measured O₄ AMFs at high SZA by about 15% (see Fig.
3008 A34), whereas much better agreement is found for the standard settings. The underestimation
3009 is caused by the high aerosol extinction at high altitudes, which increase the scattering altitude
3010 of the solar photons observed at 90° elevation.

3011
3012
3013



3014 Fig. A34 Top left: Aerosol profiles used for the simulations (see text). Top right: Ratios of the
3015 O₄ (d)AMFs simulated for the modified profiles versus those of the original profile. Bottom:
3016 comparison of the measured diurnal variation (SZA dependence) for 90° elevation, and the
3017 elevation dependence of the O₄ dAMFs for the period 7:00 – 11:00 on 8 July.
3018
3019

3020
3021 Table A31 Ratios of (d)AMFs for 8 July 2013 for the modified profiles with respect to the
3022 original profile

	<u>low</u> <u>+40 %</u>	<u>middle</u> <u>+40 %</u>	<u>top</u> <u>+40 %</u>	<u>10%</u> <u>bottom</u> <u>to top</u>	<u>25%</u> <u>bottom</u> <u>to top</u>	<u>30%</u> <u>bottom</u> <u>to top</u>
<u>ratio AMF without scaling</u>	<u>0.95</u>	<u>1.03</u>	<u>1.03</u>			
<u>ratio dAMF without scaling</u>	<u>0.85</u>	<u>1.02</u>	<u>1.02</u>			
<u>ratio AMF with scaling</u>	<u>1.00</u>	<u>1.06</u>	<u>1.04</u>	<u>1.07</u>	<u>1.12</u>	<u>1.20</u>
<u>ratio dAMF with scaling</u>	<u>0.94</u>	<u>1.08</u>	<u>1.04</u>	<u>1.17</u>	<u>1.31</u>	<u>1.48</u>

3023
3024
3025
3026
3027
3028
3029
3030
3031
3032